Structural Response of Piping Components to Detonation Loading

Z. Liang, T. Curran and J. E. Shepherd

Graduate Aeronautical Laboratories
California Institute of Technology
Pasadena, CA 91125

Explosion Dynamics Laboratory Report FM2006.008

December 20, 2008

Abstract

Experimental studies were carried out on the elastic structural response of simple piping systems to internal explosions in the form of a propagating detonation wave. We examined the propagation of detonation in straight tubes with reflection from a closed end, propagation around a gradual bend, and through a 90-degree tee branch. Hoop and longitudinal strain histories were obtained at a number of locations on each specimen and are analyzed using simple models of structural response. In the case of the tee branch specimens, significant beam bending mode excitation was observed and the peak strains were substantially larger than observed in either the straight sections or bends. The implications are that both beam bending and hoop oscillation modes must be considered analyzing the response of industrial piping systems to internal explosion hazards.

Executive Summary

Experimental studies were carried out on the structural response of simple piping systems to internal explosions in the form of a propagating detonation wave. The specific cases we examined were the propagation of detonation in straight tubes with reflection from a closed end, propagation around a gradual bend, and through a tee branch. The piping systems were modeled by specimens constructed of 1-5/8-in. round, mild-steel, tubing with a wall thickness of .060-in and total lengths between 2 and 3-1/2 ft. Three types of specimens were used: straight sections, sections with a bend of radius 6 in. and sections with a tube intersecting at right angles. The specimens were fastened to a stiff fixture with a combination of slip-on sleeves and rigid collets. Stoichiometric mixtures of ethylene-oxygen (C_2H_4+$3O_2$) were initiated by a spark plug and transition to detonation occurring in an initiator tube about 1.5 m from the specimen. For most cases, we studied nearly-ideal detonations with speeds close to the Chapman-Jouguet velocity and detonation cell sizes much smaller than the tube diameter.

Hoop and longitudinal strain histories were obtained at a number of locations on each specimen. The deformations were all within the elastic range in the present series of tests. Pressure histories were measured in separate specimens using piezoelectric pressure transducers mounted in welded fittings on tubes of the identical construction as the strain specimens. The peak strains are reported for each case and compared with static estimates based on CJ and reflected CJ pressures in order to define bounds on the dynamic load factors. For the straight sections and gradual bends, the peak strains can be bounded by a dynamic load factor of 1.25 using a reference pressure corresponding to that produced by an ideal reflected CJ detonation.

In the case of the tee intersection and bend, the excitation of multiple modes with widely varying frequencies are observed. This is most obvious for the tee specimen, for which we observe a short-period (25 μs) hoop oscillation superposed on a much longer period (4-5 ms) beam bending mode. The peak strains associated with the beam bending modes are up to twice as large as the hoop oscillations for the case of our tee so that superposition of the modes results in peak strains that can be up to two times larger than in a straight tube with reflection. The peak strains can be bounded by a dynamic load factor of 2 using a reference pressure corresponding to that produced by an ideal reflected CJ detonation. For the tee specimen, the beam bending motion can be modeled using a simple single-degree-of-freedom model of structural response.

Although the magnitude of the strains and the modes of oscillation are specific to the specimens we tested, we believe that the results are broadly applicable to piping systems.

The implication for explosion hazard analysis are that in the case of detonations inside pipes, structural modes of oscillation may be as significant as high-frequency breathing modes and in some cases, the superposition of the two modes may lead to much large structural response than estimated on the basis on each mode alone.

Contents

List of Figures

List of Tables

1 Introduction

Industrial plants with extensive piping networks are vulnerable to mechanical damage if internal explosions take place within the pipes or connected components. This is potential hazard with plants that deliberately handle combustible gases (Thibault et al., 2000, Sperber et al., 1999) and may be a consequence of accident situations in complex facilities like nuclear power plants (Naitoh et al., 2003b,a, Kuznetsov et al., 2005), waste or fuel reprocessing facilities. For plants that handle hazardous materials, such accidents present not only an economic setback, but also a danger to those who work in the plant and the surrounding environment.

Previously, tests in the Explosion Dynamics Laboratory at Caltech have been performed to investigate the mechanical effects of shock and detonation waves on straight sections of pipe (Beltman et al., 1999, Beltman and Shepherd, 2002). The fracture of tubes with deliberate flaws and related issues were examined in Chao (2004), Chao and Shepherd (2004, 2005a,b). The mechanical effects due to deflagration-to-detonation transition (DDT) inside of a straight section or near a pipe end were examined by (Pintgen and Shepherd, 2005, 2006) and (Liang et al., 2006b,a, Liang and Shepherd, 2007). The results of this work is summarized in Shepherd (2006)

The purpose of the present investigation is to extend the previous work to cover elements of more complex cases such as the piping system shown in Fig. 1. The elements that are considered in the present study are reflection of a detonation from a closed end, the propagation through 90-degree bends, and tee sections.

1.1 Previous Testing on Piping Systems

There has been one published experimental study by Thomas (2002) on detonation in piping systems. The study examined detonation propagation in an ethylene-air mixture inside GRP (300 mm diameter, 8-9 mm wall thickness) and MDPE (30 mm diameter, 15 mm wall thickness) piping with a closed-end straight section, single and double-bends, and a tees with one end closed. Strain (hoop and axial), displacement, gas pressure, were measured at selected locations. Dominion Engineering (Ahnert, 2006) analyzed the single and double-bend case using a detailed finite-element model of the piping system and supports with an internal traveling load that simulated the detonation propagation inside the pipe. The time-dependence of the pipe displacement at the supports was calculated and compared with the measurements. For three model pressure profiles, reasonable agreement was found between measured and predicted response for the first 100 ms in the single bend case with one exception that can be accounted for by the omission of an axial load in the model.

Attempts to simulate the double-bend case were unsuccessful, apparently due to processes like plastic strain that were note modeled. The conclusion is that while these tests showed that it is feasible to make measurements of the system response, it is not possible to use this particular test data for quantitative benchmarks.

The difficulties with using data from these tests are due to the nature of the piping materials (the properties of the GRP were unknown and the MDPE pipe ruptured during the test), type of supports (thin plates that significantly deformed), and detonation initiation method. The GRP material was not characterized and certainly has a complex constitutive relationship that is at least anisotropic. The support construction is difficult to model, involving a collar with an elastomer sheet, and support plates that undergo large deformation. The deformation measurements and SDOF modeling by Thomas (2002) clearly demonstrate that significant hysteresis and plastic deformation was taking place in both pipe and supports in some tests. The initiation section was not completely isolated from the test section but it was difficult to quantify (see the discussion in Ahnert, 2006) how much axial force was transmitted by the inflatable collar between the two sections. The differences between the Thomas piping system and typical metallic piping systems used in the power industry (ASME, 2001) are quite substantial. Tests with much stiffer supports similar to U-bolt restraints (see Chap. 6 Antaki, 2003) and metallic pipes that respond elastically are needed to validate modeling for typical piping systems used in the power or nuclear industry.

1.2 Piping System Response to Internal Detonations

A detonation is a dynamic load that excites a wide spectrum of mechanical vibrations in a piping system and creates an internal pressure load. If a piping system is to withstand a detonation, both aspects of the loading must be considered. The highest vibrational frequencies are associated with the shell oscillations, particularly the radial or hoop mode, and the lowest are associated with beam bending modes. The amplitude of the vibrations and summation of the various modes together with the internal pressurization determines the peak stress and strain. From this point of view, the response of piping systems to internal detonations has common elements with the evaluation of seismic (Antaki, 2003, see Chapter 11) and fluid-transient (Antaki, 2003, see Chapter 9) excitation of piping systems. The static internal pressurization is a key aspect of the design of piping systems Antaki (2003) and pressure vessels Harvey (1991), Annaratone (2007) and static design can be augmented with considerations of dynamic load factors to formulate elementary design rules for dynamic situations. Some design considerations for dynamic pressurization by explosions within piping are discussed by (Antaki, 2003, see Chapter 12) and the specific problem of

high explosive detonation inside vessels is discussed by (Rodriguez and Duffey, 2004, Duffey et al., 2002). In general, the stresses due to both internal pressure and vibration have to be considered simultaneously in order to fully evaluate the response of a piping system to an internal explosion. This means that the collective motions of all the components of the piping system must be considered through testing Harris and Piersol (2002), McConnell (1995) and detailed structural response computations Paz (1985) similar to what is done to evaluate water hammer and seismic response (Chaps. 34, 36, 37 Rao, 2002). For vessels, this evaluation has been formulated as a Code Case 2564 which extends the ASME B&PV code to cover impulsively loaded vessels. Although elements of this Code Case apply to detonations inside piping, there are some essential differences which will have to be addressed. At present there is no accepted Code Case or design guide for piping systems with internal detonations. The present study is part of a larger effort to identify the issues and develop data that can be used for a design guide.

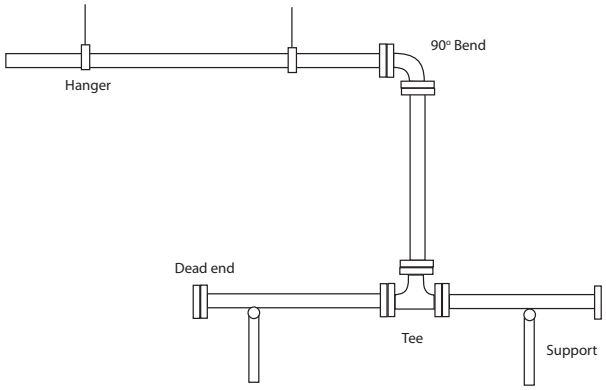

Figure 1: Generic piping system with features of interest: bends, tees, and dead ends.

A detonation or shock wave propagating within a tube represents a traveling load in the form of a step or jump in pressure. For ideal detonations, the wave speed is constant and approximately equal to the Chapman-Jouguet (CJ) value and the pressure loading is axi-symmetric. A sudden load traveling at a constant speed excites periodic flexural[1] waves Beltman and Shepherd (2002) behind the wave front. The flexural waves have a characteristic frequency associated with the breathing mode of radial oscillation of the tube wall and the largest deformations are produced in the circumferential direction (hoop strain). The magnitude of the hoop strains has been extensively characterized in previous studies with straight tubes Beltman and Shepherd (2002). The peak value of the strain depends on the

[1]Here flexural refers to localized bending induced by the radial hoop oscillations. These are high-frequency, short-wave length vibration modes that are distinct from the low-frequency, long-wavelength bending modes associated the flexural of the piping system considered as a space-frame type structure.

tube material parameters such as Young's modulus, Poisson ratio, and tube dimensions, and also the detonation peak pressure, wave speed, and time dependence of the following flow. In some situations, strains can be significantly higher, as much as 3 or 4 times greater, than the strains that would be observed under simple static loading with the same internal pressure. These situations include resonant excitation, interaction of direct and reflected flexural waves, and detonation pressure oscillations coupling with flexural waves (Beltman and Shepherd, 2002) and also deflagration-to-detonation transition (Liang et al., 2006b,a, Liang and Shepherd, 2007).

When a detonation wave propagates in the pipe with a closed end, a reflected shock wave is created when the flow following the detonation wave comes to rest. Previous investigations Shepherd et al. (1991), Boyack et al. (1993) have shown that the peak pressure of this reflected shock wave can be as high as 2.5 times the CJ pressure. The shock pressure rapidly decays as the wave moves away from the closed end. One consequence of this is a sudden jump in force in the direction perpendicular to the closure, which creates longitudinal (axial) stresses and may create a bending moment in a piping system. As the shock propagates away from the closed end, flexural waves are also created in the tube just as in the case of the incident detonation wave. These two sets of flexural waves interfere, leading to the maximum strain values being observed at times corresponding to the passing of the reflected wave (Shepherd, 2006). The highest strains are found close to but not exactly at the closed end due to the restraining effect of the end closure. As a consequence, the onset of plastic deformation and the greatest risk of material failure is found in testing to occur adjacent to closed ends.

When a detonation wave propagates in a bend, the change in direction of the flow results in the generation of a reaction force in the plane of the bend and opposing the resultant of the momentum flux of the flows into and out of the bend. In addition, the detonation wave diffracts, resulting in lower pressures on the inside (intrados) of the bend and higher pressures on the outside (extrados) of the bend. The detonation takes some time to recover from this disturbance and this results in an asymmetric loading downstream of the bend. The net consequence of the propagation through a bend is a time-dependent force on the elbow that has an impulsive and a static component. These forces and impulses generate structural motion in a piping system, primarily bending motions that are usually treated by considering the piping as beam-like structural elements. One of the key issues is the possibility that the hoop and bending deformations occur simultaneously, which will complicate the evaluation of the structural loading. When a detonation wave propagates into a tee junction, the effect is similar to that with an elbow but the direction and magnitude of the force is different. The detonation is disturbed downstream of the tee and takes some distance to recover to the CJ state.

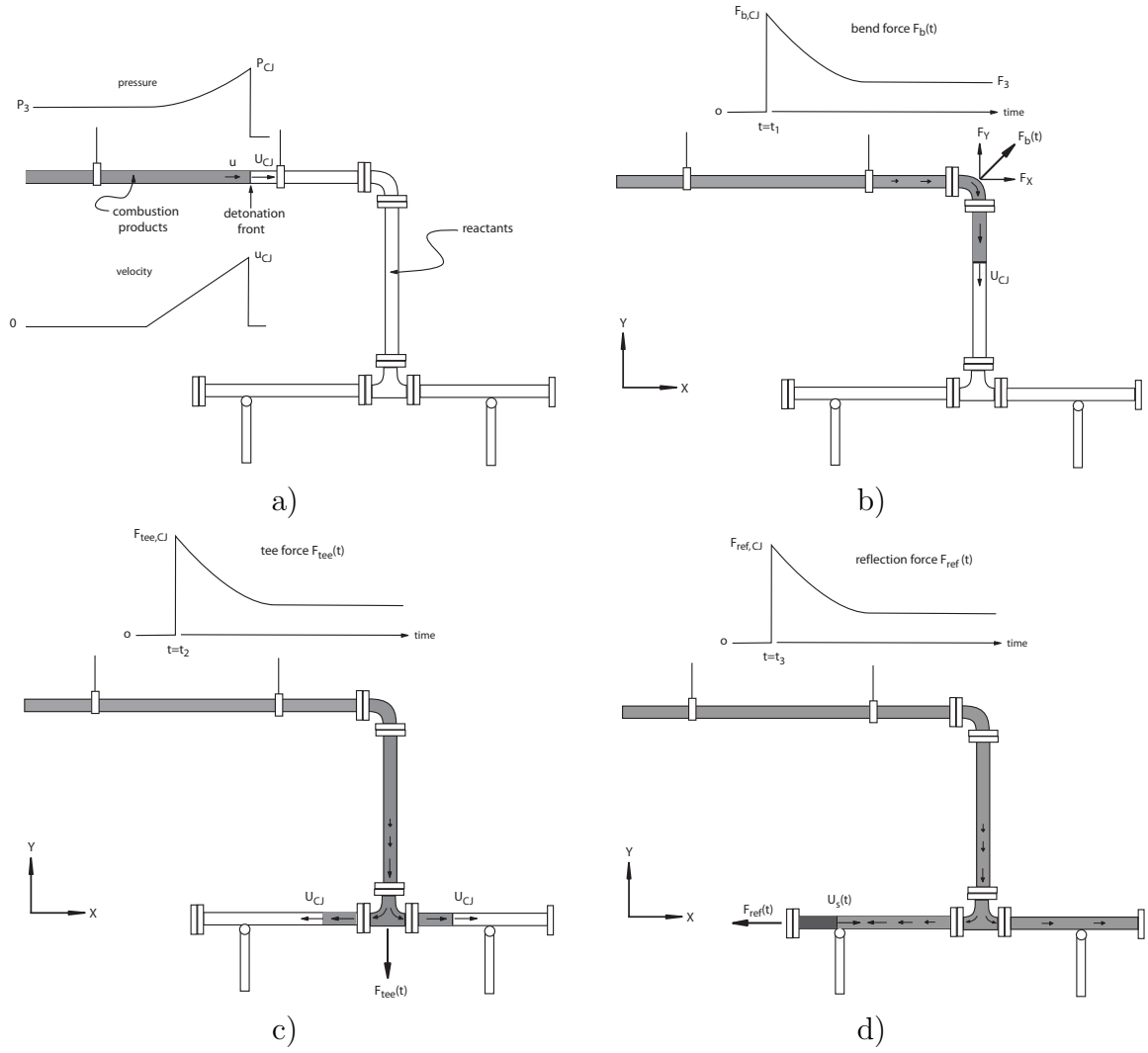

Figure 2: Generation of structural loads due to a) detonation propagation, and interactions with b) bends, c) tees, and d) dead ends.

The net result is that as the detonation propagates through the piping system, a series of forces are applied at the bends, tees, and closed end as shown in Fig. 2. As shown in the figure, the detonation arrives at each location after some propagation delay and then the time-dependent loading is suddenly applied. For an ideal detonation, the nominal propagation delay can simply be computed as the transit time for a constant speed wave. As an example, referring to Fig. 3, the propagation time between the bend and tee will be t_2 - $t_1 = L_2/U_{CJ}$. The forces will excite bending, torsional and ovalization modes in the piping. Superposed on these will be the hoop oscillations that are generated by detonation exciting radial motion. The forces will be applied sequentially as the detonation propagates and in order to compute the structural response using standard piping system mechanical response

approaches, a set of force-time histories (Fig. 3) must be specified by the analyst.

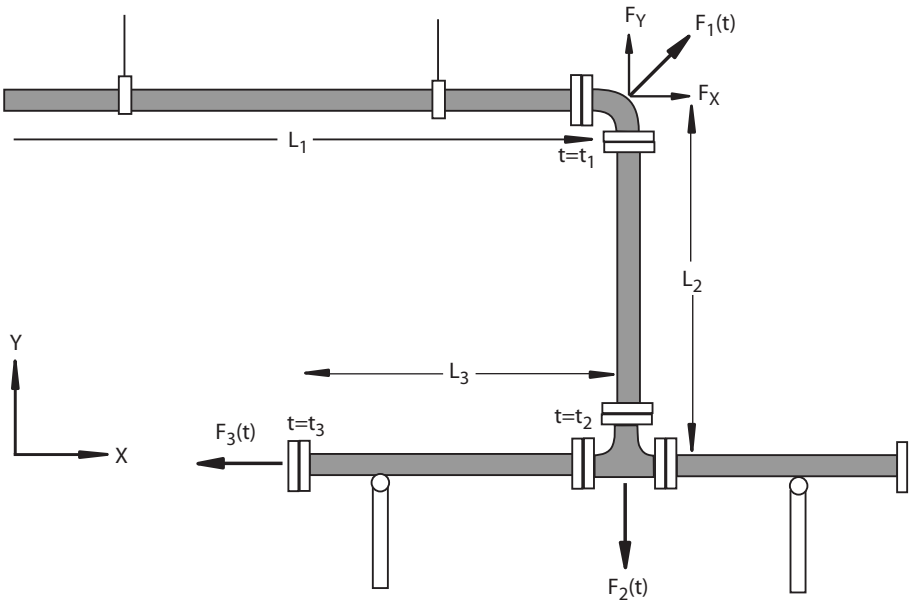

Figure 3: Sequence of structural loads used to compute mechanical response of piping system to detonation propagation.

1.3 Plan of report

In the present study, we measured the pressure waves and structural response of short piping segments with bend, tee and dead end elements. We have compared these measurements with simple models of detonation wave propagation and structural response. We have provided data that can be used to develop and validate models for the forces shown in Fig. 3.

The plan of the report is as follows. Section 2 of this report describes the experimental facility, test fixture, and instrumentation. Sections 3 and 4 describe the results of experiment using straight sections of aluminum and steel specimen tubes. Tests on straight sections were carried out in order to have comparisons with previous work and as standard for comparisons with bend and tee specimens. Section 5 gives the results of detonation propagation in bend specimens. Section 6 gives the results for the tee specimens. Section 7 uses single degree of freedom models to interpret the strain signals. Section 8 summarizes our findings. Data plots from all gages and each test are given in the Appendices.

2 Experimental Set-up

The apparatus consist of four main parts: the test fixture, gas fill system, the control panel and the data acquisition system (DAQ). The test fixture holds the spark initiator, detonation tube and test specimen. The gas fill system is used to evacuate and fill the detonation tube and test specimen to the desired initial pressure and mixture composition. The control panel allows the operator to control all valves and the firing system remotely. The DAQ consists of signal conditioning, digitizing, and data storage for strain gage and pressure transducer signals.

2.1 Test Fixture

The test fixture uses components that were originally designed by Chao (2004) for the detonation-driven fracture studies (Chao and Shepherd, 2002, 2005b) at Caltech from 2002-2007 and summarized in Shepherd (2006). Development of the laboratory facility and experimental studies were originally sponsored by the Office of Naval Research and the US Department of Energy.

The detonation is initiated and stabilized in a 1.607 m long, 6.35 mm wall aluminum tube. At one end of the detonation tube, a spark plug and Shchelkin spiral are used to start the detonation through rapid flame acceleration (see Fig. 4). At the other end of the detonation tube, the test specimen is connected using a O-ring seal in a slip-on flange. The detonation tube and specimen are fastened to W12-60 I-beam with stiff clamps. The end of the specimen was closed with plug containing an O-ring gland seal and pressure transducer. The plug is held by a commercial collet mounted into a steel block bolted to the I-beam or a vertical channel. A vertical beam was used to support the ends of the bend and tee specimens. The vertical beam was constructed out of steel "C" channel (10 x 2-3/4 x .526, 25 lb/ft A36 Steel) and held a block that affixed an end cap into the end of the sample pipe. This entire structure rests atop 2 m long section of I-beam milled flat and lined with slots to accommodate mounting the rest of the described pieces.

2.2 Specimens

There were two types of tubes used in these tests. Tests 1- 5 were carried out with seamless 6061-T6 aluminum tubing similar to that used in Chao (2004). The remaining tests were carried out with steel tubes of cold-rolled electric welded (CREW) ASTM 1008/1010 material with a nominal 1-5/8-in. (41.3 mm) outer diameter and a nominal wall thickness of 0.060-in. (1.524 mm). An ultrasonic thickness gage (Checkline Model TI-007) was used to make

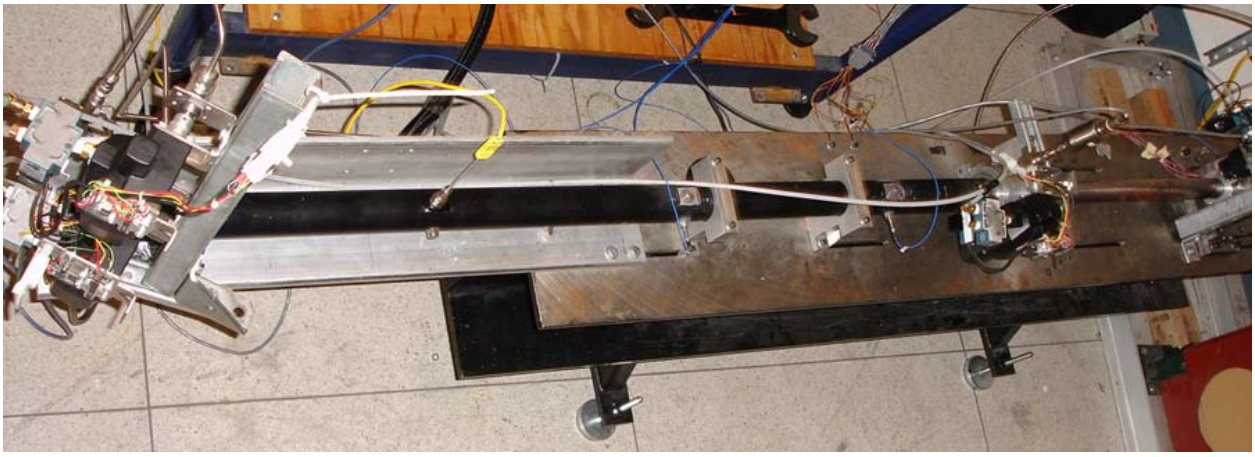

Figure 4: Experimental setup showing the detonation initiation tube connected to the straight specimen.

measurements of the wall thickness in locations around each gage and the values are reported for each specimen. Nominal dimensions and assumed properties of the specimens are given in Table 1.

Table 1: Nominal dimensions and assumed properties for the aluminum and steel tubes. E = modulus of elasticity, ν = Poisson's ratio, ρ = mass density of tube material, D_o = outer diameter of tube, h= tube wall thickness, f_{hoop} = frequency of hoop oscillations, T_{hoop} = period of hoop oscillations, V_{c0} = critical speed for excitation of flexural waves.

Material	E (GPa)	ν	ρ (kg/m^3)	D_o (mm)	h (mm)	f_{hoop} (kHz)	T_{hoop} (μs)	V_{c0} (m/s)
Al 6061	70	0.35	$2.643 \cdot 10^3$	41.3	0.866	40.5	24.7	836.5
ASTM 1010	210	0.29	$7.84 \cdot 10^3$	41.3	1.524	41.4	24.2	1098.4

2.3 Ignition System

The ignition system is short-duration (< 10 μs) spark discharge across a modified aircraft spark plug (Champion Model REJ38). The "J" electrode was removed so that the discharge was over a distance of about 5 mm. The spark initiated a flame, which rapidly accelerated and transitioned to detonation before the first pressure transducer in the initiation tube. A Shchelkin spiral (Fig. 5) was used just downstream of the spark plug to generate turbulence and promote transition to detonation. The spiral consisted of a 10-in length of spring welded to a tubular insert with additional perpendicular rods with a 1-in spacing and alternating orientation welded to the insert.

Figure 5: Looking along the axis of the Shchelkin spiral.

The spark discharge is generated by a using a custom circuit (Fig. 6) to charge a capacitor which is then discharged through a Perkin-Elmer (formerly EG&G) TR-2012 step-up transformer (163:1 secondary:primary ratio) to create the high voltage pulse. The energy stored in the capacitor is on the order of 350 mJ so that the spark discharge energy is much higher than ignition limits for all but the most insensitive mixtures. This ensures prompt ignition even at low pressure and minimizes the chances of misfires.

A number of safety features are incorporated into the discharge circuit to prevent accidental ignition. High voltage cannot be discharged from the capacitor until a sequence of three events has occurred. First, AC power must be applied from the control system by the operator. Second, the capacitor must be charged by applying an arming signal. Third, the capacitor must be discharged by applying a firing signal. The AC power, arming, and firing functions are interlocked to the valve control system, gas leak detectors, room ventilation, and door to the experimental area. In addition to these engineering safety features, a checklist is used to carry out and document the steps in the test procedure (see Appendix A). Arming and firing signals are transmitted through opto-isolators to prevent ground loops.

2.4 Gas Fill System

A gas-fill system previously installed in the room was used to precisely control the mixtures that were put into the apparatus. It consisted of a combination of hand and electropneumatic valves to control the flow of pressurized gases from storage bottles to the appa-

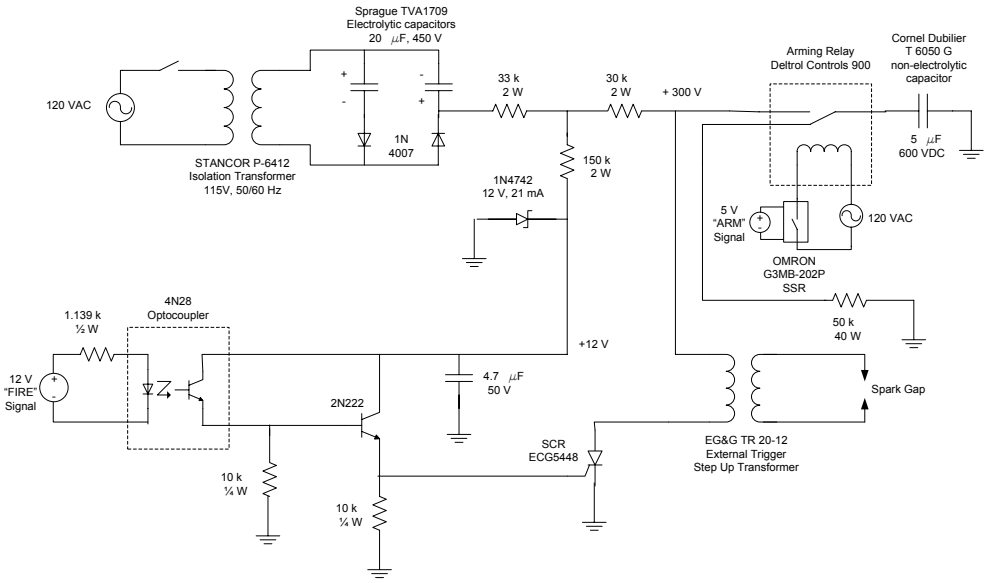

Figure 6: Circuit of custom spark generation unit used to ignite the mixtures.

ratus. The electro-pneumatic valves were operated by a set of switches and relays on the control panel. The valves inside the test area have position sensors that can be read on the control panel.

The control panel pressure gages and valve controls are used to manually fill the test channel to the desired pressure with an accuracy of 0.1 kPa. A Sargent-Welch model 1397 vacuum pump was used to evacuate the apparatus prior to filling and also the fill lines were evacuated when switching gases. After evacuation, the pressure was less than 50 mTorr.

2.5 Data Acquisition System

The data acquisition (DAQ) system consisted of signal conditioning amplifiers and PC-based digitizers. The acquisition of data was triggered by the same signal that was used to discharge the spark to initiate the detonation. The DAQ used National Instruments hardware (BNC 2110 input connectors and PCI 6110 digitizer cards) and LabView software. Strain gage measurements were amplified and filtered by Vishay 2310 signal conditioners prior to digitizing. The pressure signals were directly recorded by the digitizers at the same sampling rate. Data were written into an ASCII file that was used as input to application programs (GUNPLOT, MATLAB) for analyzing and graphing the data.

2.6 Pressure Measurements

To measure the pressure, Piezotronics PCB piezoelectric pressure transducers were employed. The transducers were mounted on the detonation tube (Fig. 7) using SAE J1926 straight thread, o-ring seal fittings machined to accept the transducer. The fittings tended to loosen and leak after repeated shots so the SAE fitting was sealed to the tube using DEVCON 60020 "TITANIUM 5" Epoxy. The models used were of type 113A24 and 113A23, which

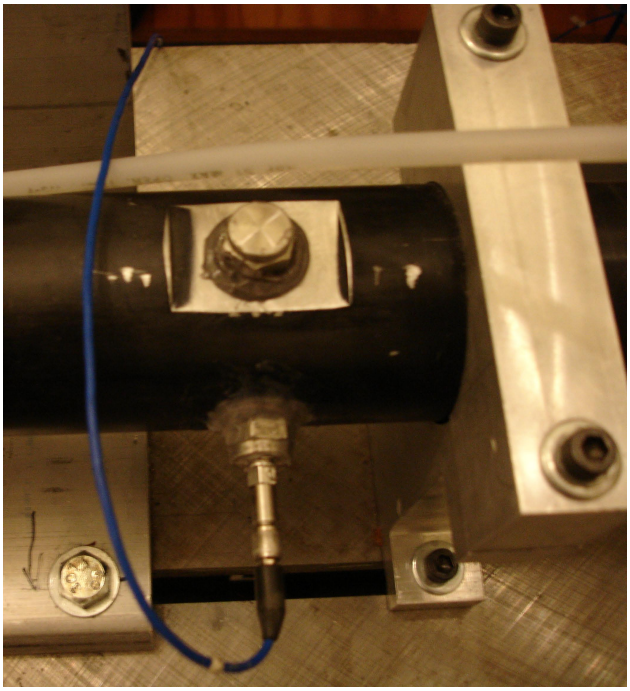

Figure 7: Pressure gage mounting on detonation tube and adjacent tube attachment to I-beam.

have dynamic ranges of 69 bar and 1034 bar, respectively. The pressure transducer signals were passed through 12-channel PCB Model 483A signal conditioner and power supply. A number of issues related to the accuracy and fidelity of pressure measurements of this type are discussed by Liang et al. (2008).

2.7 Strain Gage Measurements

To measure the strain, strain gages of type CEA-06-125UN-350 were used in a 1/4-bridge configuration. They are manufactured by the Micro-Measurements Division of Vishay Measurements Group. The grid resistance of these gages is 350.0 ohm and the gage factors were either 2.100 or 2.125 (this value is included in the conversion factor used in the DAQ). Each

gage feeds its signal into a separate Type 2310A strain gage amplifier, which has an excitation voltage of 10V. A three-wire configuration with separate excitation and sense lines was used to minimize line length effects. A number of issues related to the accuracy and fidelity of strain measurements of this type are discussed by Shepherd et al. (2008).

2.8 Experimental Check List

To ensure that each experiment was done in a repeatable and safe fashion, a separate checklist (see Appendix A) was generated and filled out for each test. The target initial conditions were pre-computed and the CJ detonation conditions were calculated ahead of the shot.

2.9 Test Mixtures and Strain Estimates

In all the tests, a stoichiometric (C_2H_4+$3O_2$) mixture at room temperature and initial pressures from 0.05 to 1.0 bar (5 to 100 kPa) were used. The pressure and strain signals were analyzed using computed values of the peak pressure for idealized combustion processes. The values for CJ pressure (P_{CJ}), reflected CJ pressure (P_{CJref}) and constant volume explosion pressure (P_{CV}) are calculated using a chemical equilibrium program (Reynolds, 1986). The computed values are listed in Table 2.

The peak strain values are analyzed using the concept of dynamic load factor Φ that is based on ideas from single-degree of freedom analysis of structures (Paz, 1985) and widely used in explosion analysis (Smith and Hetherington, 1994, Baker et al., 1983). The dynamic load factor can be calculated or estimated for simple structures and known loading profiles (Biggs, 1964). For the simplest case of a step function load followed by an exponential decay, Φ can be computed exactly as a function of the ratio of structural response time to loading decay time. In the case of uniaxial strain due to a load with a peak pressure P_{max}, the maximum strain can be estimated as

$$\epsilon_{max} = \Phi \frac{(P_{max} - P_a)}{E} \frac{R}{h} \,, \tag{1}$$

where ϵ, E, R, h and P_a are respectively the hoop strain, Young's modulus, average midpoint radius and thickness of the tube, and ambient pressure in the atmosphere surrounding the tube. For the aluminum 6061T6 test specimens, E = 70 GPa, R = 20.2 mm (0.795-in.) and h = 0.866 mm (0.0341-in.). For the steel C1010 test specimens, E = 210 GPa, R = 19.89 mm (0.783-in.) and h = 1.486 mm (0.0585-in.).

For simple waveforms, $0 < \Phi < 2$, with a value of 2 for step-function loading and $\Phi < 2$ for suddenly applied but decaying loads. As the decay time decreases, the value of Φ

decreases with the limit of small values for short duration, low-amplitude pulses (impulsive waveform). For propagating detonations, the dynamic load factor can be computed (Beltman and Shepherd, 2002) and the magnitude depends on the speed of the detonation wave relative to the critical wave speed for flexural wave propagation in the tube wall (Beltman and Shepherd, 2002). For the aluminum tubes used in this study, the critical wave speed is 1100 m/s, for the steel tubes, 850 m/s. The detonation speeds are approximately twice this value. From the analysis and experiments in Beltman and Shepherd (2002), the maximum hoop strain can be estimated for propagating detonations by using $1 \leq \Phi \leq 2$ and the computed CJ pressure as the maximum applied pressure. The precise value of the amplification factor will depend on other factors such as detonation propagation distance, tube construction - particularly flanges, effect of tube wall thickness, and the detonation cell size, see Beltman and Shepherd (2002), Chao (2004) for discussions of particular situations.

The maximum pressure can either be determined experimentally or taken to be a reference value associated with a well-defined physical property. In the case of detonations, either the CJ pressure or else the peak pressure produced by normal reflection of a CJ detonation are possible choices. The CJ pressure is appropriate for propagating waves, the reflected pressure is appropriate for dead ends and DDT. For deflagrations, the appropriate reference pressure is the CV explosion pressure and $\Phi = 1$, i.e., the loading is quasi-static. From an experimental point of view, the dynamic load factor represents the ratio of the measured peak strain to the static value of strain corresponding to the peak pressure that is applied.

$$\Phi = \frac{\epsilon_{peak}}{\epsilon_{static}} \, . \tag{2}$$

In the present experiments, the reference pressure depends on the initial pressure since the composition is fixed. The equivalent static strains ($\Phi = 1$) corresponding to the CJ detonation pressure (ϵ_{CJ}) and reflected CJ detonation pressure (ϵ_{CJref}) have been computed for the range of initial pressures used in these experiments and are given in Table 2.

In addition to the thermodynamic properties and strain estimates, we have used the idealized ZND detonation model (Shepherd, 1986) to compute the reaction zone length Δ based one the GRI-Mech 3.0 reaction mechanism and thermochemistry (Smith et al., 2004). The reaction length can be used directly as a measure of thickness of the detonation wave although the detonation cell width is a more conventional scaling distance. Based on the data given in Detonation Database, the ratio of cell width to reaction zone is approximately 30. Using this fixed constant of proportionality, we have estimated the cell widths and these are shown together with data in Fig. 8

The data and estimates shown in Fig. 8 indicate that at atmospheric pressure, the cell

Table 2: Computed parameters for C_2H_4+3O_2 (stoichiometric) mixtures at various initial pressures. The strain values are computed for the steel tubes using (1) with $\Phi = 1$.

P_0 (bar)	P_{CV} (MPa)	P_{CJ} (MPa)	P_{CJref} (MPa)	ϵ_{CJ} (μstrain)	ϵ_{CJref} μstrain)	U_{CJ} (m/s)	Δ (mm)
1	1.679	3.326	8.342	206	525	2375.6	0.022
0.8	1.332	2.639	6.619	162	416	2364.7	0.027
0.7	1.160	2.298	5.763	140	361	2358.2	0.030
0.6	0.989	1.958	4.911	118	306	2350.7	0.035
0.5	0.818	1.621	4.064	97	253	2341.9	0.042
0.4	0.649	1.286	3.224	76	199	2331.2	0.052
0.3	0.482	0.954	2.391	54	146	2317.4	0.069
0.2	0.316	0.626	1.569	34	94	2298.0	0.104
0.15	0.235	0.465	1.164	23	68	2298.0	0.104
0.1	0.154	0.305	0.764	13	42	2265.4	0.216
0.05	0.075	0.149	0.372	3.1	17	2233.4	0.458

size is 0.7 mm and the detonation should behave in an almost ideal fashion, propagating close the CJ speed in almost all situations. With decreasing initial pressure, the cell width will increase and any effects of cellular structure on the structural response should become more pronounced. At an initial pressure of 1-2 kPa (0.01-0.02 bar), the cell width becomes comparable to the tube diameter and very strong oscillations on the detonation front will be present as the detonation reaches the "spinning"regime. One of the purposes of the present study was to use this variation of cell size with initial pressure to examine how the presence of strong pressure fluctuations on the front affects the strain histories.

2.10 Hoop Oscillation

An ideal detonation wave propagating along the axis of a straight tube creates a traveling flexural wave (Beltman and Shepherd, 2002) with a primarily radial deflection. The main frequency of the radial mode excited by the detonation wave passage is measured (Shepherd et al., 2008) to be close to the frequency of hoop or axi-symmetric radial vibrations of long cylindrical tubes. For the axially unconfined case, the fundamental frequency is

$$f = \frac{1}{2\pi R}\sqrt{\frac{E}{\rho(1-\nu^2)}}, \tag{3}$$

where R is the mean radius of the pipe, $R = (D_o - h)/2$, E is the modulus of elasticity, ρ is the density and ν is Poisson's Ratio. Table 1 lists the parameters and fundamental frequency

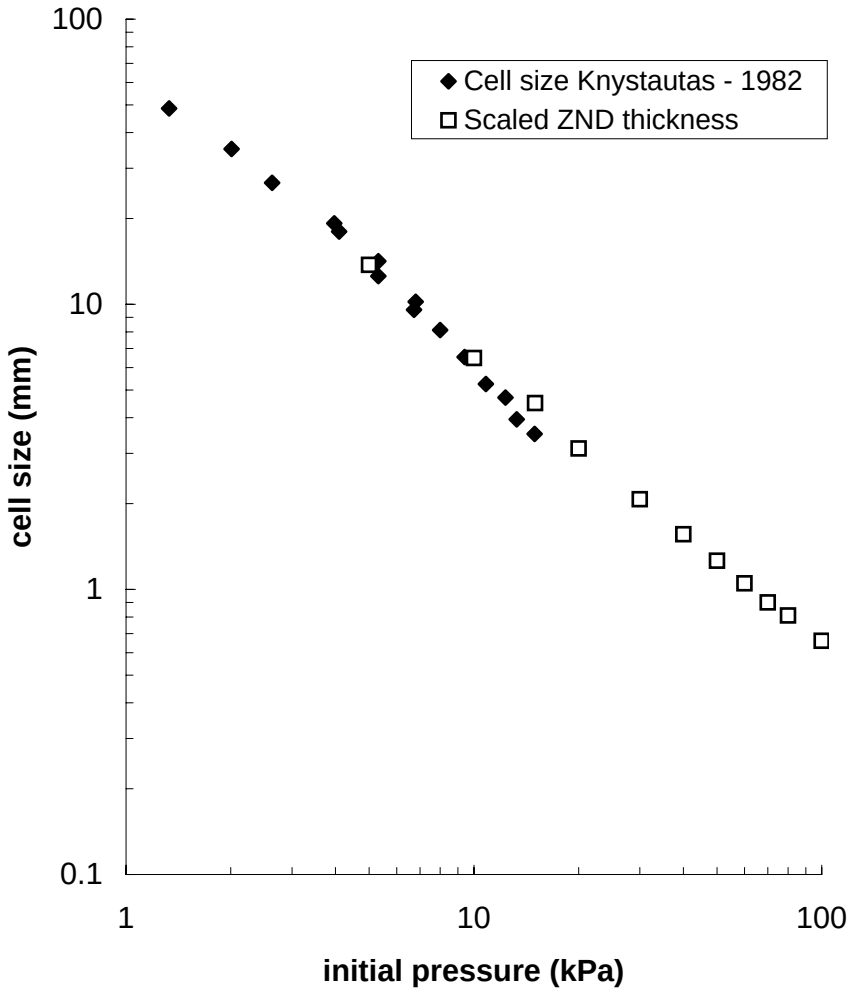

Figure 8: Measured detonation cell width (Knystautas et al., 1982) and scaled ZND reaction zone lengths (30Δ) for stoichiometric ethylene-oxygen mixtures.

for the two tubes used in the present study. The period of the hoop oscillation $T = 1/f$ is much less than the elastic wave transit time τ_l through the tube wall.

$$\tau_l = h/c_l \tag{4}$$

where the longitudinal sound speed c_l, about 6000 m/s for both aluminum and steel. The transit time is about 0.25 μs, 100 times smaller than the structural period, $T \approx 25$ μs. For this reason, we only consider the structural modes of oscillation. There is a longitudinal strain wave precursor that propagates at the bar speed (about 5000 m/s) but these waves were not measured in the present study.

2.11 Dynamic load factor and critical wave speed

The peak structural deflection due to the hoop oscillation is a function of the peak pressure, detonation wave speed, boundary conditions on the tube motion, and the distance that the wave is traveled. A detailed discussion is given in Beltman and Shepherd (2002). One of the key parameters is the first critical speed V_{c0}, which corresponds to the group velocity of flexural waves that consist of coupled radial-bending oscillations. If rotatory inertia and shear deformation is neglected, the closed form solution for V_{c0} is

$$V_{c0} = \sqrt{\frac{Eh}{\rho R}} \left(\frac{1}{3(1-\nu^2)} \right)^{1/4} \tag{5}$$

This was first derived by Simpkins and the relevance to detonations is discussed in Beltman and Shepherd (2002). The dynamic load factor Φ approaches one, when the internal loading travels slower than V_{c0}, and Φ approaches two when the load travels much faster than V_{c0}. There is a resonance effect when the load speed is close to V_{c0}, where Φ has been observed to reach peak values on the order of 3 to 4. For the steel specimen, V_{c0} is 1098 m/s and since the wave speed in the present tests, $U_{CJ} > 2000$ m/s, the dynamic load factor is between one and two.

3 Straight aluminium tube specimen

In order to verify the setup, we started the tests with the same type of aluminum specimen as used in previous studies (Liang et al., 2008, Shepherd et al., 2008) in our laboratory. This specimen is a seamless 6061-T6 tube with an outer diameter of 1-5/8-in. (41.3 mm) and a nominal wall thickness of 0.034-in. (0.866 mm). We did not make a survey of the wall thickness as we did for the steel tubes since the strain measurements were not being used for validation. From our previous study (Shepherd et al., 2008) we know a periodic variation of up to 10% in thickness is typical for these specimens.

Three pressure transducers (P1, P2, and P3) were mounted along the tube, two of which were located on the main detonation tube and one was on the reflecting end plug that formed the tube closure (Fig. 9). The strain gages on the straight tube specimens were all located near the termination end of the specimen as shown in Fig 9. Five strain gages (S1-S5) were

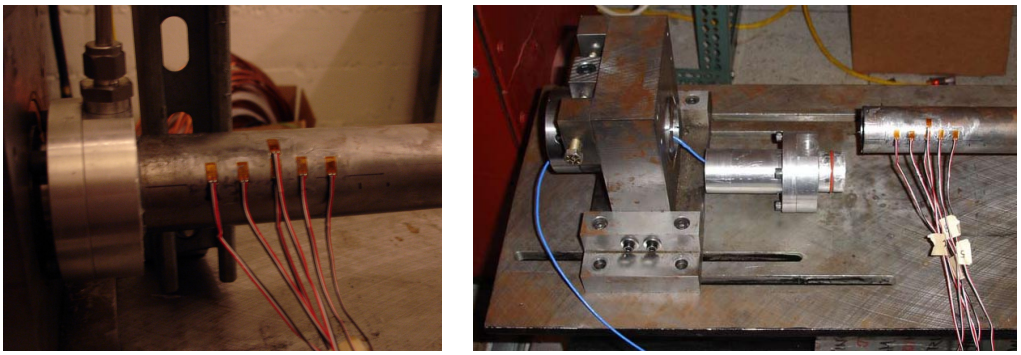

a) b)

Figure 9: Closed end of tube with strain gages and pressure gage. a) tube assembled with closure. b) tube and components of closure in disassembled state; the end plug (middle) is held by the collet clamp on the left and fits inside the tube on the right.

placed at 0.5-in. increments, starting 1-in. from the termination end of the specimen and moving back toward the beginning of the tube. This 1-in. distance was included because the end cap extended 1-in. into the end of the specimen tube. All of these gages were oriented in the hoop direction and placed along the longitudinal axis of the specimen. There will be some variation in the strain with circumferential location due to wall thickness non-uniformity, see Shepherd et al. (2008). We did not attempt to evaluate this effect in the present tests since the strains were in the plastic regime and substantial numerical efforts would be required to model the deformation history. The same tube was used for all five shots and strain-hardening will obviously occur and is apparent in the peak strains observed on S5 (see App. B).

The dimensions of the setup are shown in Fig. 10. The locations of the pressure transducers to the ignition plane and the locations of the strain gages to the reflecting end are listed in Table 3. The locations of the strain gages are given to the center of the gage element. The gages (CEA-06-250UN-350) have an active gage element that is 0.12 in (3.05 mm) wide and 0.25 in (6.35 mm) long.

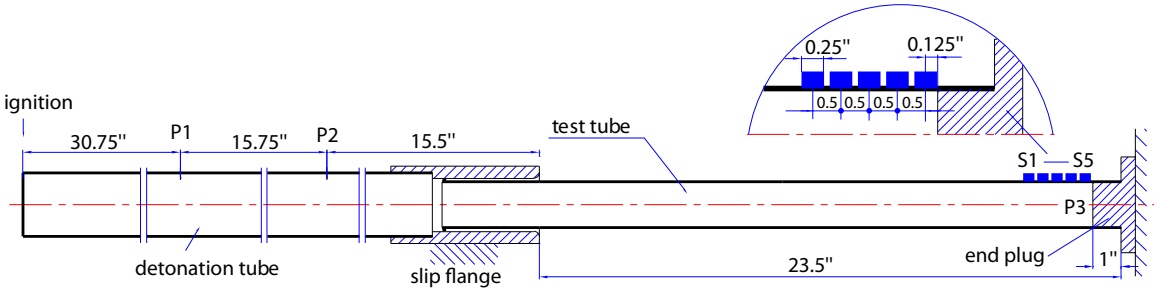

Figure 10: Tube setup and dimensions for the straight aluminum tube.

Table 3: Distance X of the pressure transducers to the ignition plane and the strain gages to the reflecting end.

	X (m)	X (in)		X (mm)	X (in)
P1	0.780	30.75	S5	3.17	0.125
P2	1.180	46.50	S4	15.87	0.625
P3	2.146	84.50	S3	28.57	1.125
			S2	41.27	1.625
			S1	53.97	2.125

A total of 5 tests were performed with an initial pressure of 1 bar. A summary table of peak values is given in App. B and the pressure and strain histories are given in App. F. The data are very similar for all 5 tests and a typical set of results are shown in Figure 11 for shot 2. The pressure traces (see Fig. 11a) show the progression of the detonation wave through the detonation tube (P1 and P2) and reflecting from the plug at the end of the specimen tube (P3). The peak pressures are subject to substantial shot to shot uncertainty due the presence of strong pressure oscillations on the signals. The measured peak pressures of the incident waves are 1.5–1.9 times P_{CJ} and the reflected peak pressure is on the average 1.1 times higher than P_{CJref}, see Table 2. The high peak values on the incident waves are due to very short transients (shock waves followed by expansions) and as discussed in Liang et al. (2008), are probably transverse shock waves from either the initiation process, discontinuities in the detonation tube bore area, or at low pressure, detonation instability.

The strain gages (see Fig. 11b) register deformation as soon as the detonation wave reaches that location. The general features of these signals and the mechanism of flexural

wave generation are discussed in detail by Beltman and Shepherd (2002). The detonation is a traveling structural load and excites a propagating oscillation at close to the hoop frequency of 40 kHz for the aluminum specimens. This corresponds to a period of 25 μs, close to what is observed for the highest frequency oscillations in Fig. 11b. The lower frequency (1 kHz or a period of 1 ms) modulation is due to interference between flexural waves excited by both the incident detonation and reflected shock wave. The effect of the incident wave can be seen in the first three cycles of S1. In these three cycles, the average maximum strain value for S1 through S4 is 1835 μstrain. This compares favorably with the peak values between 1700-2050 μstrain (depending on the wall thickness) that was reported for these same types of specimens by Shepherd et al. (2008).

When the wave reaches the end cap it reflects. This can be seen in the increase of magnitude of the pressure signal P3 in comparison to P1 and P2. The reflected shock wave then travels back toward the initiation end of the tube. An increase in the strain signals S1 through S4 can be seen as the wave passes the gage locations for the second time. Strain signal S5 is directly at the end of the specimen next to the end cap, so it only registers the reflected pressure. In the other strain gages, the interference in the flexural waves excited by the incident detonation and reflected shock wave is clearly visible. The interference of the flexural waves signals close to the end wall was also observed by Liang et al. (2006b).

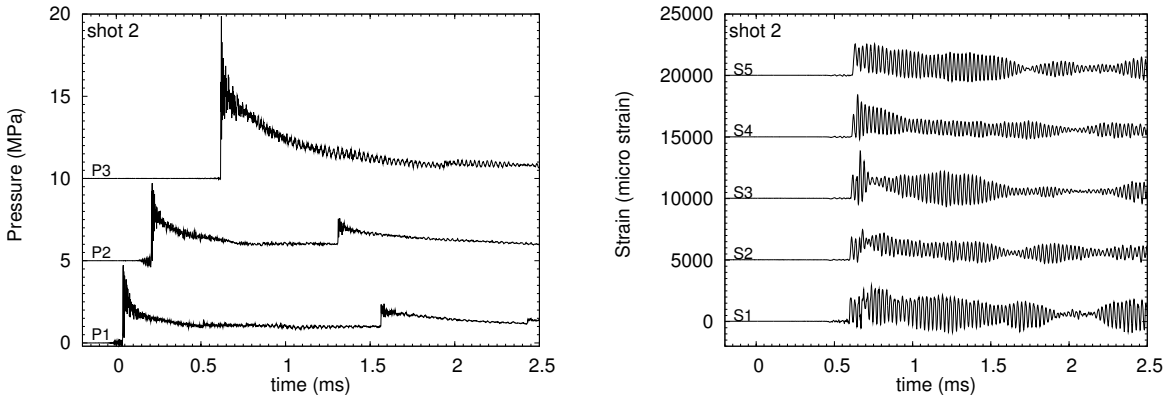

Figure 11: a) Pressure traces and b) strain traces for the aluminium straight tube specimen. Shot 2. $P_0 = 1$ bar.

The peak pressure and the arrival time (see Appendix B for the three pressure transducers were analyzed to determine the average wave speed. Fig. 12 shows that all five shots had very minimal variability in wave speed. Linear regression analysis of the data gives an average wave speed for all 5 tests of 2359 m/s $\pm$ 5 m/s. This is 0.7% less than the CJ speed of 2375.6 m/s computed by STANJAN and 0.6% than the Shock and Detonation Toolbox

value of 2373.6 m/s as discussed in Liang et al. (2008). We conclude that the detonations are traveling very close to the ideal speed. Very similar results were obtained for tests discussed in Liang et al. (2008), Shepherd et al. (2008).

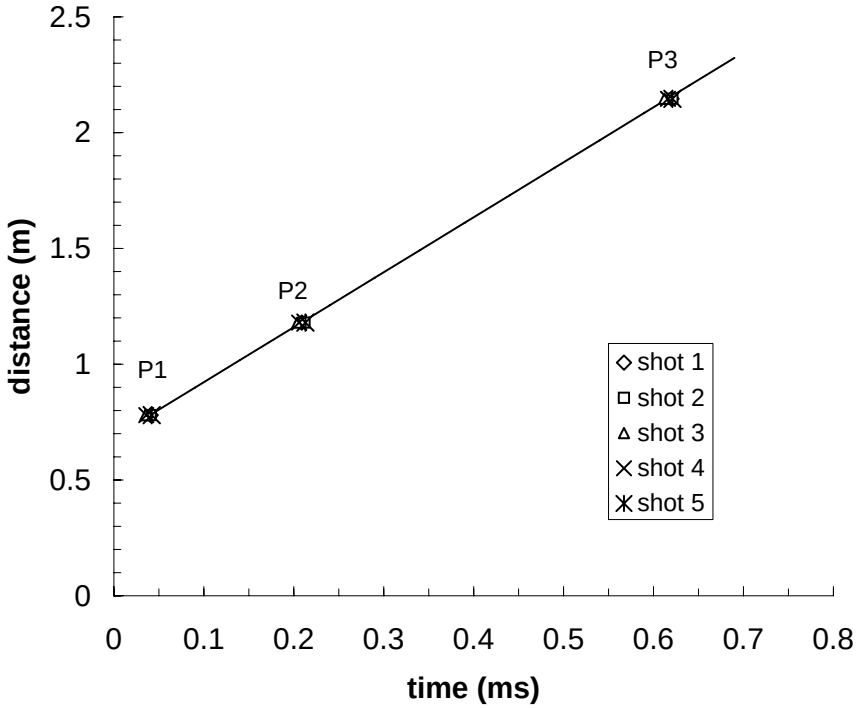

Figure 12: Arrival times of the peak pressures vs. the location of the pressure gages for shots 1-5. $X = 0$ is the ignition location. The line represents a CJ wave trajectory with a speed of 2374 m/s.

The experimental peaks $P3_{max}$ and S_{max} are given in Table 4, for more detail on the individual gages see App. B. The highest strain did not occur on the gage S5 but on gage S3. Examination of the strain signals in App. F shows that this is due to the positive interference of incident and reflected flexural waves. The maximum values of peak strain observed at S3 are on the order of 4000 μstrain, above the conventional plastic limit of 2000 μstrain. Some permanent deformation is apparent in the strain signals with the baseline displaced from zero and damping of the oscillations at the end of the recording period. If the deformations are elastic, the estimated peak strain for the incident wave is 1800 μstrain using (1) with $P_{max} = P_{CJ}$, and $\Phi = 1.5$, consistent with the estimates made by Shepherd et al. (2008). This is comparable to the initial peak values measured on gages S1 to S4. The estimated elastic strain is 5492 μstrain using (1) with $P_{max} = P_{CJref}$, and $\Phi = 2$. The actual values of the peak strains are lower due to the onset of plastic deformation above 2000 μstrain.

The pressure signals P1 and P2 are compared in Fig. 13 with the ideal CJ detonation model and the Taylor-Zeldovich (TZ) similarity solution for the flow behind the wave. The

Table 4: Peak pressure and peak strain for the straight aluminium tube specimen tests for $P_0 = 1$ bar.

shot	P3$_{max}$ (MPa)	S_{max} μstrain
1	8.52	4085
2	9.87	3873
3	9.51	3873
4	9.21	3958
5	8.76	3832

model and application to similar experiments in this fixture is discussed in Liang et al. (2008) and the computational methods are described in Browne et al. (2004). The flow behind the wave used the exact constant-γ perfect gas solution (see p. 28 Liang et al., 2008) with the computed CJ pressure of 3.38 MPa, plateau pressure P_{plat} of 1.24 MPa, and $\gamma = 1.14$. The analytical solutions are only given up to the time of the reflected shock arrival. There is

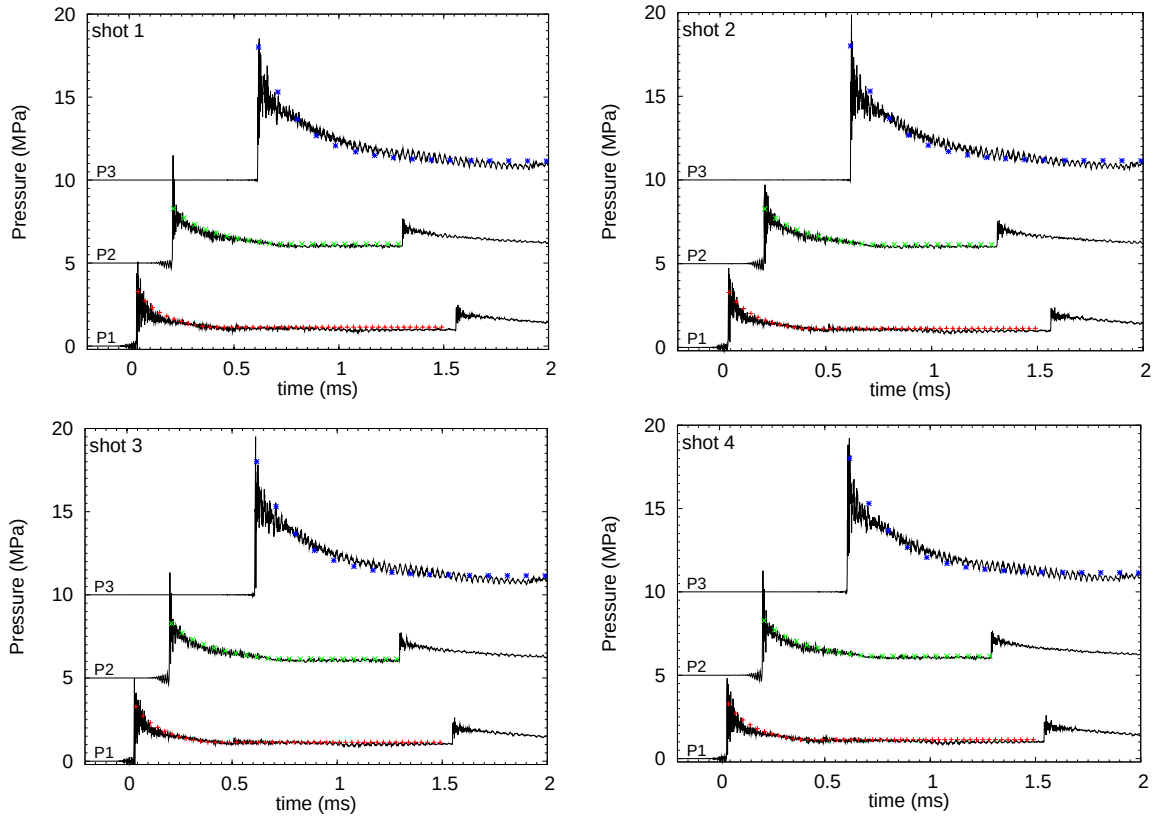

Figure 13: Comparison of measured pressure histories (solid line) with computed or estimated ideal pressures histories (symbols) for shots 1, 2, 3, and 4.

no analytical solution for the pressure signal P3 so we have modeled this using an empirical

function motivated by the success of the exponential decay approximation used by Beltman and Shepherd (2002) to model the TZ analytical solution. The analogous expression we have used to model the reflected pressure history is:

$$P = P_0 \qquad t < t_r \ , \tag{6}$$

$$P = (P_{CJref} - P_{plat}) \exp(-(t - t_r)/\tau_r) + P_{plat} \qquad t > t_r \ , \tag{7}$$

where the ideal peak reflected pressure $P_{CJref} = 8.34$ MPa, t_r is the time of detonation reflection, and τ_r is a characteristic decay time for pressure at the reflecting surface. For an ideal detonation reflecting after propagating a distance L from the initiation point, dimensional considerations suggest that decay time can be written as

$$\tau_r = b \frac{L}{U_{CJ}} \ , \tag{8}$$

where b is a numerical constant. Using a visual fit of the data, we find that b is approximately 1/5. This constant is reasonable since for the TZ solution (Beltman and Shepherd, 2002, Liang et al., 2008), the constant is on the order of 1/3. The reflected shock is moving in the opposite direction of the gas set into motion by the detonation and the time of interaction is therefore smaller than the time needed for the Taylor wave to sweep by the same location. The comparisons shown in Fig. 13 indicate that this approximation should be reasonable for engineering estimates of the forces created by wave reflection. To examine this further, we have integrated the pressure-time histories for the data and the models

$$I'(t) = \int_0^t (P(t') - P_0) \ dt \tag{9}$$

and compared the resulting area-specific impulses I' (N-s/m^2) in Fig. 14. All three traces show reasonable agreement at early times (< 1.5 ms) but increasing differences between models and experimental values occur at late times (> 2.5 ms for P3). This is due to the reduction from the ideal value in the plateau pressure because of heat transfer from the high-temperature combustion products to the cold detonation and specimen tube walls. Following the initial transient, the trend for all gages is a nearly linear increase in area-specific impulse with time. This is a consequence of the almost constant plateau pressure at long times ($>$ 1.5 ms) with some changes in slope (visible at 1.5 ms on P1) due to the shock waves created by detonation reflection. The form of the pressure and impulse histories suggests that as long as the structural response times are sufficiently long compared to the duration of the TZ wave, the applied force can be considered a suddenly-applied constant level corresponding

to the plateau pressure with a superimposed impulse due to the flow transient.

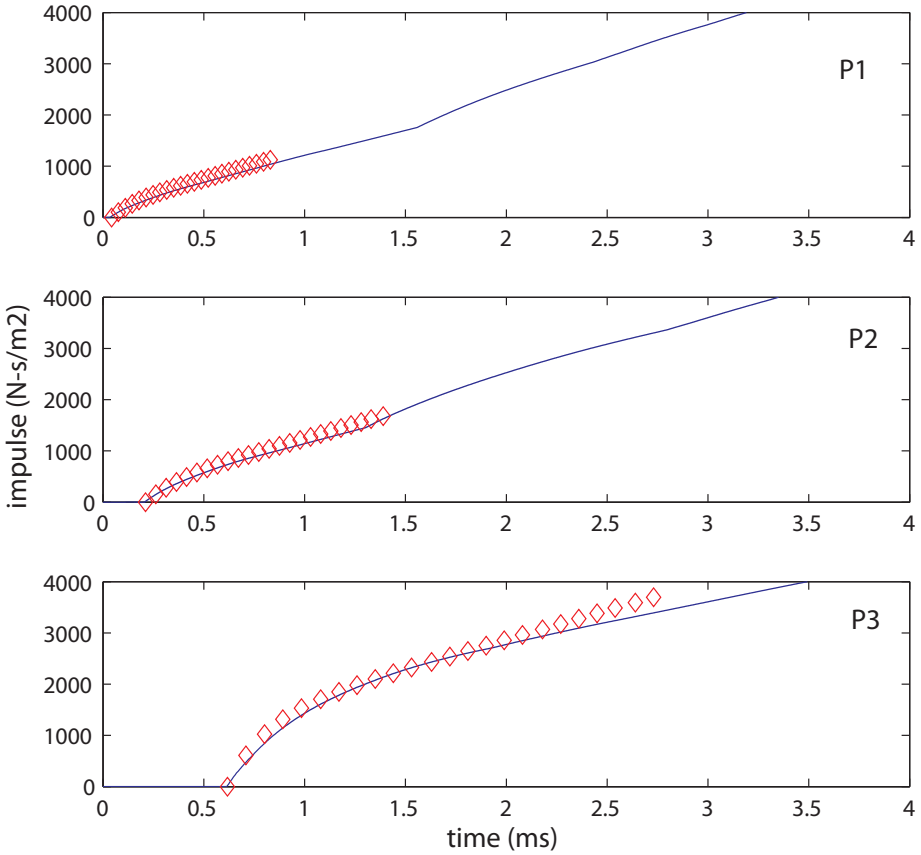

Figure 14: Comparison of specific impulses computed from measured pressure histories (solid line) with analytical approximations to area-specific impulse (symbols) for shot1.

4 Straight steel tube specimen.

The straight steel specimens are 24-in. long segments of Cold-Rolled Electrically Welded (CREW) tubing constructed of ASTM 1008/1010 steel. The nominal outer diameter (OD) of the tube is 1-5/8-in. and the nominal wall thickness is 0.060-in. This is a standard size that can be readily found at industrial metal suppliers. The dimensions and location of the test specimen in the fixture are shown in Fig. 15. The actual thickness of the tubing was quite uniform (Table 19) as determined by a precision ultrasonic thickness gage (Checkline TI-007) and was equal to 0.0609 ±0.0003 in for specimen number 1. The distance of the pressure transducers to the ignition and the distance of the strain gages to the reflecting end are listed in Table 5.

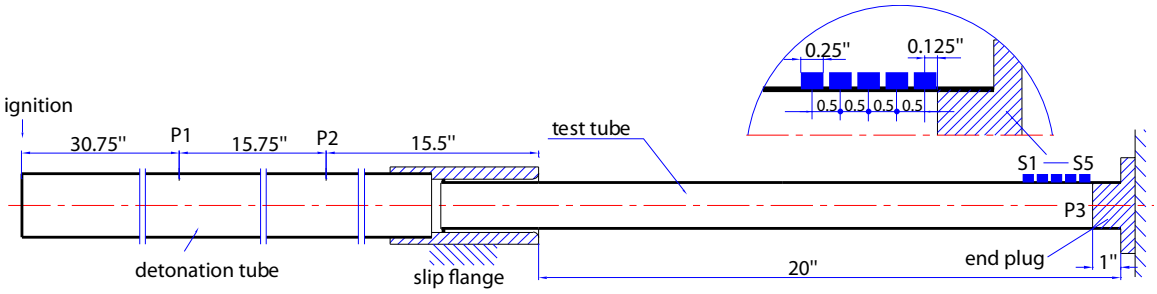

Figure 15: Tube setup and dimensions for the straight steel tube.

Table 5: Distance X of the pressure transducers to the ignition plane and the strain gages to the reflecting end.

	X (m)	X (in)		X (mm)	X (in)
P1	0.780	30.71	S5	3.175	0.125
P2	1.180	46.46	S4	15.92	0.627
P3	2.057	80.98	S3	28.62	1.127
			S2	41.32	1.627
			S1	54.02	2.127

A total of 18 tests (shot 6-23) were performed with the initial pressure P_0 between 1 and 0.05 bar (see the shot summary in Table 6 and Appendix C). When $P_0 \geq 0.10$ bar, the transition to detonation was observed to take place before pressure gage P1. For $P_0 = 0.07$ bar, transition took place between pressure gages P2 and P3. No combustion was observed on the pressure or strain gage signals for $P_0 = 0.063$ or 0.05 bar. This is consistent with the data given in Table 2 and the cell sizes shown in Fig. 8.

As expected for $P_0 = 1$ bar, the pressure traces (see Fig. 16a) are essentially identical to those obtained in shots 1-5, see Fig. 11a. The strain signals show similar high frequency

oscillations close to the expected hoop frequency of 41.4 kHz (24 μs period) for the steel specimens. The hoop oscillations appear to damp much more rapidly for the steel than the aluminum tubes so that the 1 kHz amplitude modulation that is prominent in aluminum is not observed in the steel specimens. The known differences in the damping rates of steel and aluminum (see Chap. V Kolsky, 1963) may be responsible for this effect. The peak strain (see Fig. 18b) due to the incident wave loading is on the order of $\approx$ 300 micro stain and the maximum reflected strain is on the order of 550 μstrain. This a factor of 6 smaller than the strains observed in the aluminum tube due to the differences in thickness and Young's modulus of the steel and aluminum specimens.

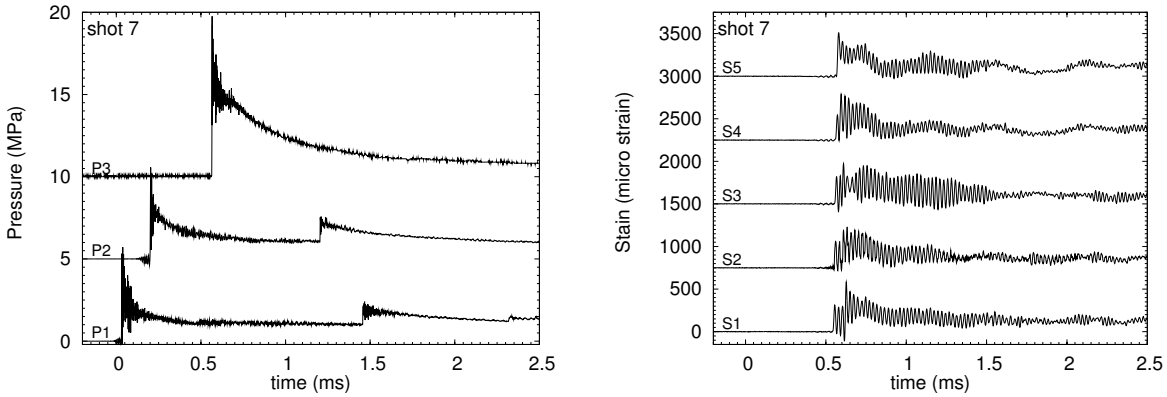

Figure 16: a) Pressure traces and b) strain traces for the steel straight specimen, Shot 7, P_0 = 1 bar.

Analysis of the arrival time data to obtain average detonation wave speeds was carried out and the results are shown in Fig. 17. For initial pressures above P_0 = 0.4 bar, the detonation waves were propagating within $\pm$3% of the CJ velocity. There is substantially more variability in the 1 bar cases (shots 6–11) for the steel tube than for shots 1-5 in the aluminum tube. It is not clear what parameters were uncontrolled but based on past experience, the shot-to-shot variability in wave speed is usually less than $\pm$0.5%. At initial pressure of less than 0.4 bar, the cell size begins to play a role and we would expect increasing deficits in velocity with decreasing initial pressure.

The peak value of the strain signals can be analyzed by finding the dynamic load factor Φ by taking the ratio of the measured peak strain to the peak strain expected in the case of quasi-static loading

$$\Phi = \frac{\epsilon_{exp}}{\frac{\Delta P \bar{R}}{Eh}} \ . \tag{10}$$

For the first peak in the strain signals, the appropriate scaling pressure is the CJ value. At P_0 = 1 bar, the experimental peak strain is about 300 μstrain on gages S1–S4 and from

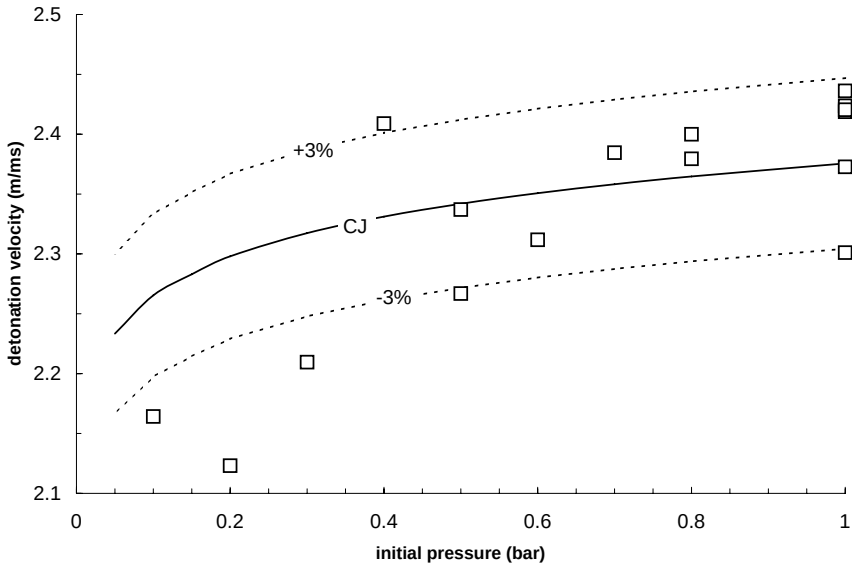

Figure 17: Average detonation speed vs initial pressure.

Table 2, the corresponding static strain is 200 μstrain. This results in $\Phi_{CJ} \sim 1.5$ for the initial peak, which is comparable to what was found for the aluminum tubes in Section 3 and also by Chao (2004) and Shepherd et al. (2008) using this fixture. The highest peak strains are generally found on gage S5, adjacent to the reflecting end plug. Table 4 summarizes the peak strains, pressures, and the dynamic load factors computed with Eqn. 10 and $\Delta P = P_{CJref}$ - P_a.

There are substantial fluctuations in the pressure near the front and these become more pronounced as the pressure is reduced, particularly on gage P3. As shown in Fig. 18a, the peak pressure at P2 lies between P_{CJ} and P_{CJref}, and the peak pressure for P3 is always greater than P_{CJref}. The ratio of peak pressure to reference value is larger for lower initial pressure, i.e. P3 $\approx 2.5 P_{CJref}$ for $P_0 = 0.5$ bar but P3 $\approx 1.13 P_{CJref}$ for $P_0 = 1$ bar. This is a consequence of the dependence of detonation cell width on pressure, see Fig. 8. The measured peak strain correlates very closely with the ideal static $\epsilon_{CJ,ref}$ strain (Fig. 18b) with no systematic effect of initial pressure. This shows that strain measurements are more useful than pressure measurements in characterizing the structural response. The structure averages out the high frequency oscillations that are present in the pressure and provides a more reliable means of measuring the structural loading. The resulting values of Φ_{CJref} are shown graphically in Fig. 19. Leaving aside the lowest initial pressure case, there is no clear trend with initial pressure and $0.8 \leq \Phi_{CJref} \leq 1.2$. At the lowest pressures, the strains are very small and with the instrumentation settings used in these experiments, the values are subject to substantial uncertainty. In addition, the effect of detonation cell width will be

more pronounced at low pressure and as shown by Beltman and Shepherd (2002), this leads to higher values of peak strain.

Table 6: Peak pressure, strain and dynamic load factor based on reflected CJ wave pressure for the straight steel specimen.

shot	P_0 (bar)	$P3_{max}$ (MPa)	S_{max} μstrain	$\Phi_{CJ,ref}$
6	1	9.48	640	1.24
7	1	9.76	583	1.13
8	1	8.8	549	1.06
9	1	8.87	541	1.04
10	1	10.3	555	1.07
11	1	8.05	520	1.00
13	0.8	13.92	461	1.12
25	0.8	12.28	440	1.07
14	0.7	8.53	376	1.05
15	0.6	6.89	306	1.00
16	0.5	9.89	250	0.99
26	0.5	10.4	291	1.15
17	0.4	6.89	197	0.98
18	0.3	6.69	156	1.05
19	0.2	5.25	105	1.08
20	0.1	3.89	62	1.31

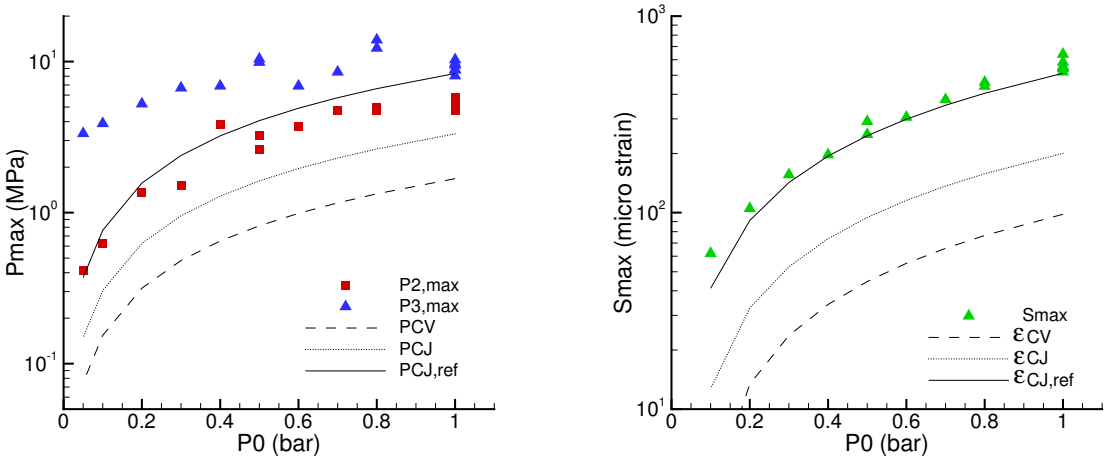

a) b)

Figure 18: a) Peak pressure and b) peak strain for the steel straight specimen.

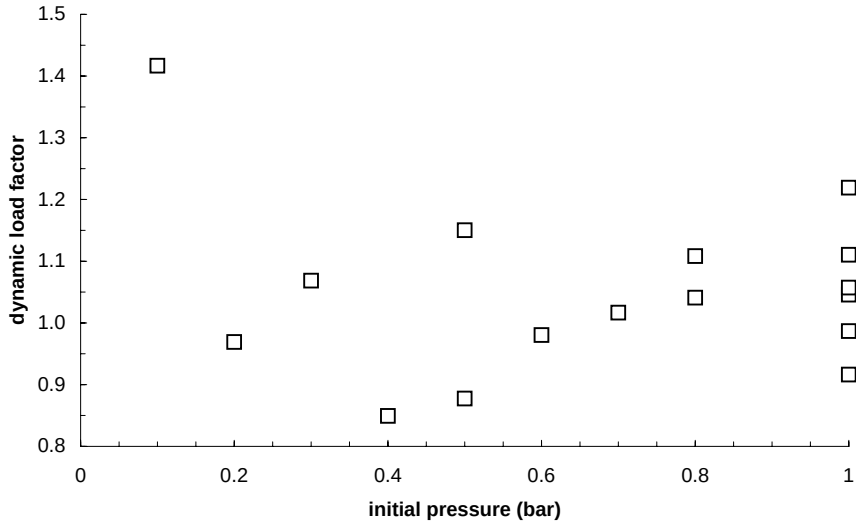

Figure 19: Dynamic load factor vs. initial pressure for the steel straight specimen. Scaling pressure is the peak pressure behind a reflected CJ detonation.

5 Bend Specimens

The bend specimens were made by hydraulic forming about a mandrel using the same stock of material as the straight specimens. There were two specimens, one used for series B-1, and another used for series B-2, -3, and -4. The specimen for series B-1 (Fig. 21) consisted of a 24-in. straight section connecting to the bend which had a radius of 6-in. (measured to the midline of the pipe) completing a 90-degree turn. After the bend, the specimen extended for an additional 12-in. The specimen for B-2, -3 and -4 was similar (Fig. 27) but had a slightly shorter entry section (19.3125 in) and fourteen adapter ports were welded onto the tube and used for mounting pressure transducers. The ports were spaced at 15° intervals, seven on the intrados and seven on the extrados of the bend. The hydraulic bending process created some non-uniformity in the wall thickness which was characterized (Table 20 in App. D) with an ultrasonic thickness gage.

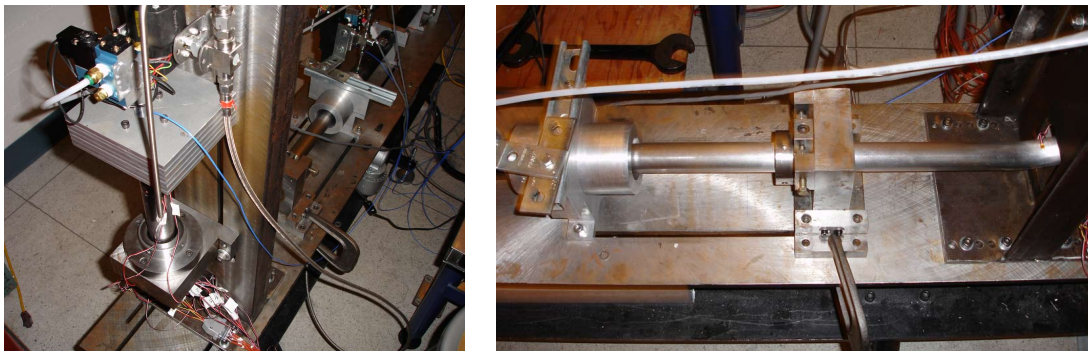

Figure 20: Views of the fixture holding the bend specimen.

The specimen was supported by a vertical U-shaped section of steel channel that was bolted to the main fixture, see Fig. 20. The specimens were terminated by the same end cap and pressure transducer as used in the straight tube specimen tests. Fixed collets were used to grasp the tube just upstream and downstream of the bend, Fig. 20 and 22. This created a "built-in" boundary condition at these locations and prevents the tube from pulling out of the end cap or slip-on junction between the detonation tube and specimen. This mounting method was adopted after initial tests showed that the unrestrained tube was pulled completely off the end plug by the forces created by the detonation propagating through the bend. Four series of tests were performed with the bend specimens (see Table 7). The summaries of each set of tests are given in App. D and a complete set of signal histories given in App. H.

Table 7: Summary of Bend test series. "PT" represents the pressure transducer and "SG" represents the strain gage.

Series	Setup	Shots	P_0 (bar)	Note
B-1	Fig. 22	29-39	0.05-1	15 SG and 3 PT
B-2	Fig. 26	81-91	0.2-1	10 PT, 7 on intrados
B-3	Fig. 26	94-101	0.15-1	10 PT, 7 on extrados
B-4	Fig. 31	103-108	0.1-1	10 PT, 3 intrados and 4 extrados

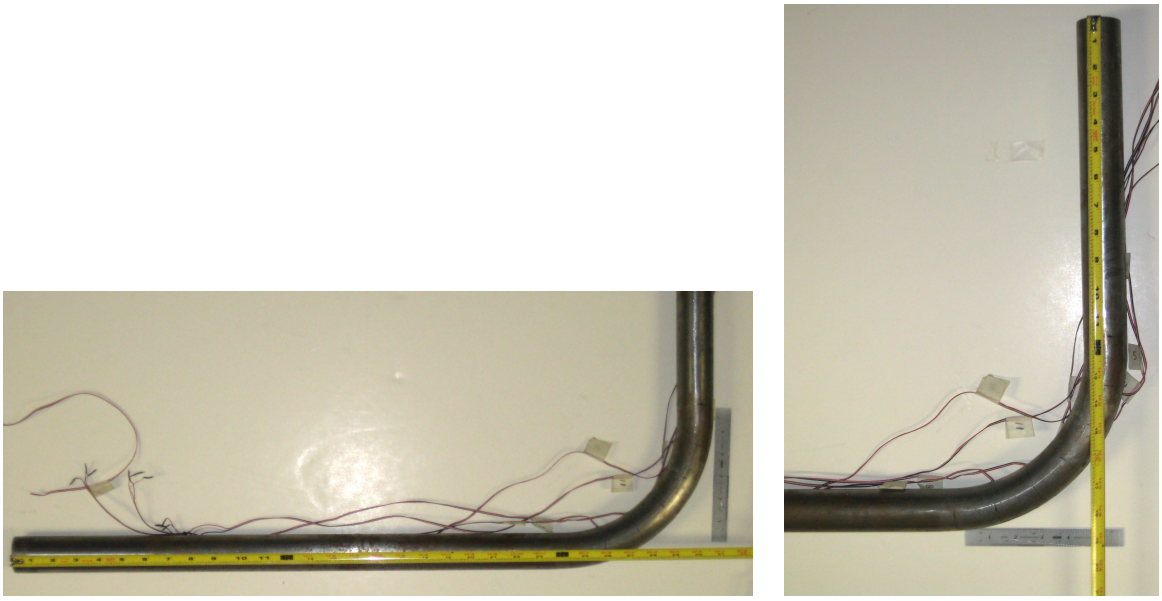

a) b)

Figure 21: The bend specimen used for hoop strain measurements in series B-1. a) Horizontal leg, b) vertical leg. Gage 12 is missing in this post-test photograph. The gray lumps are Dow Corning 3145 RTV adhesive/sealant used to secure the strain gage wires to prevent tearing the wiring from the solder pads.

5.1 Test series B-1

For test series B-1, three pressure transducers (P1-P3) were used with two on the main tube and one on the closed end, and fifteen strain signals were measured along the test specimen. Strain gages S1-S12 were placed on the bend in hoop orientation along the midplane of the specimen. As illustrated in Fig. 22, the gages S1-S6 were placed every 15 degrees along the extrados of the bend. Gages S7 to S12 were placed every 15 degrees along the intrados of the bend. Gages S13-S15 were placed at the termination end of the specimen, as shown in the inset of Fig. 22. The distance of strain gages S1-S12 to the ignition plane is listed in Table 8. This distance was measured both along the surface of the tube (columns labeled intrados or

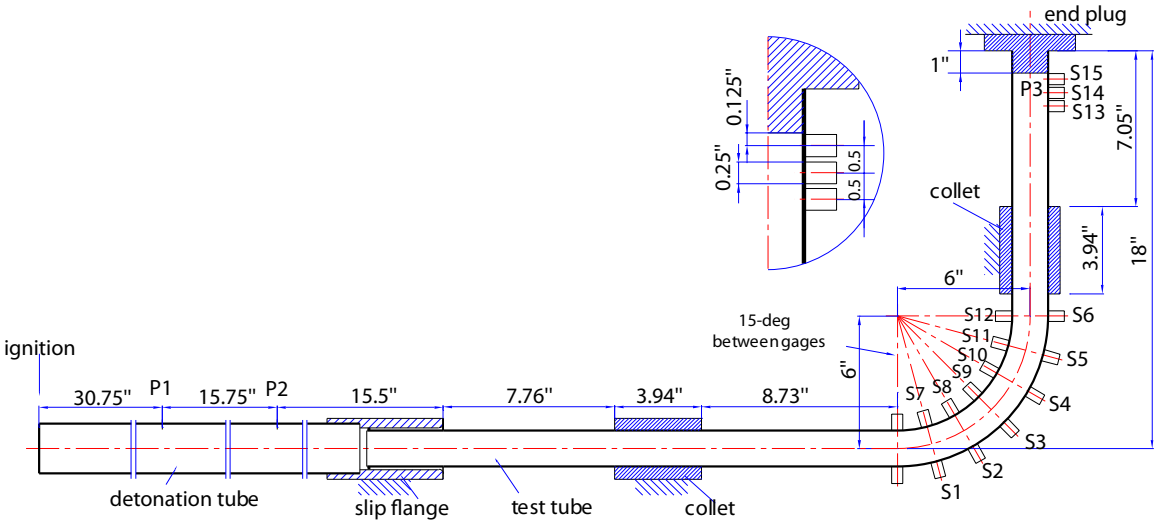

Figure 22: Layout of the 15 strain gages and 3 pressure gages on the bend specimen for test series B-1. See Table 8 for gage locations.

extrados) or as a distance along the centerline of the tube corresponding to projecting the gage location in the direction normal to the local wall orientation.

Table 8: Distance of the pressure and strain gages to the ignition plane for series B-1. Distance in the first column (labeled intrados or extrados) is measured along the surface of the tube in the plane of the bend. The distance in the second column (labeled centerline) are the nominal distances along the mean centerline of the tube.

Gage	X (m)	X (in)	X (m)	X (in)
	Extrados		Centerline	
P1	-	-	30.75	0.781
P2	-	-	46.50	1.181
S1	2.139	84.29	84.00	2.134
S2	2.184	85.97	85.57	2.173
S3	2.229	87.74	87.14	2.213
S4	2.274	89.51	88.71	2.253
S5	2.319	91.28	90.28	2.293
S6	2.363	93.05	91.85	2.333
	Intrados		Centerline	
S7	2.129	83.81	84.00	2.134
S8	2.164	85.19	85.57	2.173
S9	2.199	86.57	87.14	2.213
S10	2.234	87.95	88.71	2.253
S11	2.269	89.33	90.28	2.293
S12	2.304	90.71	91.85	2.333
P3	-	-	102.60	2.606

A total of 11 tests were performed in series B-1, varying the initial pressure from 1 bar to 0.05 bar. A summary of the tests is given in Table 21 and Appendix D; the full data plots are given in Appendix H. The distortion of the detonation wave as it travels around the bend creates differences between the pressures and strains experienced by the inside and outside of the bend region. Pressure measurements downstream of the bend (see the next section) indicate these effects diminish with distance and by the time the wave reaches the end of the specimen, the loading is very similar to that experienced by the straight tube.

The peak pressures at P1 and P2 (see Fig. 23) are on the order of 5 MPa, which are similar to shot 7 for the straight specimen, but the reflected peak pressure P3 is 14.4 MPa, almost 1.5 times larger than the value recorded in shot 7. However, these peak pressures appear to be due to a spike at the wave front which is extremely short in duration and aside from this feature, the overall pressure-time histories are very similar for the bend and straight specimens. This is reasonable since the detonation cell size (< 1 mm) is quite small compared to the bend radius (150 mm) and the pressure gage P3 is located more than 7 tube diameters downstream of the bend exit.

The peak strain on the intrados of the bend is about 200 μstrain due to the incident waves and 330 to 450 μstrain due to the reflected waves (see Fig. 24a). The peak strain on the extrados of the bend (Fig. 24b) is about 300 μstrain due to the incident wave and 350 to 575 μstrain due to the reflected wave. The strain values on the extrados are higher than on the intrados, consistent with the difference in peak pressures expected due to the diffraction of the detonation wave. Diffraction is associated with higher pressures on the extrados due to the increase in amplitude due to reflection of the detonation wave and lower pressure on the intrados due to generation of expansion waves by the flow turning through the bend.

The average of intrados and extrados values of strain are comparable to those observed for the straight tubes, about 300 μstrain peak for the incident waves and 550 μstrain for the reflected waves (18). For the first 0.5 ms after wave arrival, strain gages S13–S15 near the end of the tube have strain histories (Fig. 24c) that are very similar to the corresponding gages on the straight specimens (Fig 16b). The maximum strain magnitude on gages S13-S15 is approximately 600 μstrain. The effect of the bend on the detonation wave and the measured strains at the end of the specimen appears to be modest for the first 0.5 ms following wave arrival. This is to be expected not only for the reasons given at the end of the previous paragraph but in the case of the strains, the collet located just downstream from the end of the bend provides a very strong restraint on the tube motion due to the bend forces.

At longer times, 10-20 ms following wave arrival, the strain measurements on the bend specimens show features not seen in the straight tubes. We interpret these as strains created by the structural oscillations resulting from the forces associated with the geometry of the

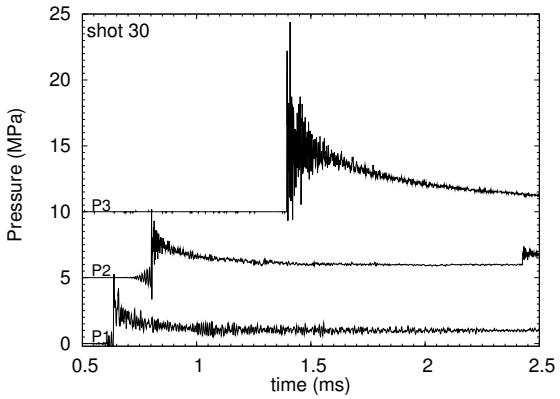

Figure 23: Pressure traces for test series B-1 of shot 30. P_0=1 bar.

bend. These structural oscillations can be seen on the long time scale plot of Fig. 24d. These oscillations are much longer in period (≈4 ms) than the hoop oscillations that are initially excited by the arrival of the detonation or reflected shock wave. The hoop oscillations that are clearly observed in Fig. 24c, appear as very high-frequency ringing or noise superimposed on the low frequency structural oscillation when the strain is plotted over a long time scale, Fig. 24d. The structural oscillations may be due to the bending, coupled bending-torsion-hoop distortion modes of the tube, or due to the flexibility of the mounting system used to support the vertical leg of the tube. An A36 steel channel (C10 x 15.3 channel, which has a cross section of 10 in x 2-1/2 in x .240 in) was clamped to the main support I-beam and used to mount the collet and tube end plug, see Fig. 20. This channel may be bending and causing relative motion of the collet and end plug, creating the long-time variations in strain that are visible on gages 13, 14, and 15, which are closest to the end.

Table 9 and Fig. 25 give the maximum peak strain at the intrados $S_{intrados,max}$ (the maximum of S1-S6), extrados $S_{extrados,max}$ (the maximum of S7-S12) and the reflecting end $S_{end,max}$ (the maximum of S13-S15). The maximum strains were always observed close to the closed end due to the shock waves created by the reflection of the detonation. The peak strain on the extrados and intrados were comparable for all initial pressures. With the exception of the lowest pressures, the data are bounded by two estimates shown on Fig. 25. The lower bound is given by (1) using the CJ pressure and $\Phi = 2$; the upper bound is given by (1) using the Reflected CJ pressure and $\Phi = 1.25$. The upper bound is consistent with the values for Φ computed from the straight tube data, see Table 6. The results at the lowest pressure lie well above the bounds. This is because that test resulted in DDT at the tube end, producing exceptionally high pressures and strains. The peak strains at each location are summarized in Figs. 58 in Appendix D.

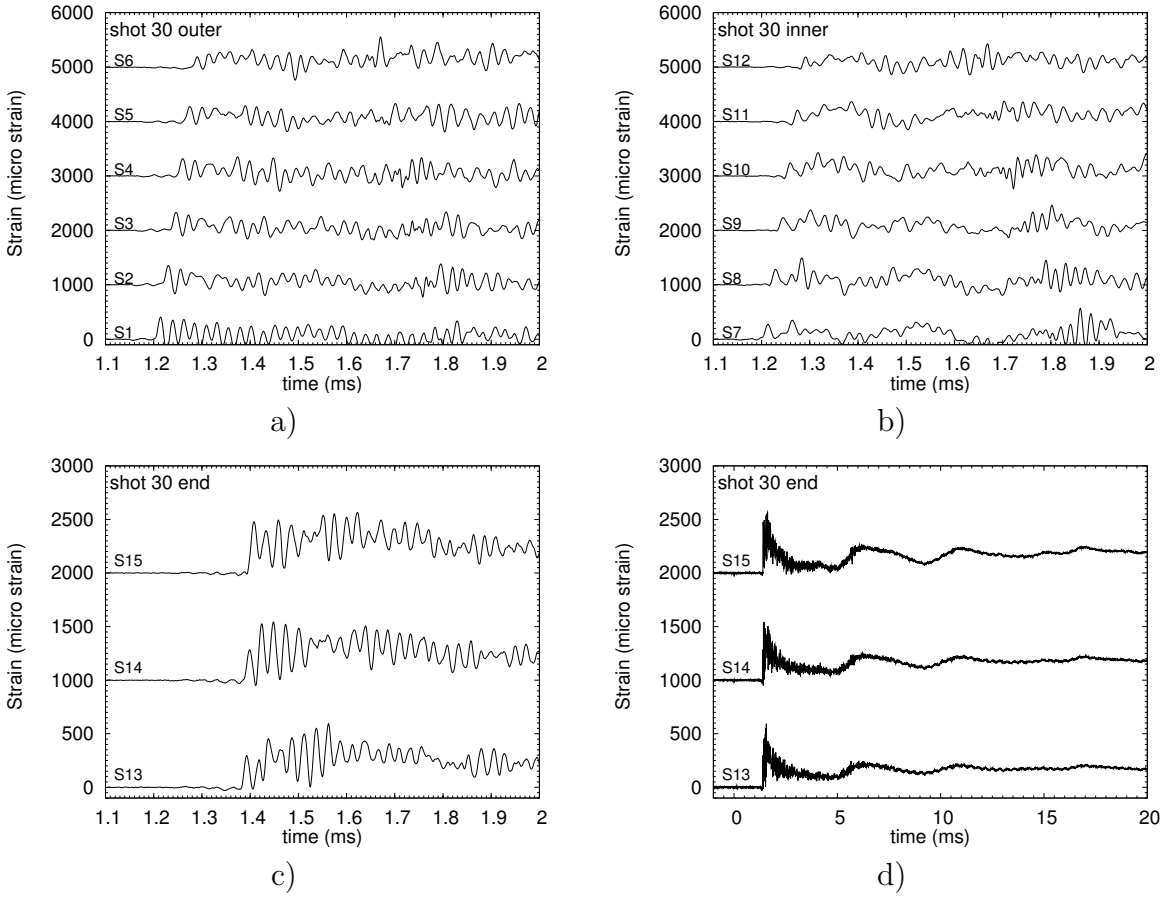

Figure 24: Strain gage traces for (a) extrados (S1 - S6), (b) the intrados (S7 - S12), (c) end (S13 - S15), early time and (d) end, late time. Shot 30 and P_0=1 bar.

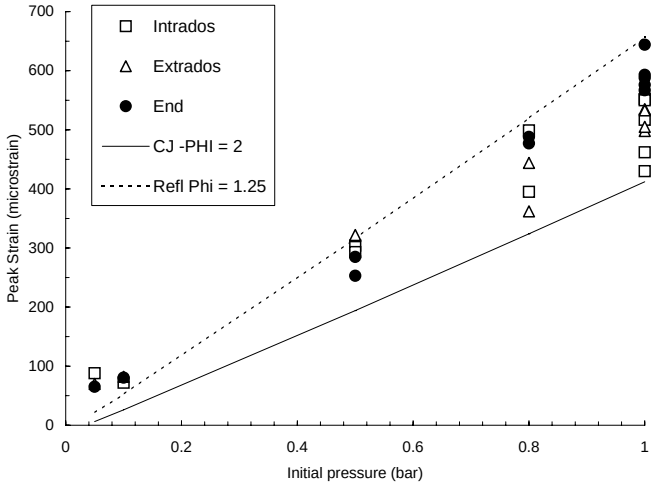

Figure 25: Peak strain vs initial pressure at extrados (S1-S6), intrados (S7-S12) and reflecting end (S13-S15) for the bend specimen. Test series B-1.

Table 9: Maximum stain at the extrados(S1-S6), intrados (S7-S12) and reflecting end (S13-S15) for the bend specimen.

shots	P_0	$S_{intrados,max}$	$S_{extrados,max}$	$S_{end,max}$
29	1	430	498	576
30	1	552	570	593
31	1	517	535	644
32	1	550	505	567
33	1	462	533	588
34	0.8	395	362	477
35	0.8	499	444	488
36	0.5	304	320	285
37	0.5	293	322	253
38	0.1	72	82	80.5
39	0.05	88	70	65.1

5.2 Test series B-2 and B-3

In order to measure pressure signals at points on the bend, a special specimen tube was designed and fabricated. As shown in Fig. 26 and 27, fifteen pressure transducer adaptors were welded on the tube at the locations corresponding to the strain gages in test B-1. In test series B-2, the extrados adapters were instrumented and the intrados adapters were plugged, and vice-versa for test series B-3. The distance of the pressure gages to the ignition plane is listed in Table 10. We have given both the distance along the tube surface and the mean distance as measured along the tube centerline.

Table 10: Distance of the pressure gages to the ignition plane for tests B-2, B-3, and B-4.

Gage	Extrados		Intrados		Centerline	
	(m)	(in)	(m)	(in)	(m)	(in)
P1	0.78	30.71	0.78	30.71	0.78	30.7
P2	1.18	46.46	1.18	46.46	1.18	46.5
P4	1.980	77.95	1.980	77.95	1.98	77.9
P5	2.025	79.72	2.015	79.33	2.02	79.5
P6	2.070	81.50	2.050	80.71	2.06	81.1
P7	2.115	83.27	2.085	82.09	2.10	82.6
P8	2.160	85.04	2.120	83.46	2.14	84.2
P9	2.205	86.81	2.155	84.84	2.18	85.8
P10	2.250	88.58	2.190	86.22	2.22	87.4
P3	2.500	98.42	2.500	98.42	2.50	98.42

A total of 19 tests were carried out in series B-2 and B-3 with the initial pressure varying

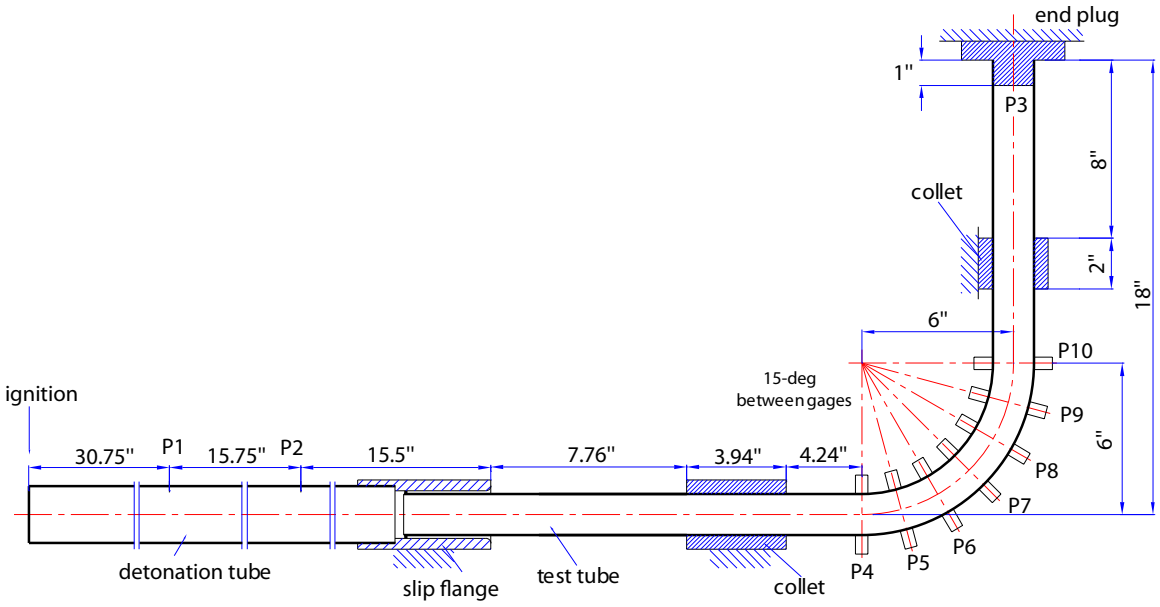

Figure 26: Locations of the 10 pressure gages for the bend specimen for test series B-2 and B-3.

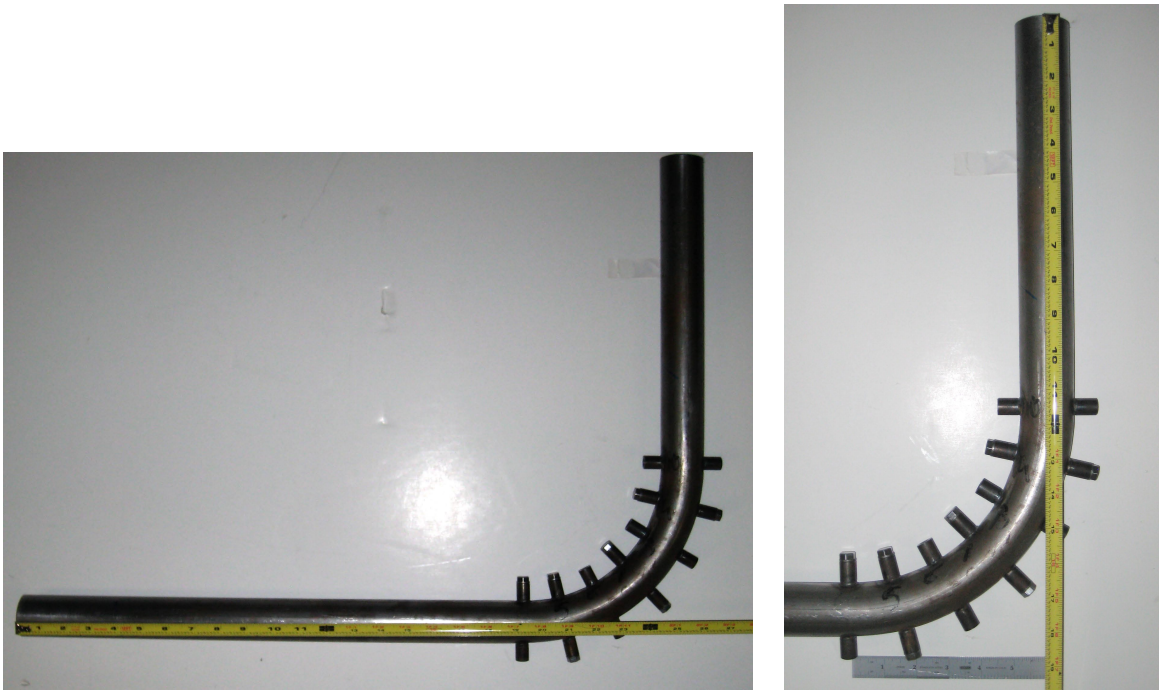

a) b)

Figure 27: The bend specimen used for pressure measurements. a) Horizontal leg, b) vertical leg. Note that the horizontal leg is shorter than the specimen used for the strain gages but the vertical legs are approximately the same length.

from 1 bar to 0.2 bar. A summary of the tests is in Tables 11 and 12, and Appendix D; the full data plots are given in Appendix H.

Table 11: Peak pressure for the bend specimen tests at 10 intrados locations. Test series B-2.

shot	P_0	P1	P2	P4	P5	P6	P7	P8	P9	P10	P3
	(bar)	(MPa)									
		–	–	0°	15°	30°	45°	60°	75°	90°	–
81	0.1	5.470	4.188	3.981	3.715	3.425	5.163	–	4.437	4.451	17.53
82	0.1	5.091	4.153	3.948	3.285	3.420	4.592	4.257	4.663	4.233	15.95
83	0.1	4.971	4.011	3.698	3.261	3.482	4.116	4.968	4.382	4.033	17.93
84	0.1	4.691	4.257	3.631	3.083	3.383	3.708	4.423	4.120	3.984	17.52
85	0.08	3.864	4.094	2.699	2.367	2.516	3.007	4.256	3.327	3.318	14.16
86	0.08	3.482	3.843	3.115	2.588	2.745	3.504	4.594	2.943	3.162	13.10
87	0.05	6.745	2.884	2.315	1.971	2.066	2.379	2.612	2.360	2.625	9.16
88	0.05	1.845	2.016	1.949	1.883	2.047	2.327	3.388	2.787	2.165	10.54
89	0.03	0.359	0.485	2.765	2.451	1.480	2.343	2.169	1.072	1.341	21.73
90	0.02	0.093	0.059	0.067	0.033	0.038	0.038	0.033	0.045	0.051	0.136
91	0.015	0.868	0.930	0.716	0.380	0.796	2.108	0.544	0.640	0.697	4.332

Table 12: Peak pressure for the bend specimen tests at 10 extrados locations. Test series B-3.

shot	P_0	P1	P2	P4	P5	P6	P7	P8	P9	P10	P3
	(bar)	(MPa)									
		–	–	0°	15°	30°	45°	60°	75°	90°	–
94	1	5.405	4.220	4.731	5.818	8.011	11.333	9.718	7.320	6.616	17.107
95	1	5.472	4.525	4.198	5.449	7.562	7.930	8.741	6.439	6.410	16.988
96	0.8	4.142	3.263	3.448	4.249	6.405	6.623	7.950	5.235	5.797	14.839
97	0.8	4.106	3.266	3.648	4.626	7.077	6.598	8.249	5.704	6.983	14.395
98	0.5	1.576	1.995	2.865	3.851	5.292	5.367	7.511	5.125	4.232	10.916
99	0.5	2.549	2.343	1.866	2.634	3.838	4.218	5.877	4.035	3.643	9.534
100	0.3	1.722	2.107	1.033	1.285	1.079	1.690	3.647	1.545	1.139	7.164
101	0.2	0.252	5.326	1.199	1.807	2.542	2.080	3.970	1.613	1.565	7.402

Selected pressure traces are shown in Figs. 28. Peak pressures are given in Table 11 for the intrados and Table 12 for the extrados. Comparison of the tabulated values reveals that the peak values on the extrados are all larger than those in the intrados. As expected from previous studies (Edwards et al., 1983, Williams and Thomas, 2002, Henshaw et al., 1986) on shock and detonation diffraction, compression waves were created on the extrados and

expansion waves were generated on the intrados as the wave turned to remain normal to the tube surface.

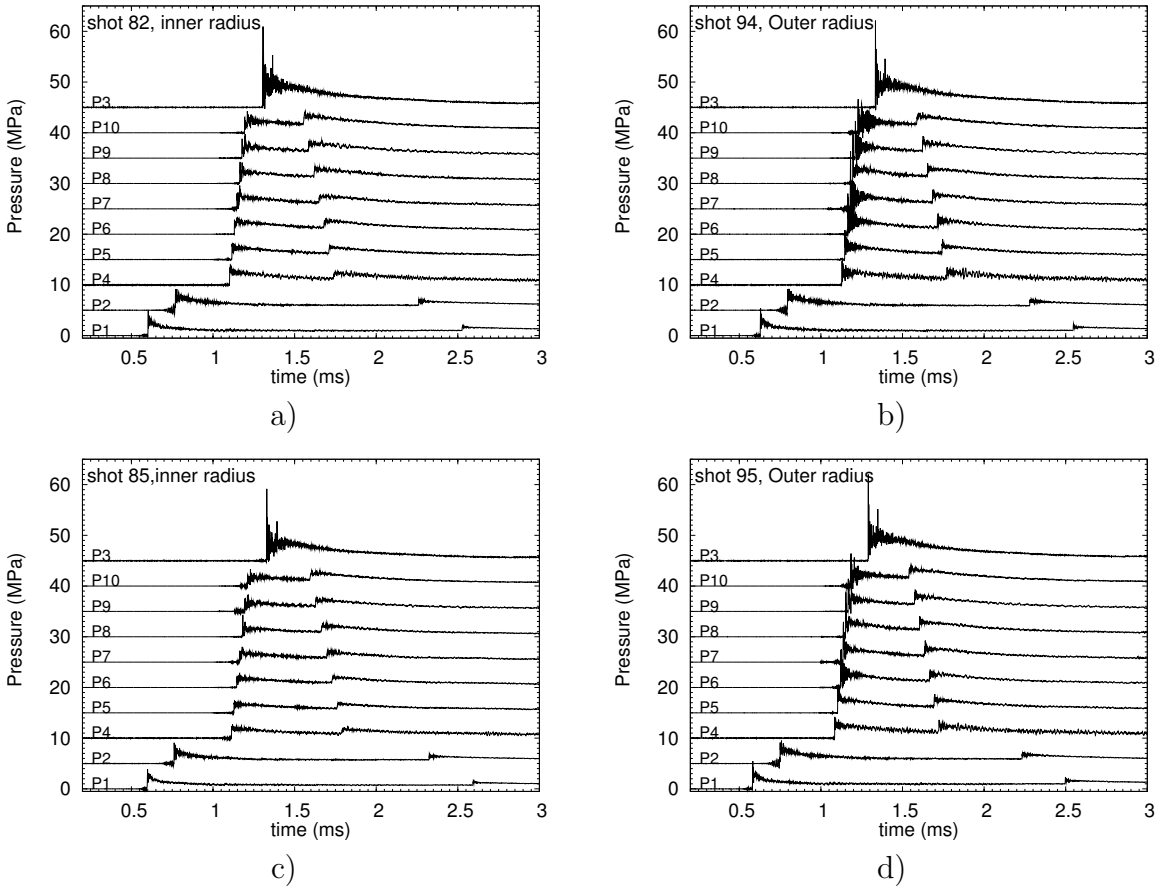

Figure 28: Pressure traces for the bend specimen tests for a) shot 82 (intrados) and b) shot 94 (extrados) at P_0=1 bar, c) shot 85 (intrados) and d) shot 95 (extrados) at P_0=0.8 bar.

The peak pressure and the wave velocity, which was computed using the arrival time of the peak pressure, are plotted in Figs. 29. For $P_0 = 1$ bar, before the bends, the peak pressure is about 1.3-1.6 times of P_{CJ} then it decreases in the intrados to a minimum of P_{CJ} at 30 degrees of the bends, then increases back to the same value at the 90 degrees. On the extrados, the peak pressure increases to a maximum of 3-3.5 times of P_{CJ} at a point between 45-60 degrees and then decreases to 2 times of P_{CJ} at the end of the bends. The detonation velocity in the extrados increase to 1.4 U_{CJ} close to the 75 degrees while in the intrados it decreases to 0.8 U_{CJ} at 60 degrees.

The pressure arrival times have been used to construct the x-t diagrams shown in Fig. 30. Regression analysis of the data has been used to determine wave speeds. The data have been adjusted to compensate for the small variation in arrival time that occurs due to the DDT initiation process. The adjustment was to add a constant to the time of arrival so that all

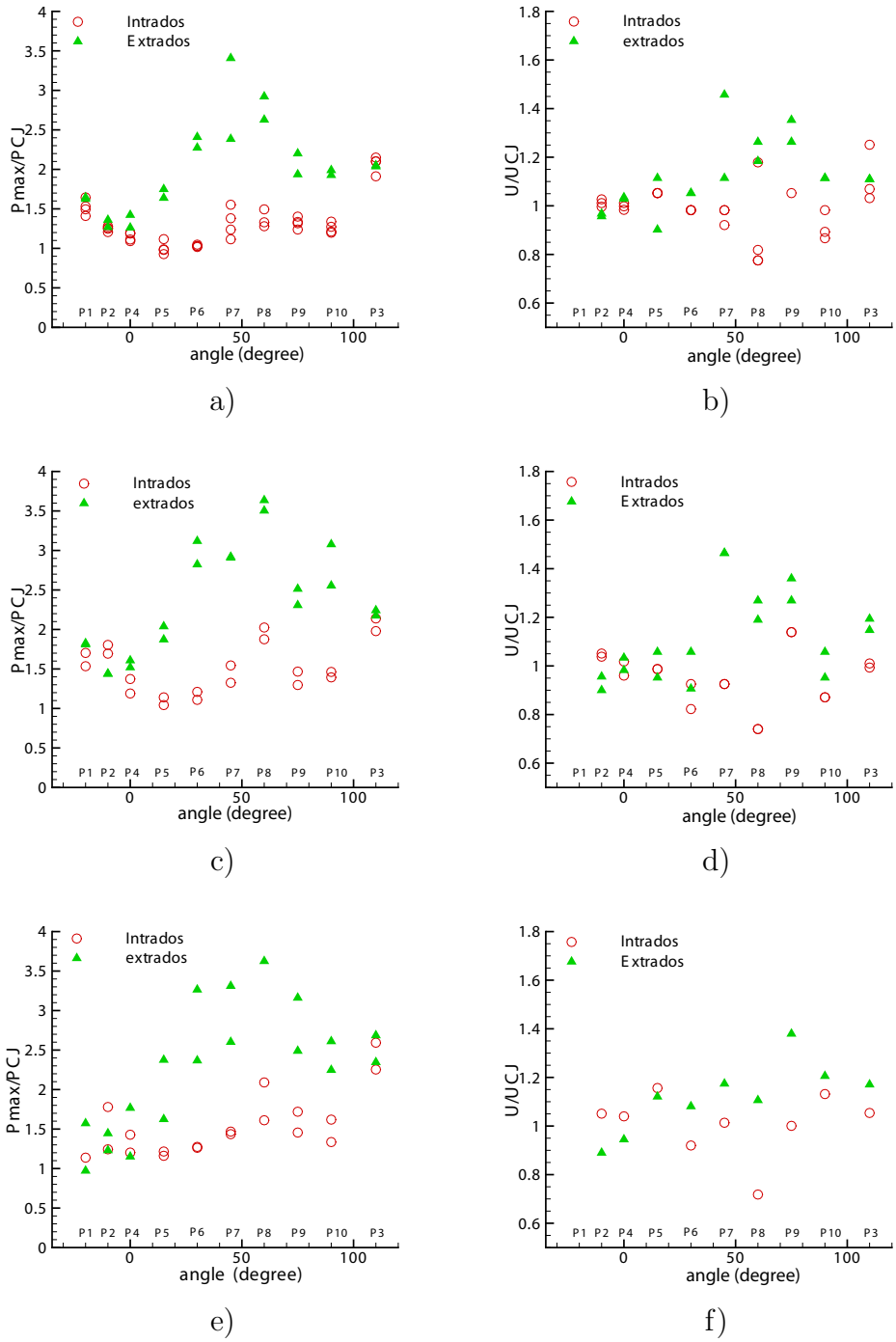

Figure 29: Peak pressure (left column, normalized by P_{CJ}) and detonation speed (normalized by U_{CJ}, right column) vs. location (angle) for (a) $P_0 = 1$ bar, (b) $P_0 = 0.8$ bar and (c) $P_0 = 0.5$ bar.

shots appeared to reach gage P2 at the same time. Analysis of the wave speed indicates that the detonation wave propagates at very close (within 0.5%) to the CJ velocity before reaching

the bend and appears to be slightly overdriven (up to 1.5%) upon emerging from the bend, as shown by the displacement of the points for gage P3 below the CJ trajectory shown in Fig. 30a. There are very small variations in velocity through the bend but overall, the data points are an excellent fit (R=0.9999) to a linear relationship with average speeds within +3.1% and -1.1% of the computed CJ speed of 2375.6 m/s over the combined detonation and specimen tube length.

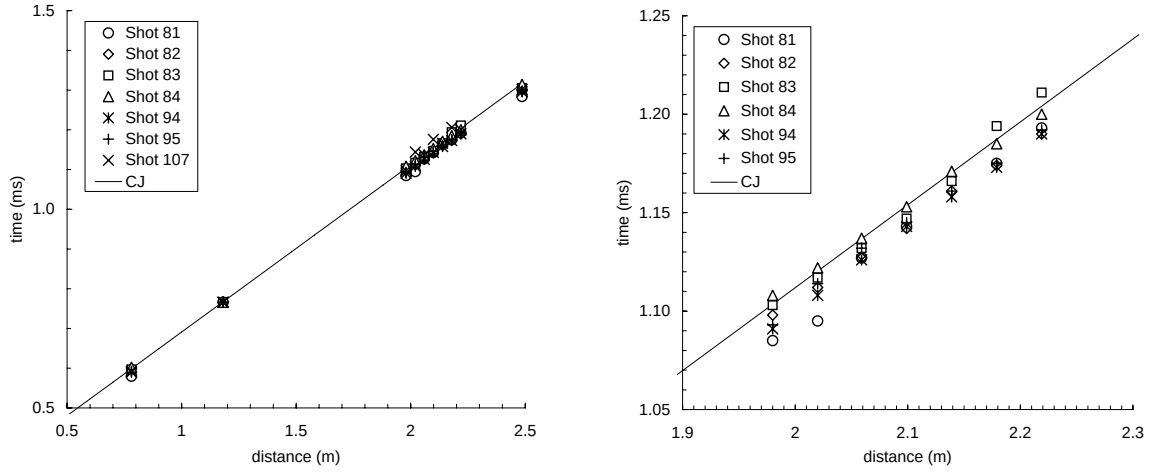

a) b)

Figure 30: (a) Peak pressure arrival time vs. the location of the pressure gages for shots at $P_0 = 1$ bar; (b) enlargement showing the region of the bend.

5.3 Test series B-4

In test B-2 and B-3, we found the results of the lower initial pressure shots were not repeatable because: (1) the mixtures were not well mixed at low pressures (the diaphragm pump performs poorly at low pressure); (2) DDT occurred in the specimen tube instead of immediately after the ignition as it did for higher P_0. This made it difficult to compare intrados and extrados pressure measured in separate shots. Therefore we repeated several shots measuring pressures at the intrados and extrados simultaneously (see Table 13. The labels for the pressure transducers are shown in Fig. 31.

Figure 32 shows the pressure traces. DDT occurred within the bend region for $P_0 = 0.1$ bar, at the higher pressures, DDT occurred upstream of the bend specimen. The pressure peak arrival times were analyzed on an x-t diagram and the results are given in Fig. 33. The arrival times have not been adjusted so that the delay during DDT results in the upward displacement of the trajectories with decreasing initial pressure and increasing delay time. The offset in arrival times between intrados and extrados can now be observed quite clearly

and consistently for pressures between 0.3 and 1 bar. The scatter observed in Fig. 30 has been eliminated.

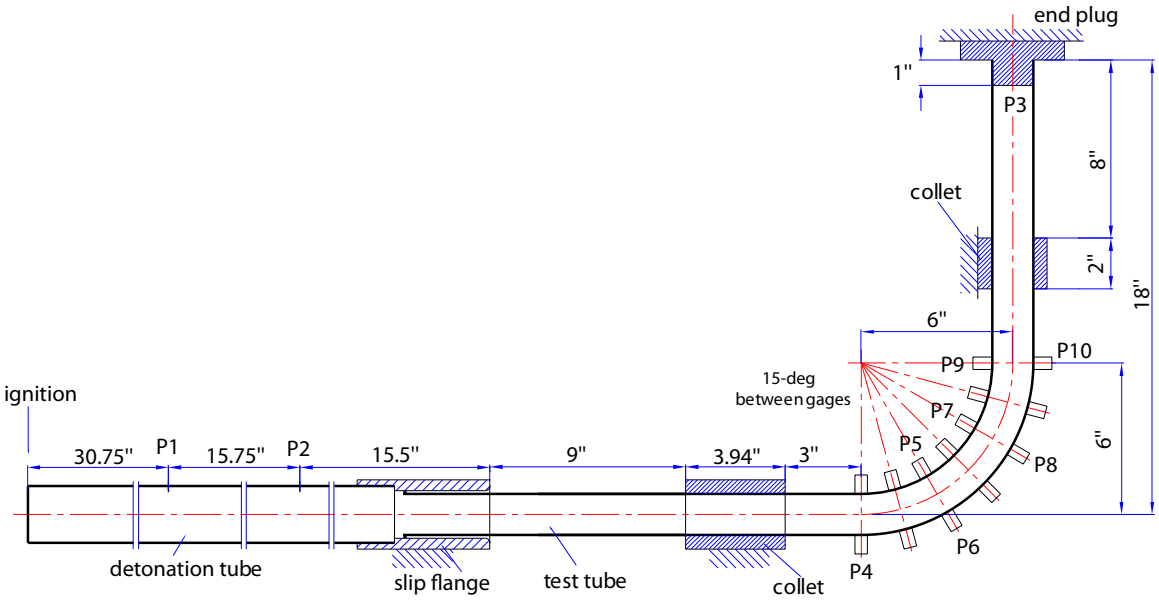

Figure 31: Locations of the 10 pressure gages (extrados & intrados) for the bend specimen and test series B-4. The specimen is the same as used for tests B-2 and B-3 but the location of the lower collet is slightly different.

Table 13: Peak pressure for the bend specimen at 10 locations (see Fig. 31). Test series B-4.

shot	P_0	P1	P2	P4	P5	P6	P7	P8	P9	P10	P3
	(bar)	(MPa)									
		–	–	0°	30°	30°	60°	60°	90°	90°	–
		–	–	ex	in	ex	in	ex	in	ex	–
107	1	5.218	4.372	4.364	3.032	8.104	4.724	7.917	4.618	5.715	15.811
106	0.8	4.406	3.558	3.415	2.458	6.650	4.111	7.021	3.273	4.607	12.434
105	0.5	2.223	2.085	2.016	1.510	4.846	2.710	5.913	2.125	3.015	10.489
103	0.3	1.335	1.765	1.083	0.770	2.666	1.220	3.697	1.293	1.821	6.618
104	0.2	0.982	1.803	0.933	0.551	1.305	1.100	2.130	0.865	0.804	7.692
108	0.1	0.175	0.204	0.816	0.376	1.630	0.419	1.639	0.492	0.970	3.496

5.4 Comparison of Ideal and Measured Pressure Histories

The x-t diagrams of Fig. 30 and 33 indicate that the detonation travels through the bend with a mean speed close the CJ velocity, slightly lagging on the extrados and leading on the intrados. This suggests that the simplest model of the pressure distribution within the bend

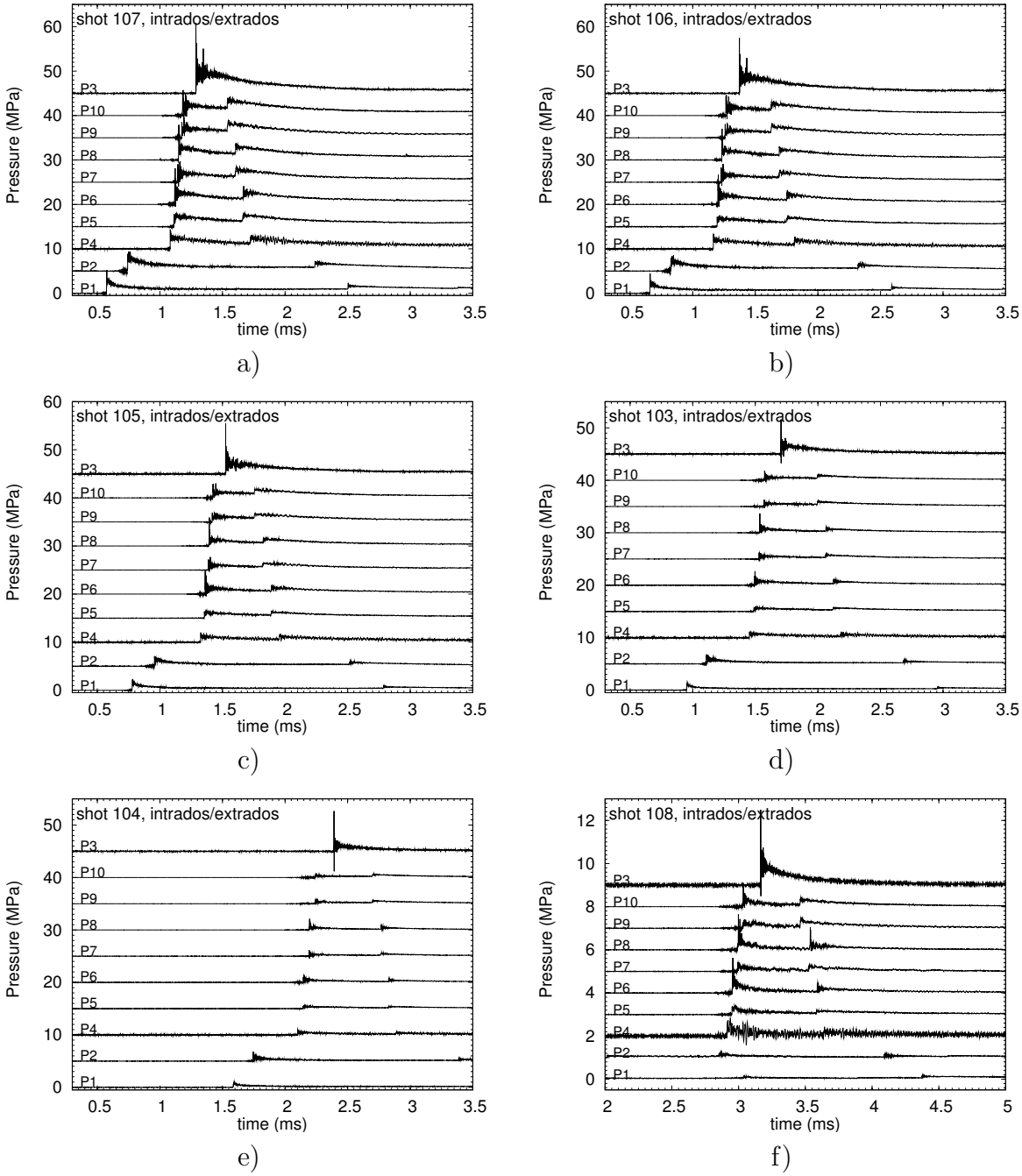

Figure 32: Pressure traces for the bend specimen, test series B-4. a) P_0=1.0 bar (shot 107), b)P_0=0.8 bar (shot 106),c) P_0=0.5 bar (shot 105), d)P_0=0.3 bar (shot 103), e) P_0=0.2 bar (shot 104) and f) P_0=0.1 bar (shot 108).

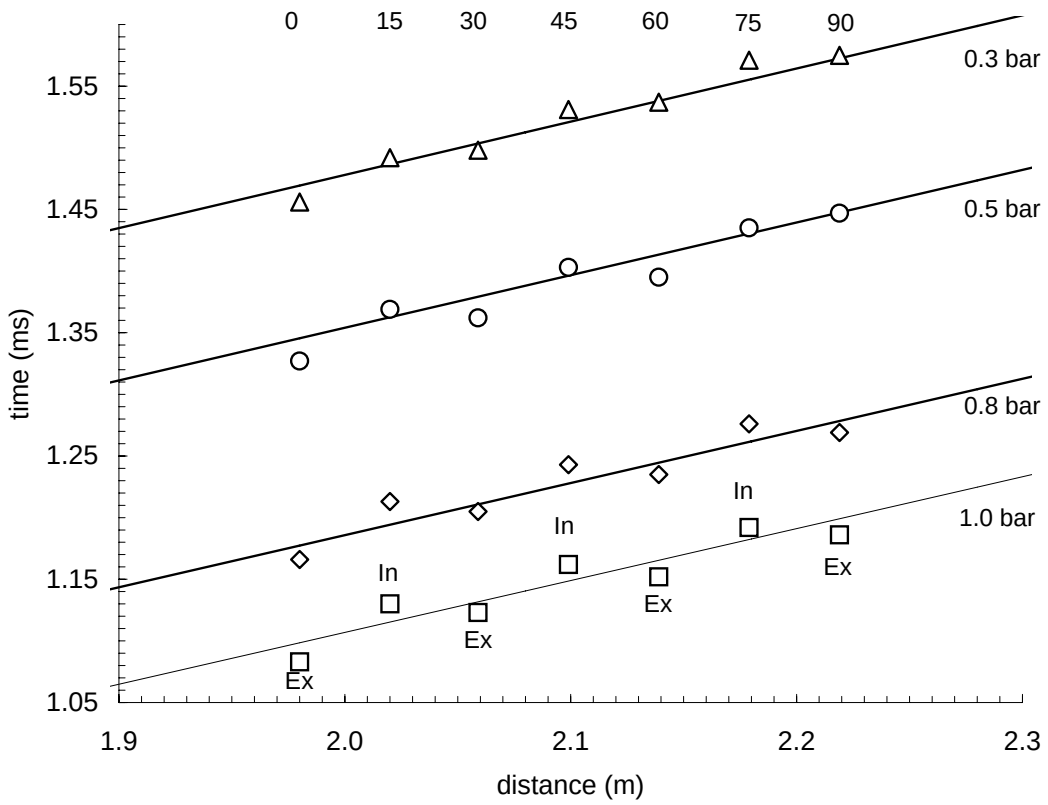

Figure 33: Detonation front trajectories within the bend for shots 107-103 in the B-4 series. The line slopes correspond to the CJ velocity at each pressure. The points are labeled according the location of the gage on the intrados (In) or extrados (Ex) of the bend and the angular location of the gage is shown at the top of the plot.

is to neglect the slight variations in speed and assume that the pressure is given by the ideal TZ model with the wave front traveling along the centerline of the bend at the CJ speed. Obviously, this is not an accurate model for the fine details of the pressure distribution but may be useful for developing traveling load models for finite element simulations of bends to detonations. A comparison between the TZ model and pressure data from two tests is shown in Fig. 34. The TZ profiles have been adjusted so that the wave fronts coincide with the experimental data at the entrance to the bend (gage P4).

The pressure signals on the extrados, Fig. 34b, show high-frequency oscillations which are an artifact of the vibration of the pressure transducers associated the radial and ovalization modes of the tube oscillation. By contrast, the signals on the intrados, Fig. 34a, are free of these artifacts. Taking this difference into consideration, we see that the ideal TZ model pressures pass through or are slightly above the mean value of the measured pressures with the exception of the first 50 μs. In the first portion of the signal, leading shock waves and expansions associated with the wave reflection from the bend can be clearly observed.

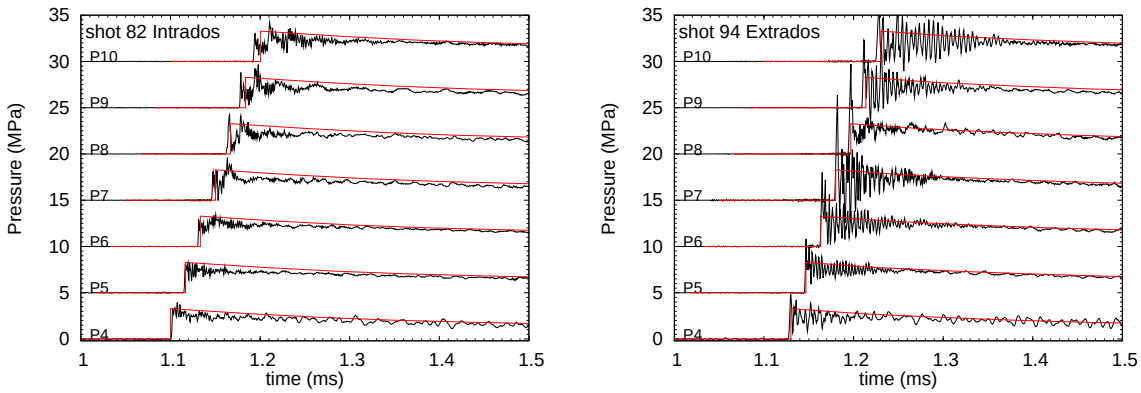

(a) (b)

Figure 34: Pressures histories within the bend compared to TZ model computed for CJ wave speed on the bend centerline. a) Shot 82. b) Shot 94.

On the intrados, a pair of leading shocks separated by 20-30 μs can be observed in traces P7-P10 of Fig. 34a. The second wave front corresponds to the reflected wave created by the Mach reflection on the extrados, as discussed in Edwards et al. (1983), Henshaw et al. (1986) for shocks and Williams and Thomas (2002), Deiterding (2006) for detonations. The Mach reflection on extrados first appears on gage P6 in Fig. 34b as a high pressure leading spike and can be observed to grow in amplitude on gages P7 and P8, then decreasing slightly on gages P9 and P10.

After about 100 μs, the measured and ideal pressure signals are in close (within 10%) agreement. This indicates that the ideal TZ model is a good starting point for estimating the pressure inside the bend just after the wave front has passed through. Further considerations about the initial portion of the signal and accounting for the asymmetry indicated by Fig. 33 are needed if some variant of the TZ model is used to estimate net force due to detonation propagation in a bend. Actual force measurements or structural response measurements that can be used to infer forces are required in order to pursue this further.

6 Tee specimens

The tee specimens were constructed of the same stock of steel tubing as used for the bends. The tees were formed by cutting a hole in the center of a 24-in length of tubing and welding a 12-in. section at a 90 degree angle. Two specimens were fabricated. Specimen No. 1 was instrumented only with strain gages and had no penetrations for pressure gages. Specimen No. 2 had penetrations for pressure gages but no strain gages.

As in the previous tests with straight and bend specimens, the detonation was initiated in the thick-wall aluminum tube and propagated approximately 1.6 m before entering the specimen tube along the axis of the long (24-in) section of the specimen. The specimen was attached to the detonation tube using the same slip-on flange with an o-ring seal as used in previous tests.

In test series 1-4 and 7, the specimens were closed with two end caps containing a pressure transducer and gas recirculation fitting. One cap was located at the end of the 24-in. section and anchored to the main fixture I-beam, see Fig. 35. The other cap was at the end of the 12-in. section and fastened to the vertical support beam. The end caps were slip fits inside the tubes and sealed with o-rings. Caps with plastic diaphragms were used in series 5 and 6.

Seven series of tests (see Table 14) were performed in the two tee specimens. In series 1-3, the specimen was supported only at the three ends and strain gage locations were varied between test series. In series 4, two collets were used to constrain the motion on both the horizontal and vertical legs of the tee. In series 5 and 6, the detonation was allowed to vent through plastic diaphragms to examine the effect of eliminating the reflected waves from the two closed ends of the tee. In series 7, pressure gages were used at selected locations.

Table 14: Summary of test series. "PT" represents the pressure transducer and "SG" represents the strain gage.

Series	Specimen	Setup	shots	Instrumentation
T-1	1	Fig. 36	40-52	15 SG (hoop) on the Tees and 3 PT
T-2	1	Fig. 43	53-56	4 SG (longitudinal) on the Tees and 3 PT
T-3	1	Fig. 45	60-61	15 SG (hoop) on the Tees and 3 PT
T-4	1	Fig. 47	62-63	14 SG (hoop) and 3 PT with two collets
T-5	1	Fig. 49	77-80	14 SG (hoop) and 3 PT with venting
T-6	1	Fig. 45	109-111	14 SG (hoop) and 3 PT with venting
T-7	2	Fig. 52	65-76	12 PT

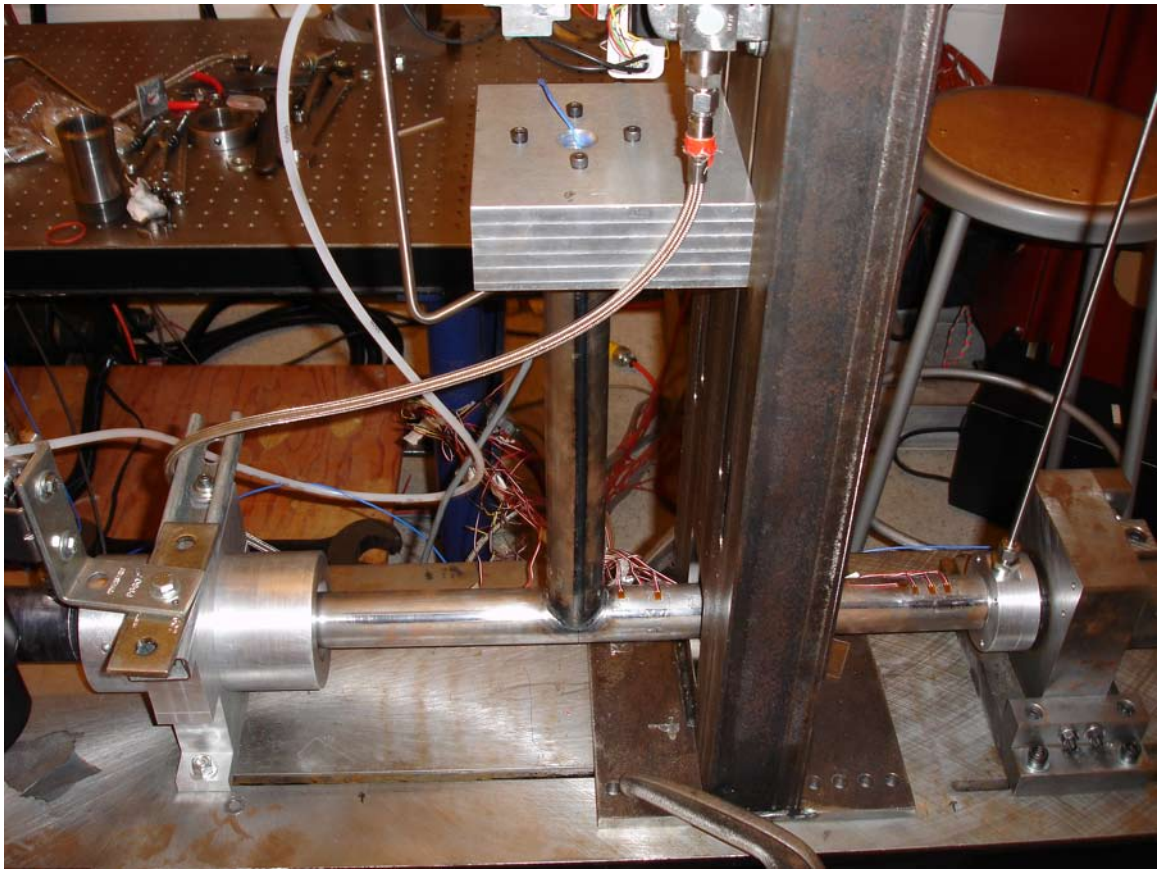

Figure 35: Photograph of tee specimen No. 1 mounted on fixture with closed end caps used in test series T-1 through T-3.

6.1 Test series T-1

In test series T-1, 15 strain gages (see Fig. 36) were mounted on the tube and all were oriented in the circumferential direction to measure hoop strain. Nine gages (S1-S9) were placed close to the tee intersection and three (S10-S12) near the closed end of the 12-in section and three (S13-S15) near the closed end of the 24-in section. These gages and additional ones used in subsequent tests are shown mounted in the photographs of Figs. 37 and 38. Four pressure transducers were used, two (P1 and P2) on the detonation tube to determine the incident wave speed and two (P3 and P4) on the end caps.

The key feature of wave propagation in the tee specimens is the split in the wave propagation path at the tee intersection. The detonation will diffract (turn) into the vertical leg when it reaches the intersection and also continue along the horizontal leg. After the wave divides at the intersection, the resulting waves propagate to the closed ends and reflect at approximately the same time if the turning process does not appreciably affect the detonation propagation. The nature of the turning process will depend strongly on detonation cell

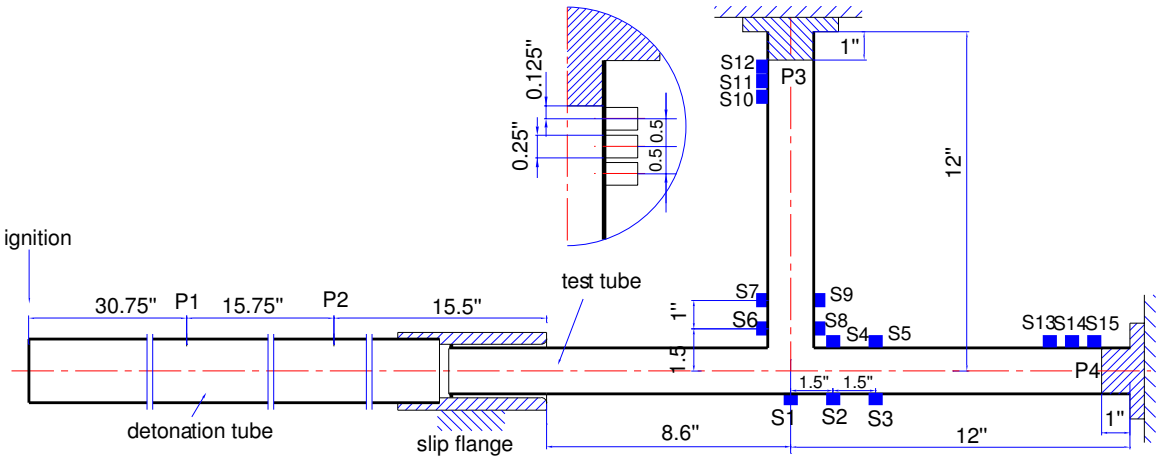

Figure 36: Hoop strain measurement locations for test series T-1.

size compared to the diameter of the tube (Lee, 2008, Pintgen, 2004, Arienti and Shepherd, 2005, Schultz, 2000, Shepherd et al., 2000). The cell size has a strong dependence on mixture type and initial pressure. In the present experiments, only the initial pressure was varied and based on the data in Fig. 8, we expect that the detonation will be able to readily turn the corner into the branch segment as long as the initial pressure is greater than 20 kPa. At this pressure, the cell width is approximately 2-3 mm, which is the critical size for limit of detonation diffraction without failure in our mixture and a diffraction aperture of 40 mm.

At sufficiently low initial pressures, previous work on detonation diffraction through circular openings (Schultz, 2000) and branched tubes (Wang et al., 2008) shows that some portion of detonation will initially fail when diffracting into the branch of the tee. A complex unsteady flow, which has some features similar to nonreactive shock diffraction (Igra et al., 1998, 2001) will result with a Mach reflection (Akbar, 1997, Shepherd et al., 2000) occurring on the outer surface of the branch tube. The reflected wave will propagate back into the failing detonation front and may cause re-initiation of the detonation process. In the present experiments, the detonation appears to be re-initiated within the branched segment close to the intersection in all cases.

The reflection of the detonation waves from the end caps can be observed on the traces obtained from the transducers P3 and P4 in Fig. 39. As in the previous tests, shock waves travel backward into the detonation products when the detonations reach the end caps. The reflected shock waves return to the tee intersection at approximately the same time since the vertical and horizontal legs are approximately the same length. This coincidence of the reflected waves at the tee intersection creates a high pressure region near this location. This transient high-pressure region excites a strong bending oscillation of the horizontal (24-in) section of the specimen with a corresponding up-and-down oscillation of the vertical section.

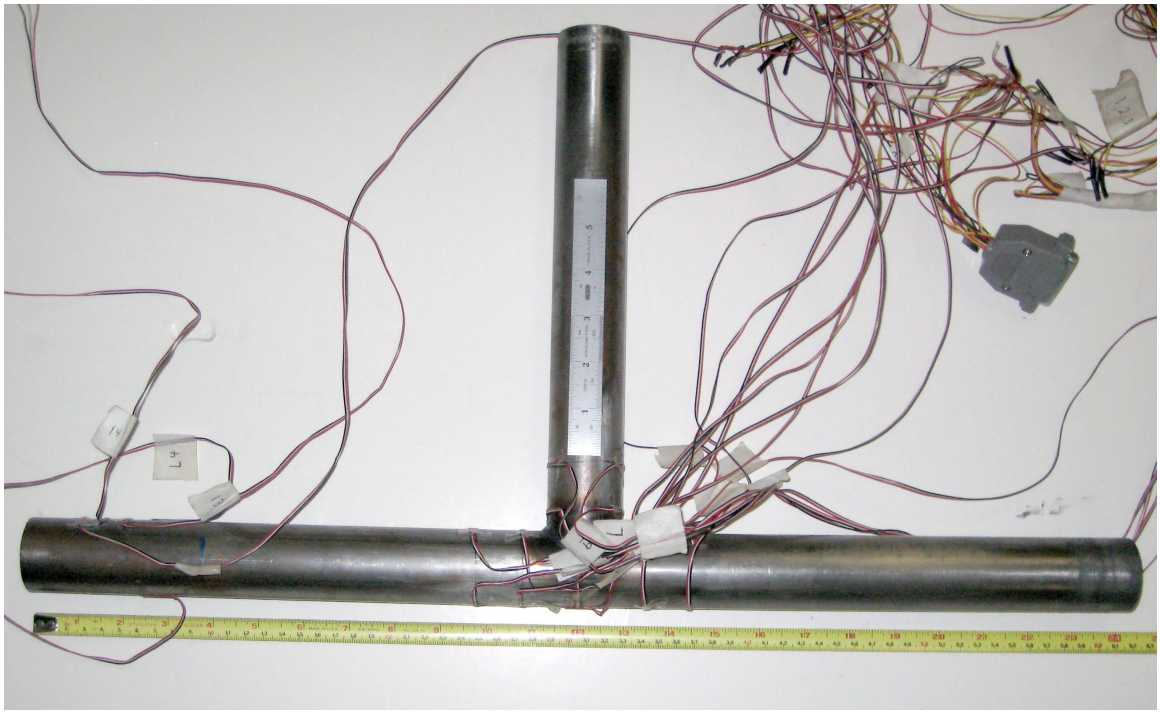

Figure 37: Strain gages mounted on tee specimen No. 1.

The peak in the pressure traces P3 and P4 corresponding to detonation reflection occurs well before the peaks in the strain signals observed in Fig. 40 and Fig. 41.

The strain signals in Fig. 40 and 41 show the characteristic high-frequency (40 kHz) hoop oscillations immediately after the detonation passes by the gage location followed by a much lower frequency (250 Hz) oscillation that damps out after about 20-30 ms. The lower frequency oscillation is identified with the bending mode (see the analysis in the next section) of the long portion of the tee specimen. The peak strain of the bending mode occurs well after the hoop mode was first excited (Fig. 40 and Fig. 41). However, the hoop oscillations persist for 3-4 ms following the passage of the detonation wave and are superposed on the bending oscillations during that time. As a consequence of the amplitude of the bending mode and the superposition of hoop and bending strains, the maximum strain observed in the tee specimens is approximately 1080 μstrain, roughly double the magnitude seen in the straight or bend specimens.

A series of tests with lower initial pressures were also performed. These tests are summarized in Table 26 in Appendix E. Similar features in the strain signals are obtained at all pressures although the bending mode is less prominent at lower pressures.

The peak strains are compared in Fig. 42 and Table 15 at five locations: intersection (S1), straight or horizontal section end (S13-S15), branched or vertical section end (S10-S12), straight section close to the intersection (S2-S5) and branched section close to the

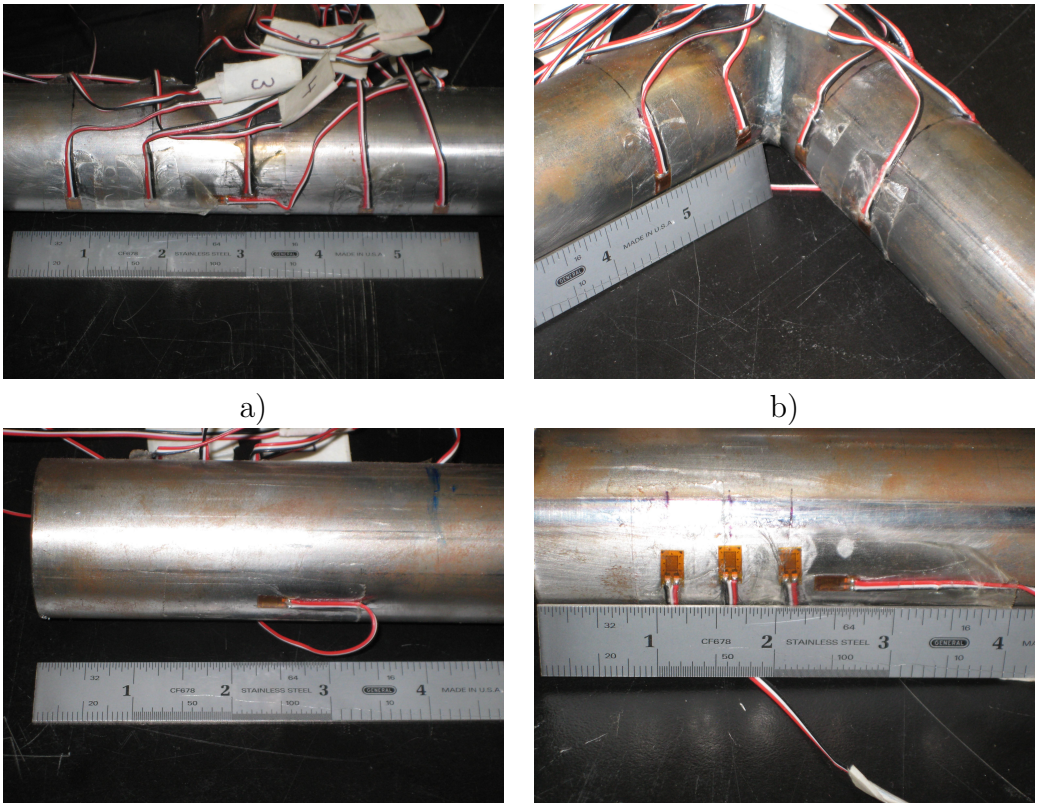

Figure 38: Details of strain gage placement on tee specimen No. 1.

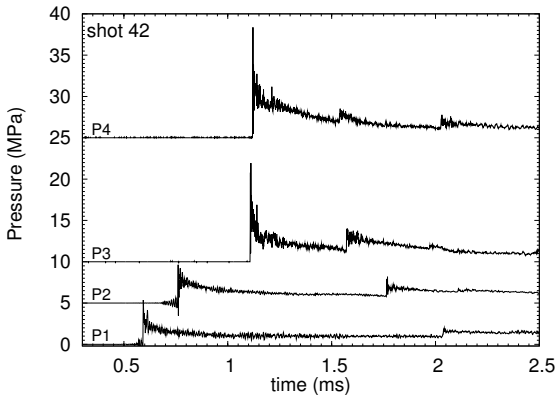

Figure 39: Pressure traces, shot 42 for the tee specimen, test series T-1.

intersection (S6-S9). For $P_0 = 1$ bar, the largest strain, ~ 1100 μstrain, was obtained on S13-S15 at the end of the straight section due to the the effect of the strong reflecting shock waves as well as the structural bending. The lowest peak strain occurs on the vertical branch close to the intersection, ~ 350 μstrain. The strain on the vertical branch is primarily due to the hoop oscillation initiated by detonation loading. As shown in Fig. 42, the peak strains

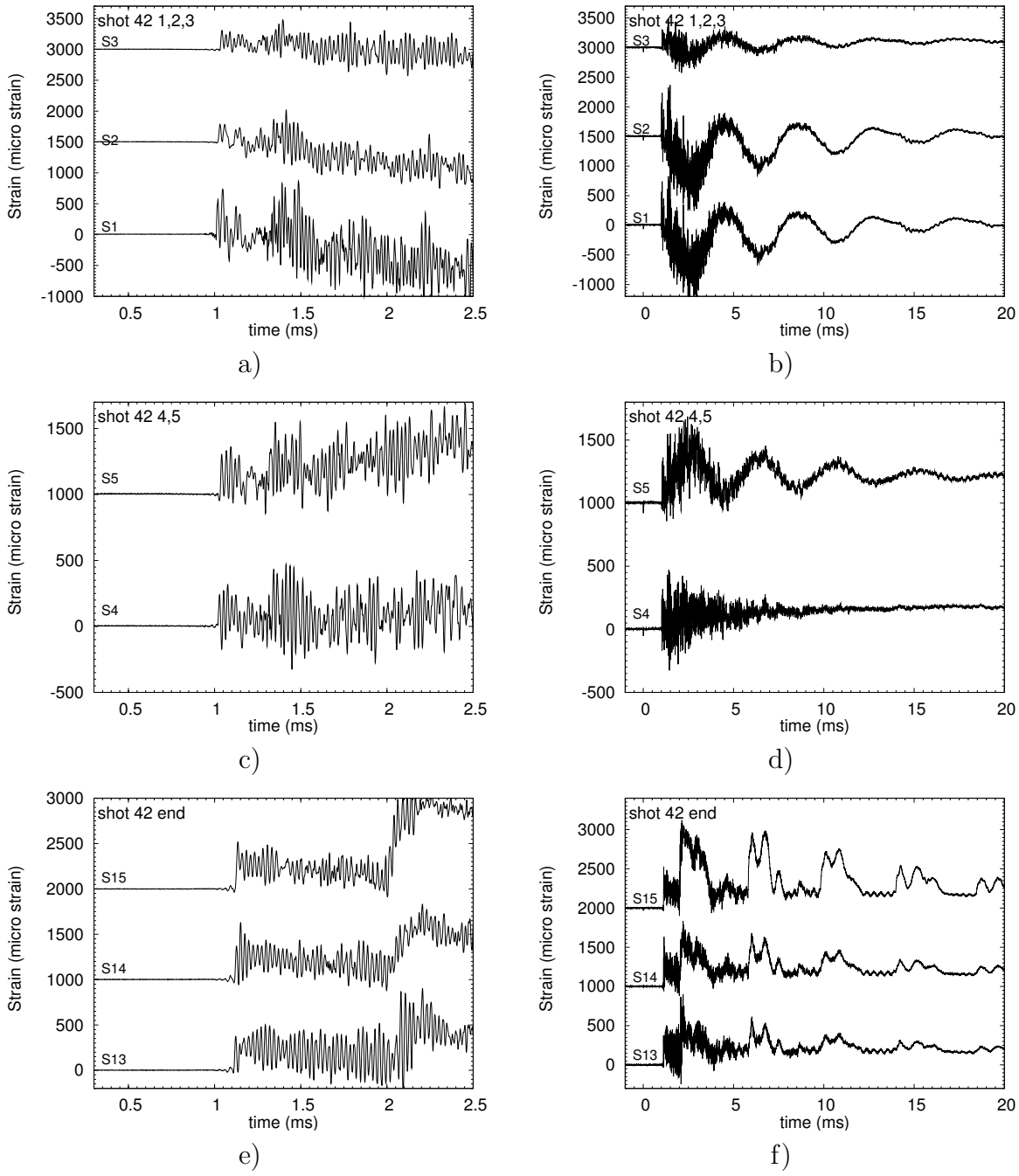

Figure 40: Strain traces of shot 42 for the tee specimen gages a) and b) S1-S3, c) and d) S4-S5, e) and f) S13-S15. Note that the times scale for the right-hand column is 20 ms and for the left-hand column is 2.5 ms. Test series T-1.

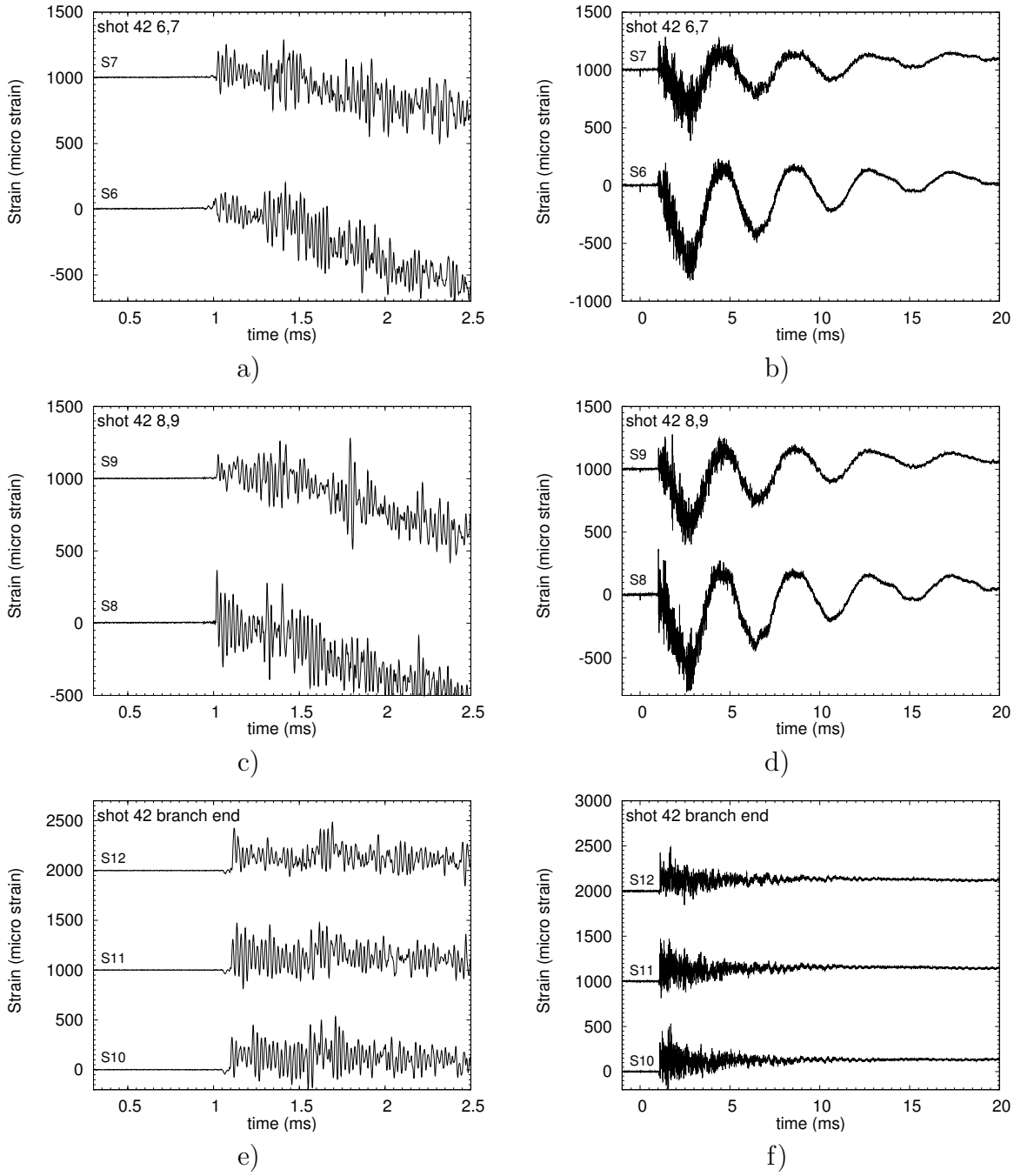

Figure 41: Strain traces of shot 42 for the tee specimen. a) and b) S6-S7, c) and d) S8-S9, e) and f) S13-S15. Note that the times scale for the right-hand column is 20 ms and for the left-hand column is 2.5 ms. Test series T-1.

are bounded from above using the reflected detonation pressure and $\Phi = 2$ in (1), and from below by using the CJ pressure and $\Phi = 2$ in (1). The peak strains are about 60% higher for the tees than the bends (compare with Fig. 25).

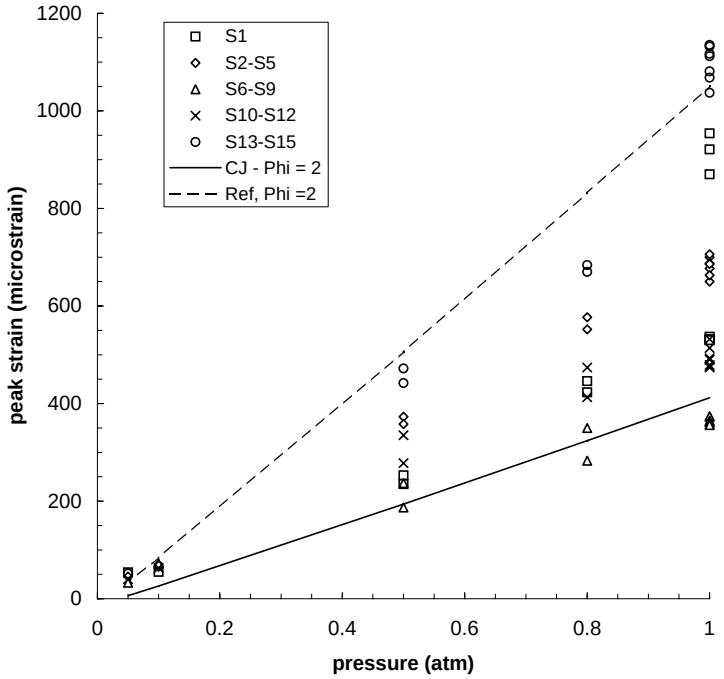

Figure 42: Peak hoop strain of the tee specimen at different initial pressures. Test series T-1.

Table 15: Peak hoop strain for the tee specimen using the setup of Fig. 36. Test series T-1.

shot	P_0	S1$_{max}$	(S2-S5)$_{max}$	(S6-S9)$_{max}$	(S10-S12)$_{max}$	(S13-S15)$_{max}$
	(bar)	(μstrain)				
40	1	921	650	373	514	1135
41	1	954	700	374	493	1132
42	1	870	687	365	532	1117
43	1	530	706	363	490	1068
44	1	537	677	358	476	1112
45	1	532	663	362	479	1081
46	1	530	686	356	474	1037
47	0.8	446	552	350	413	670
48	0.8	423	577	283	474	684
49	0.5	253	373	237	335	472
50	0.5	235	358	187	278	442
51	0.1	55	65.6	72	63	66.8
52	0.05	54	45.4	32.9	40	51.7

6.2 Test series T-2

This series of tests was designed to obtain more information on the large-amplitude, low-frequency oscillations observed in test series T-1. In order to confirm the conjecture that the low-frequency oscillations were associated with a beam bending mode of the horizontal leg of the specimen, longitudinal strain gages were added close to the location of S1, see Fig. 43.

As shown in Fig. 44, the longitudinal sinusoidal oscillation is observed at SL2 before it appears on the gages at the end of the tube. The peak longitudinal strain at the center of the specimen is about 20 times higher than at the ends. The timing and the increase in the magnitude of the strain between 1.4 - 2.5 ms indicate that the specimen is bending and stretching the material under SL2. As this occurs, a deformation of the cross section of the pipe is inevitable at the location of the circumferential end gages, leading to the increase in the strain registered on the hoop gages S13 - S15 in Fig. 40. The highest strains recorded so far (2000 μstrain) were observed on the longitudinal strain gage placed near the intersection (SL2). This gage shows a damped sinusoidal oscillation (Fig. 44) consistent with bending mode vibrations of the horizontal portion of the specimen.

Figure 40b and d show that the strain oscillations on gages S3 and S5 are out of phase by 180 degrees. These gages are located on opposite sides (top and bottom) of the horizontal segment of the specimen, which indicates that the horizontal tube bending motion is in the plane of the specimen. Figure 41b and d show that S6- S9 are oscillating in phase, suggesting that the vertical section is executing bending oscillations in the plane perpendicular to the plane of the specimen.

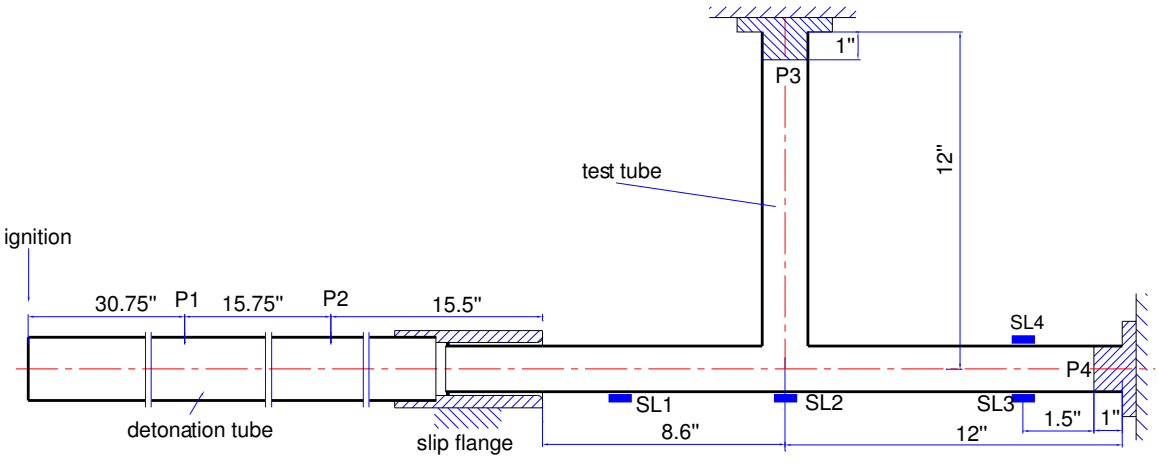

Figure 43: Longitudinal strain measurement locations for test series T-2.

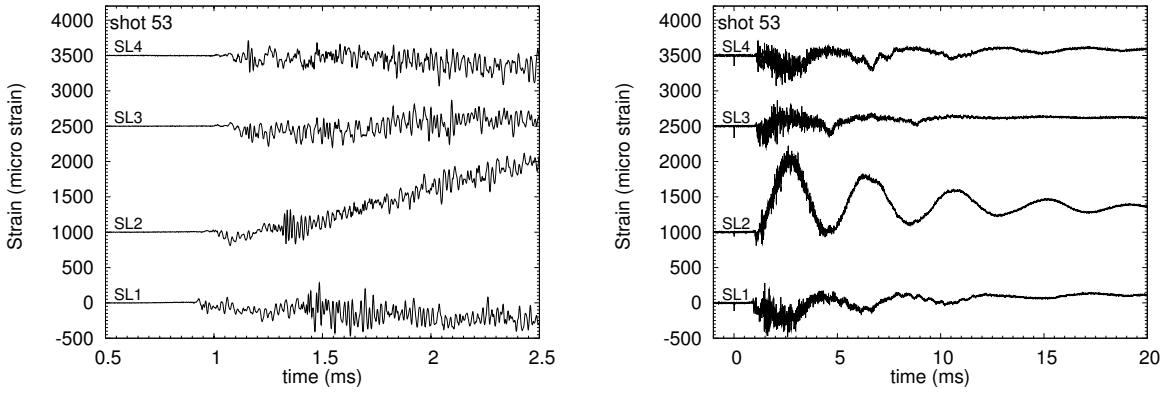

Figure 44: Longitudinal strain histories for gages SL1-SL4 in shot 53 for the tee specimen. Test series T-2.

Table 16: Peak longitudinal strain for the tee specimen using the setup of Fig. 43. Test series T-2.

shot	P_0	SL1	SL2	SL3	SL4
	(bar)	(μstrain)			
53	1	282	1216	366	209
54	1	320	1177	394	219
55	0.8	167	933	260	191
56	0.5	105	489	188	130

6.3 Test series T-3

In order to gain additional understanding of the specimen oscillation modes, test series T-3 included another four gages S2*-S5* to measure hoop strain. These were placed on the top and bottom of the horizontal section at locations symmetric to the axis of the vertical tube and the gages S2-S5 (see Fig. 45). Four (S11-S14) of the original gages were disconnected since a limited number of signal conditioners and data acquisition channels were available.

Figure 46 shows the long-time strain histories for S1-S9. The phase and the amplitudes of the strain oscillations for gages S4 and S5 and and S6 and S7 are different from those observed in shot 42. Between these two shots, the test setup had been disassembled and then re-assembled. This shows that the details of tube oscillation mode and the strain signal are strongly dependent on the placement and alignment of the fixturing.

In Figures 46, the strains from gages S1-S3 are oscillating in phase with those from S2* and S3*, indicating that the horizontal sections to the left and right of the tee intersection oscillate symmetrically. However the signal on gage S5* is 180 degrees out of phase from S3*, and S4 has the same phase as S2. This is different from the motion observed in shot 42

and indicates that the top portion of the horizontal tube may be twisting due the movement of the vertical section, creating an asymmetry in the motion of the horizontal section. The signals on gages S6-S9 are similar to those of shot 42, indicating that the vertical section oscillates in a plane perpendicular to the specimen.

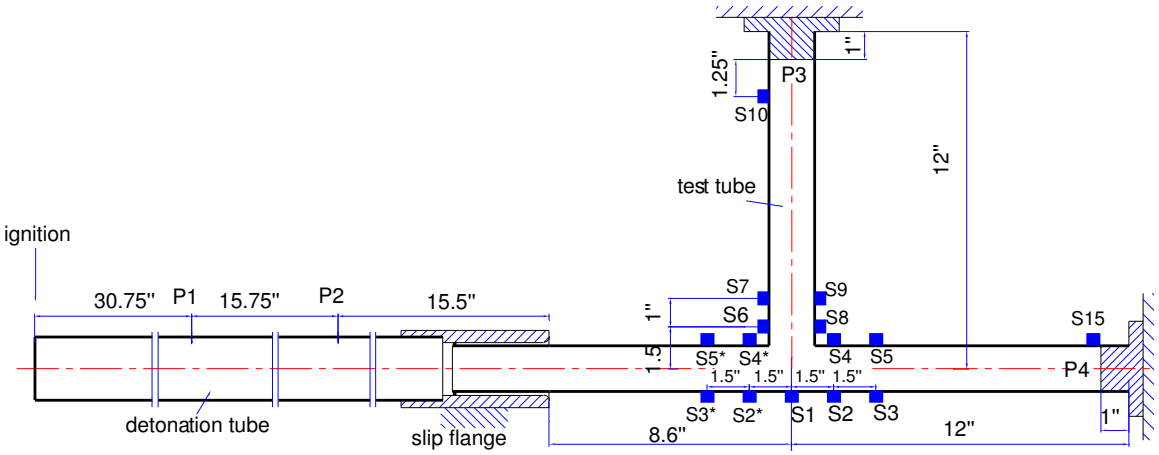

Figure 45: Hoop strain measurement locations for test series T-3.

6.4 Test series T-4

Two additional extra collets were used to clamp the specimen to the support structure in test series T-4. The location of the collets is shown in Fig. 47. The maximum strain occurs close to the reflecting end and is on the order of 500-600 μstrain. This similar to what was observed for the straight specimens, see Section 4. The strain signals in Fig. 48 clearly show that the low frequency oscillation is eliminated when the specimen is restrained by the additional collets. This provides further confirmation of the bending mode origin of the low-frequency oscillation.

6.5 Test series T-5 and T-6

As discussed previously, the equal length of the vertical and horizontal tube segments downstream of the tee intersection creates a special situation for the reflected shock waves. The collision of the reflected shock waves near the tee intersection was conjectured to play a significant role in exciting the bending mode of the horizontal tube segment. To test this conjecture, the reflected waves were eliminated and the strains measured without the additional restraining collets using in test series T4.

Two modifications were used to eliminate or reduce the reflected waves from the end caps. In test series T-5, a hollow slip-on flange (see Fig. 49) with a thin plastic diaphragm was

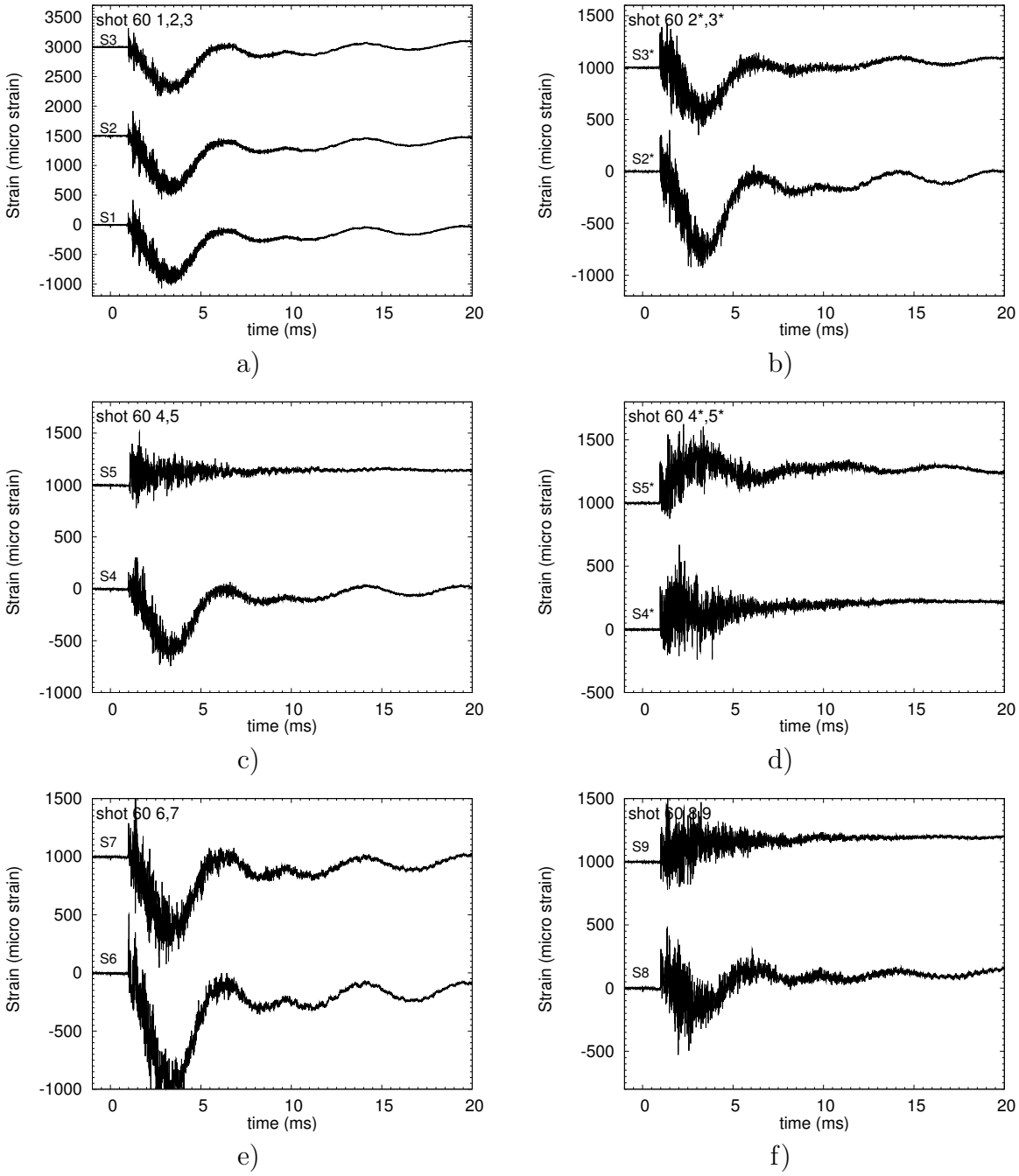

Figure 46: Strain traces of shot 60 for the tee specimen. Test series T-3.

used to seal the vertical segment. The plastic was very thin and ruptured when impacted by the detonation wave. This essentially eliminates the reflected wave on the vertical portion but the change in fixturing unfortunately created a very strong constraint on the motion of the specimen. This can be observed in the comparison shown in Figs. 50 of shot 80 with the diaphragm replaced by a rigid metal plate and shot 78 with a rupturing plastic diaphragm.

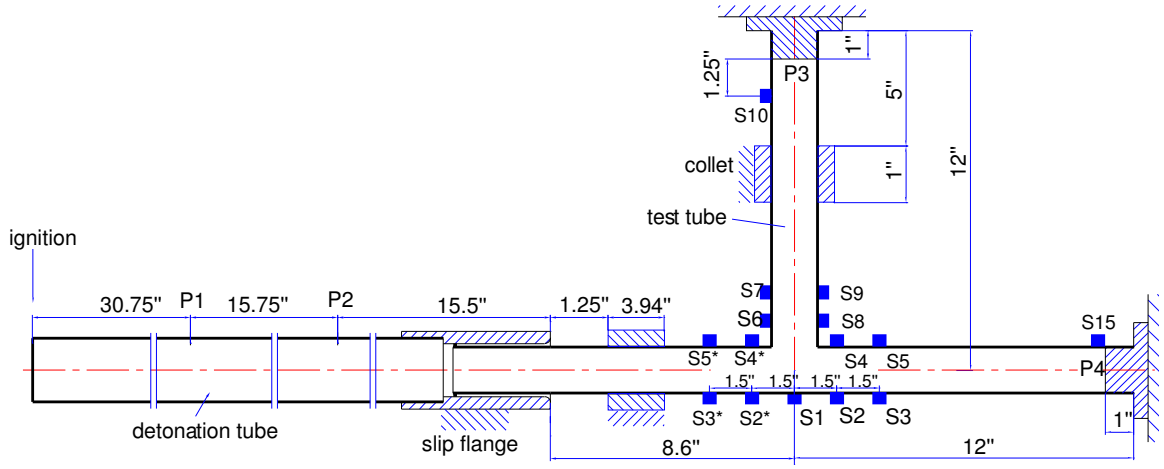

Figure 47: Hoop strain measurement and collet locations for test series T-4.

In both cases, there is a very minimal structural oscillation observed and the peak strain ($\sim$ 500 μstrain) can be accounted for by the radial motion excited by the usual detonation loading in straight tube segments.

To eliminate the constraint of the slip-on collet, test series 6 was carried out with two hollow end caps that slipped inside the tube and were sealed with either a plastic diaphragm or a rigid metal plate. These caps did not restrain the motion of the tube and the mechanical system was essentially identical to that used in test series 1, shown in Fig. 36.

The strain signals are shown in Fig. 51 for three cases. In shot 109, a rupturing diaphragm was located on the vertical segment end and the horizontal segment end had a rigid closure. In shot 110, a rupturing diaphragm was located on the horizontal segment end and the vertical segment end had a rigid closure. In shot 112, both ends used a rupturing diaphragm. It is interesting to notice that the bending mode appeared in all of the three cases with very similar magnitudes. However, the peak magnitude is much smaller than when both ends are closed as in Fig. 40. The pressure traces in Fig. 51e still show evidence of a small pressure wave reflected back into the main detonation tube. This is due to the inner diameter of two hollow end plugs being 0.1 in smaller than the tube ID.

The results of test series T-6 show that wave interactions and the symmetry of the tee segments are not essential for significantly exciting the bending mode of the tube. Both the incident wave and reflected waves contribute to the structural bending mode and the magnitude of the oscillation. The method of mounting the specimen and the amount of constraint on the end motion appears to be more important in determining the amplitude of the structural oscillation than the collision of the reflected shock waves.

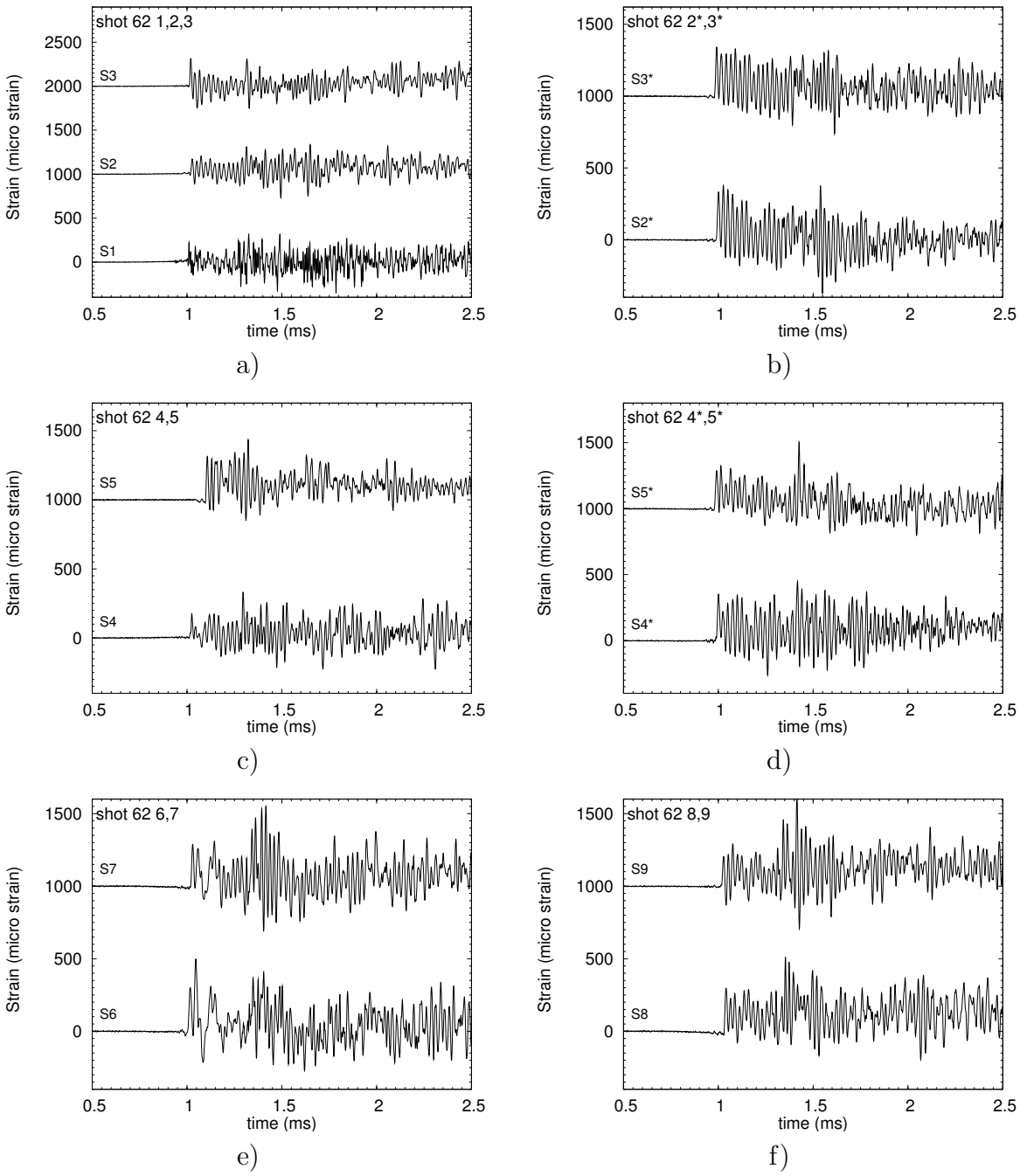

Figure 48: Strain traces for shot 62 in series T-4.

6.6 Test series T-7

In Test series T-7, the pressure signals were recorded at the selected locations using the specimen No. 2 with welded pressure transducer adaptors (see Fig. 52 and 53). A total of 12 tests were performed with various initial pressures. For higher initial pressure ($P_0 > 0.5$ bar), as shown in Figs. 54a-c, the detonation wave was initiated before entering the test

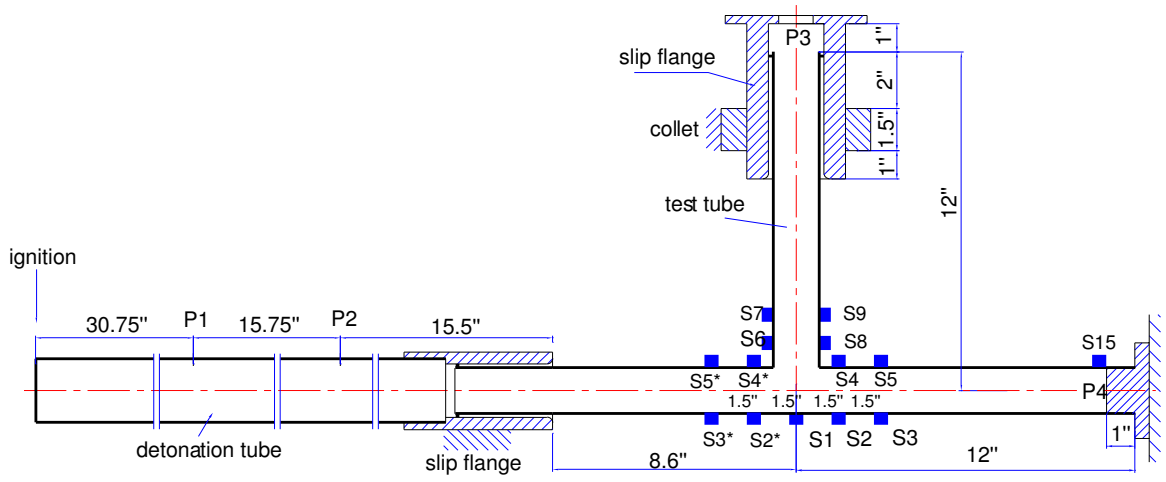

Figure 49: Hoop strain measurement locations and diaphragm mounting collet used in test series T-5.

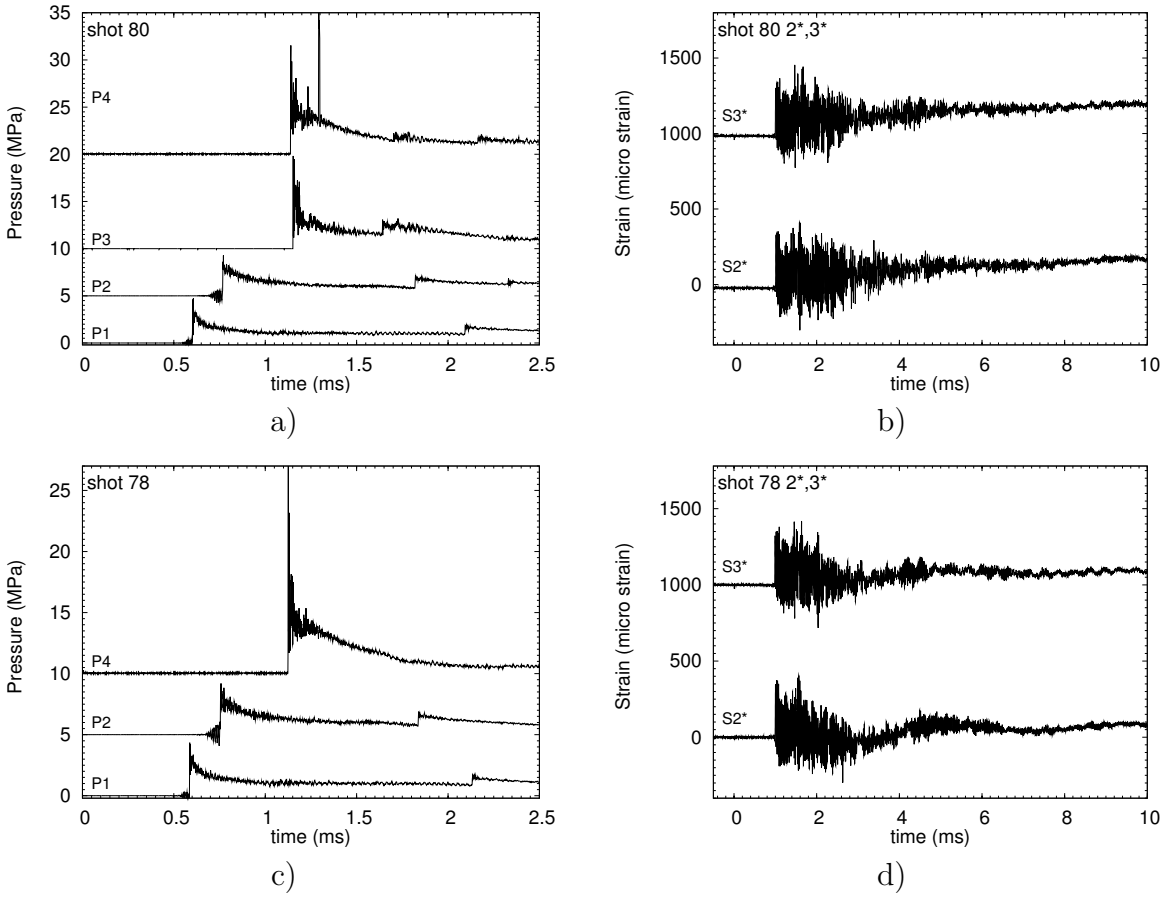

Figure 50: Pressure and strain traces of (a) and (b) shot 80 with both ends closed, (c) and (d) shot 78 with the vertical end open. Test series T-5.

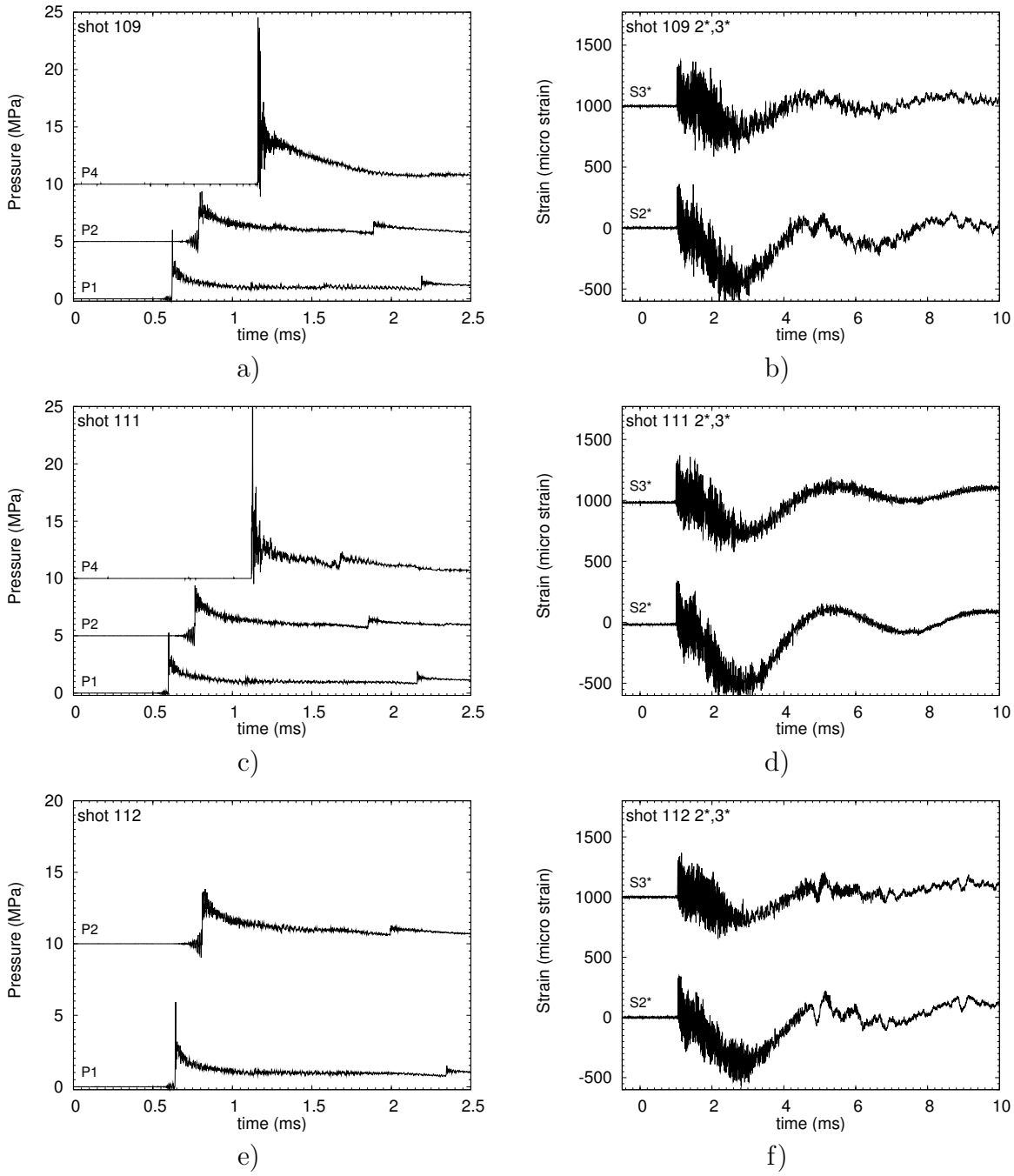

Figure 51: Strain traces of (a) shot 109 with an open end on the vertical segment (b) shot 111 with an open end on the horizontal segment, (c) shot 112 with both ends open. Test series T-6.

section, diffracted into the 90-degree branch and continued on into the straight branch. The peak pressures at both reflecting ends show the same magnitudes. For the lower P_0 cases, as shown in Fig. 54e, DDT occurred within the tee specimen close to the intersection of the tee.

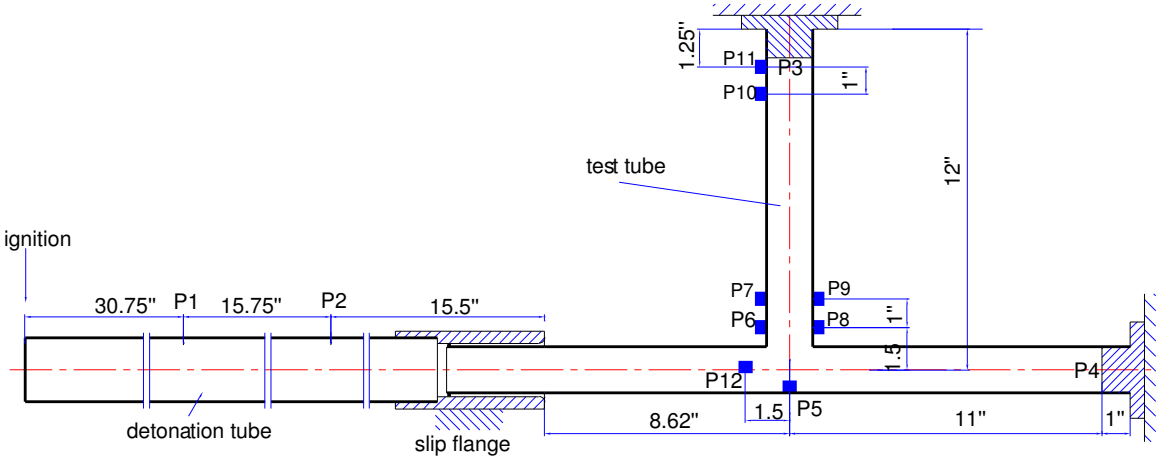

Figure 52: Pressure measurement locations for tee specimen No. 2 used in test series T-7.

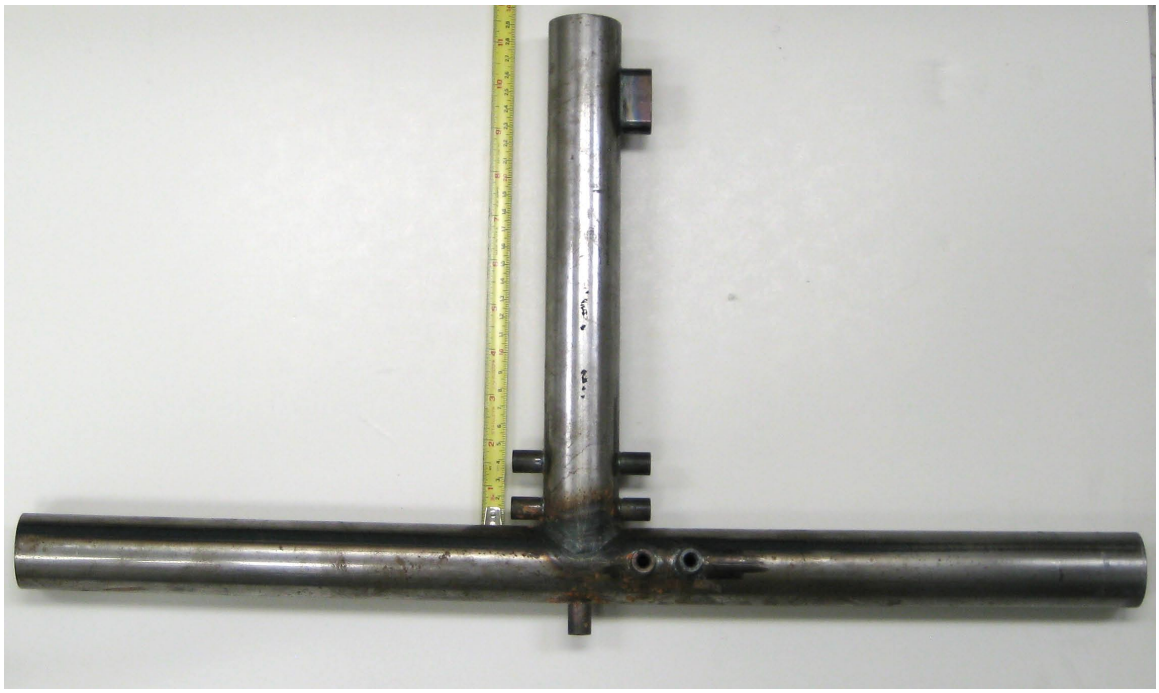

Figure 53: Photograph of tee specimen No. 2 used in test series T-7.

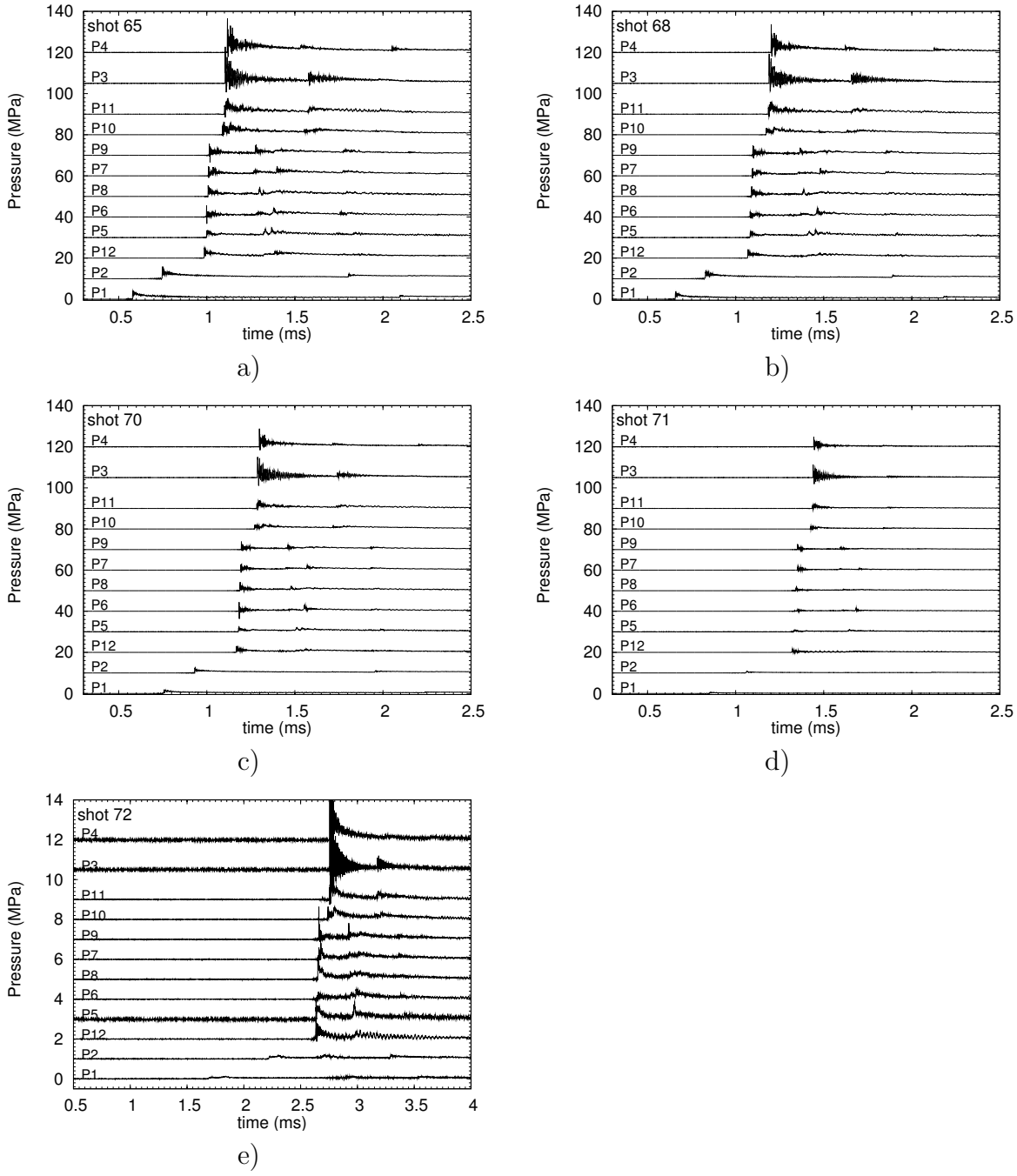

Figure 54: Pressure traces for the tee specimen. a) P_0=1 bar (shot 65); b) P_0=0.8 bar (shot 68); c) P_0=0.5 bar (shot 65), d) P_0=0.2 bar (shot 68) and e) P_0=0.1 bar (shot 72). Test series T-7.

7 Tee Structural Response Model

We have developed a simple model to explain the main features of the structural oscillations of the Tee specimens. The tee specimens are modeled as a uniform horizontal beam with both ends simply supported. The vertical portion of the tee is represented by a central mass W and the two horizontal sections by a uniform mass per length w. The approximate natural

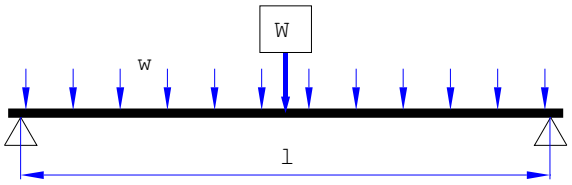

Figure 55: Mathematical model 1 of the tee specimen.

frequency is given by (Young and Budynas, 1989, pp.765, case 1c),

$$f = \frac{6.93}{2\pi l^2}\sqrt{\frac{EI}{W/l + 0.486w}} \tag{11}$$

where $E = 210$ GPa, $l = 0.609$ m, $W = 0.455$ kg, and $w = 1.492$ kg/m. We have used the entire horizontal length (24 in) of the specimen in this formula since we are considering shots of the type in test series T1 for which no additional collets were used and specimen was not held firmly at the ends. I is the area moment of inertia considering the horizontal leg of the pipe as a beam, which for a circular tube is

$$I = \frac{\pi}{4}({r_2}^4 - {r_1}^4) = \frac{\pi}{4}({r_2}^2 + {r_1}^2)(r_2 + r_1)(r_2 - r_1) \tag{12}$$

where r_2 is the outer radius and r_1 is the inner radius of the tube. Substituting h $(r_2 - r_1)$ and R ($r_2 - h/2$ or $r_1 + h/2$) into (12) gives

$$I = \frac{\pi}{2}(2R^2 + \frac{1}{2}h^2)Rh \approx \pi R^3 h \tag{13}$$

with $R = 19.88$ mm and h =1.524 mm, $I = 3.76$ mm^4.

Substituting these values into (11) gives

$$T = 4.5 \text{ ms}; \quad f = 217 \text{ Hz}\ , \tag{14}$$

which is about 6% lower than the observed oscillation frequency of 232 Hz obtained from

the power spectra of Fig. 40.

7.1 Estimation of structural deflection

The structure of the tee specimen can be modeled as a single-degree-of-freedom classical spring-mass system, see Fig. 56. If we neglect damping (which is actually quite substantial in this case), the displacement y as a function of time t is given by the solution to the forced simple harmonic oscillator

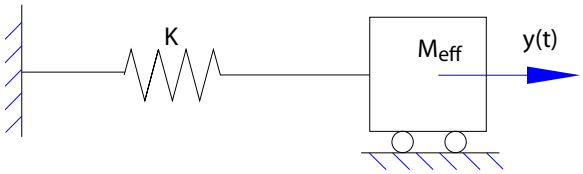

Figure 56: Mathematical model 2 of the tee specimen.

$$\frac{d^2y}{dt^2} + \omega^2 y = \frac{F(t)}{M_{eff}} \tag{15}$$

where M_{eff} is the effective mass

$$M_{eff} = W + 0.486wl \ , \tag{16}$$

$$= 0.897 \quad \text{kg} \ , \tag{17}$$

and K is the effective stiffness which can be computed from the frequency

$$K = \omega^2 M_{eff} \ . \tag{18}$$

The frequency $\omega = 2\pi f$ and f is given by (11), and in the present case

$$\omega = 1396.3 \text{ rad/s} \ . \tag{19}$$

As discussed on p. 64 of Paz (1985), an arbitrary loading history $F(t)$ can be regarded as a series of short impulses at successive incremental times ($d\tau$), each producing its own differential response at time t. The total displacement at time t due to the continuous action of the force $F(\tau)$ is given by the summation (integration) of the individual differential displacements. This approach to computing the response is known as *Duhamel's integral*

and yields the total displacement $y(t)$ at time t by carrying out the following integration

$$y(t) = \frac{1}{M_{eff}\omega} \int_0^t F(\tau) \sin(\omega(t-\tau)) d\tau \ . \tag{20}$$

For a first estimate, the force was approximated as $F = PA$, where the pressure $P(\tau)$ was measured at the base of tee, and A was approximated as the cross section area of the tube, $\pi r_1^2 = 0.00126$ m^2.

Using the experimental pressure trace and numerically integrating (20), the deflection $y(t)$ was obtained. The maximum displacement of the center portion of the beam $y = 2.1$ mm. In order to find the strain near the center, we use the beam strain relationship

$$\epsilon_l = \frac{c}{R_y} \tag{21}$$

where $c = r_2$ is the distance from the neutral axis (centerline of tube) to the outer edge of the beam and R_y is the radius of curvature of the deflected beam at the center. We can use the Pythagorean Theorem to the compute the radius of curvature R_y from beam deflection y

$$R_y = \frac{l^2}{8y} + \frac{y}{2} \ ; \tag{22}$$

and for the maximum deflection predicted by the SDOF model

$$R_y = 21.8 \text{ m} \ . \tag{23}$$

The longitudinal strain ϵ_{long} then equals

$$\epsilon_{long} = \frac{c}{R_y} \ ; \tag{24}$$

and the maximum longitudinal strain is predicted to be

$$\epsilon_{long} = 913 \ \mu\text{strain} \ , \tag{25}$$

and the corresponding maximum hoop strain is

$$\epsilon_{hoop} = -\nu\epsilon_{long} \ ; \tag{26}$$

which has a maximum value of

$$\epsilon_{hoop} = -266 \ \mu\text{strain} \ . \tag{27}$$

The estimated longitudinal strain in the middle of the tube is compared to the measured strain on gage SL2 in Fig. 7.1. As shown, the measured peak longitudinal strain (gage SL2 in Shot 53, Fig. 44) is about 1200 μstrain. The peak estimated strain is slightly lower (918 μstrain) and the period of the simple model is obviously too long in comparison with the actual value, indicating that the effective mass and stiffness are slightly different than the idealized simply-supported beam model.

The measured hoop strain (gage S1 in Shot 42, Fig. 40) shows a significant contribution of the high-frequency (42 kHz) hoop oscillations which must be filtered out to obtain the contribution of the beam bending mode alone. Using a 10 kHz low pass filter, we find that the contribution of the beam bending portion is on the order of -600 μstrain. Without filtering the peak hoop strain is on the order of -950 μstrain.

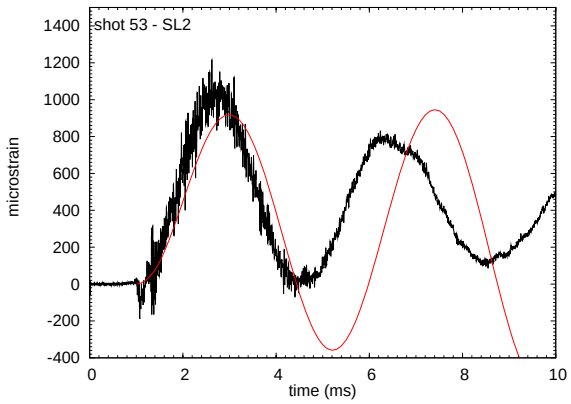

Figure 57: Strain history on gage SL2 (underneath of the Tee intersection) for shot 65 and the corresponding estimated strain using Duhamel's method and the measured pressure load.

8 Summary

The structural response, due to detonation loading of three mild carbon steel piping components: straight section with a closed end, a gradual bend, and a 90-degree branch or tee, was studied with a stoichiometric mixture of ethylene and oxygen at an initial pressure varying between 0.05 and 1 bar.

For the straight sections, the maximum strain observed close to the reflecting closed ends is approximately the static value based on the computed ideal reflected CJ pressure. Due to interference of incident and reflected flexural waves, the maximum strain values occurs at one of the five strain gages placed near the termination end of the specimen. The dynamic load factor is bounded by 1.25 at these locations when the reference pressure is the ideal reflected CJ value. The simple Taylor-Zeldovich model of the flow following the detonation compares reasonably well with the observed pressure time histories and pressure at the reflecting surface can be predicted using a simple exponential decay model.

For the bend specimens, the strain gages at the closing end show very similar strain histories as the end gages on the straight specimens. The average propagation speed of the wave around the bend is close to the CJ value. Collectively, these observations indicate for nearly ideal detonation waves, the effect of the bend is localized and dies out within one to two bend radii downstream of the bend. Across the bend, the average peak strain and peak pressures on the extrados are always larger than those on the intrados for all initial pressures. This is interpreted in terms of the diffraction of the detonation resulting in the generation of compression waves on the extrados and expansion waves on the intrados as the detonation wave front turns to remain normal to the tube surface. The dynamic load factors (based on for both the extrados and intrados are larger than 1 at the beginning of the bends ($<$ 30-deg) and decrease to less than l at the downstream locations. The peak strains measured on the bend specimens are similar to those observed on the straight sections with closed ends. A limitation of the present study on bends is the significant constraints on motion due to the collets used to clamp the ends of the tube to the fixture. These constraints and the short length of the specimens prevent the observation of motions associated with force created by the detonation wave turning as it moves through the bend. Further experiments with different specimens and instrumentation are required to obtain information about bend forces.

For the tee specimens, the peak strain is close to double that observed in either the straight section with a reflecting end or the bend specimens. This is due to the excitation of low-frequency (240 Hz) beam-bending oscillation mode of the long leg of the tee superposed on the short-period (40 kHz) hoop oscillation. The peak strains can be bounded by a

dynamic load factor of 2 using a reference pressure corresponding to that produced by an ideal reflected CJ detonation. For the tee specimen, the beam bending motion can be modeled using a simple single-degree-of-freedom model of structural response. It is possible to suppress the structural mode observed in the tee specimens by placing extra support at key points along the structure. One of the limitations of the tee section is the equal length of the arms of the tee, which results in addition bending mode excitation due to the collision of the shock waves created by the reflected detonation. However, this is not a key factor since tests with venting at the ends of the tee section also exhibit the beam bending mode but with a smaller amplitude than for closed end cases.

The present study provides insight into the detonation behavior and strains for detonations propagating in generic piping system components. Although the magnitude of the strains and the modes of oscillation are specific to our specimens and nearly ideal detonations, we believe that the results have significance to explosion hazard analysis in industrial piping systems. The implications are that structural modes of oscillation may be as significant as high-frequency breathing modes and in some cases, the superposition of the two modes may lead to significantly larger structural response than estimated on the basis on each mode alone. The present study is limited to small specimens and nearly ideal detonation waves. Additional testing is needed to extrapolate to industrial piping systems and a wide range of explosion modes, including deflagration, detonation, and deflagration-to-detonation transition. Future work should examine larger specimens, other mixtures and methods of detonation initiation, direct measurement of forces and displacement of piping components, and more realistic support method for the piping systems.

Acknowledgments

A portion of this work was carried out during the spring and summer of 2006 as a SURF project by Tim Curran who was supported by the Toshi Kubota memorial fund. Zhe (Rita) Liang was Tim's supervisor and she continued the work during the fall of 2006. Rita was partially supported by a Fellowship from NSERC, Canada during her stay at Caltech.

Bibliography

S. D. Ahnert. System response benchmark validation. Calculation Note C-6908-00-26, Dominion Engineering, Inc., August 2006. Issued as Bechtel Supplier Document 24590-QL-HC4-W000-0067. 13, 14

R. Akbar. *Mach Reflection of Gaseous Detonations*. PhD thesis, Rensselaer Polytechnic Institute, Troy, New York, August 1997. 59

Donatello Annaratone. *Pressure Vessel Design*. Springer, 2007. 14

George A. Antaki. *Piping and Pipeline Engineering*. CRC Press, 2003. 14

M. Arienti and J. E. Shepherd. A numerical study of detonation diffraction. *J. Fluid Mech.*, 529:117–146, 2005. 59

ASME. *Power Piping: ASME Code for Pressure Piping, B31*. American Society of Mechanical Engineers, 2001. ANSI standard ASME B31.1-2001. 14

W. E. Baker, P. A. Cox, P. S. Westine, J. J. Kulesz, and R. A. Strehlow. *Explosion Hazards and Evaluation*. Elsevier, 1983. 24

W.M. Beltman and J.E. Shepherd. Linear elastic response of tubes to internal detonation loading. *Journal of Sound and Vibration*, 252(4):617–655, 2002. 13, 15, 16, 25, 26, 28, 31, 34, 39

W.M. Beltman, E.N. Burcsu, J.E. Shepherd, and L. Zuhal. The structural response of cylindrical shells to internal shock loading. *Journal of Pressure Vessel Technology*, 121: 315–322, 1999. 13

J. Biggs. *Introduction to structural dynamics*. McGraw-Hill, Inc., 1964. ISBN 07-005255-7. 24

KW Boyack, SR Tieszen, and DW Stamps. Internal-pressure loads due to gaseous detonations. *Proceedings Of The Royal Society Of London Series A-Mathematical Physical And Engineering Sciences*, 443 (1918):343–366, November 8 1993. 16

S. Browne, J. Ziegler, and J. E. Shepherd. Numerical solution methods for shock and detonation jump conditions. Technical Report FM2006.006, GALCIT, 2004. 33

T. Chao and J.E. Shepherd. Detonation loading of tubes in the modified shear wave regime. In Z. Jiang, editor, *Proceedings of the 24th International Symposium on Shock Waves*, volume 2, pages 865–870. Springer, 2005a. 13

T. W. Chao. *Gaseous detonation-driven fracture of tubes*. PhD thesis, California Institute of Technology, 2004. 13, 19, 25, 38

T. W. Chao and J. E. Shepherd. Comparison of fracture response of preflawed tubes under internal static and detonation loading. *Journal of Pressure Vessel Technology*, 126(3): 345–353, 2004. 13

T.-W. Chao and J. E. Shepherd. Fracture response of externally flawed aluminum cylindrical shells under internal gaseous detonation loading. *International Journal of Fracture*, 134 (1):59–90, July 2005b. 13, 19

T.-W. Chao and JE Shepherd. Fracture response of externally-flawed cylindrical shells to internal gaseous detonation loading. In M. Fisher and A. Holdo, editors, *ASME Pressure Vessels and Piping Conference. Emerging technologies in Fluids, Structures, and Fluid-Structure Interactions, PVP Vol. 462-2*, pages 85–98. ASME, 2002. PVP2002-1491. 19

Ralf Deiterding. Dynamically adaptive simulation of regular detonation structures using the cartesian mesh refinement framework AMROC. *Int. J. Computational Science and Engineering*, 1(1/2/3):64–74, 2006. 56

T.A. Duffey, E.A. Rodriguez, and C. Romero. Design of pressure vessels for high-strain rate loading: dynamic pressure and failure criteria. Bulletin 477, Welding Research Council, P.O. Box 1942, New York, NY, 2002. 15

D. H. Edwards, P. Fearnley, and M. A. Nettleton. Shock diffraction in channels with 90° bends. *J. Fluid Mech.*, 132:257–270, 1983. 49, 56

C. M. Harris and A. G. Piersol, editors. *Harris' Shock and Vibration Handbook*. McGraw-Hill, fifth edition, 2002. 15

John F. Harvey. *Theory and Design of Pressure Vessels*. Van Nostrand Reinhold, second edition, 1991. 14

W. D. Henshaw, N.F. Smyth, and D. W. Schwendeman. Numerical shock propagation using geometrical shock dynamics. *J. Fluid Mech.*, 171:517–545, 1986. 49, 56

O. Igra, L. Wang, J. Falcovitz, and W. Heilig. Shock wave propagation in a branched duct. *Shock Waves*, 8:375–381, 1998. 59

O. Igra, X. Wu, J. Falcovitz, T. Meguro, K. Takayama, and W. Heilig. Experimental and theoretical study of shock wave propagation through double-bend ducts. *J. Fluid Mech.*, 437:255–282, 2001. 59

R. Knystautas, J.H. Lee, and C.M. Guirao. The critical tube diameter for detonation failure in hydrocarbon-air mixtures. *Combust. Flame*, 48(1):63–83, 1982. 27

H. Kolsky. *Stress Waves in Solids*. Dover, 1963. 37

M. Kuznetsov, W. Breitung, J. Grüne, and R. K. Singh. Strutural response of DN15-tubes under radiolysis gas detonation loads for BWR safety applications. In *18th International Conference on Structural Mechanics in Reactor Technology*, number SMiRT 18-J09-1, Beijing, China, August 2005. 13

J. H. S. Lee. *The detonation phenomenon*. Cambridge University Press, 2008. 59

Z. Liang and J.E. Shepherd. Explosion testing of the nested can containment system. part I: Planar gap. part II. thick-walled tube. part III. 3013 outer can. Technical Report FM2007-001, Graduate Aeronautical Laboratory, California Institute of Technology, May 2007. 13, 16

Z. Liang, J. Karnesky, and J.E. Shepherd. Delflagration-to-detonation transition tests in H_2-O_2-N_2-He mixtures. Technical Report FM2006-004, Graduate Aeronautical Laboratory, California Institute of Technology, August 2006a. 13, 16

Z. Liang, J. Karnesky, and J.E. Shepherd. Structural response to reflected detonations and deflagration-to-detonation transition in H_2-N_2O mixtures. Technical Report FM2006-003, Graduate Aeronautical Laboratory, California Institute of Technology, August 2006b. 13, 16, 31

Z. Liang, J. Karnesky, and J.E. Shepherd. Detonations in C_2H_4-O_2. Experimental measurements and validation of numerical simulations for incident and reflected waves. Technical Report FM2006-009, Graduate Aeronautical Laboratory, California Institute of Technology, June 2008. 23, 29, 30, 32, 33, 34

Kenneth G. McConnell. *Vibration Testing: Theory and Practice*. Wiley, 1995. 15

M. Naitoh, F. Kasahara, R. Kubota, and I. Ohshima. Analysis of pipe rupture of steam condensation line at Hamoaka-1, (I) Accumulation of noncondensable gas in a pipe. *Journal of Nuclear Science and Technology*, 40(12):1032, 2003a. 13

M. Naitoh, F. Kasahara, R. Kubota, and I. Ohshima. Analysis of pipe rupture of steam condensation line at Hamoaka-1, (II) Hydrogen combustion and generation. *Journal of Nuclear Science and Technology*, 40(12):1041–1051, 2003b. 13

M. Paz. *Structural Dynamics Theroy and Computation*. Van Nostrand Reinhold Company, 1985. 15, 24, 76

F. Pintgen and J.E. Shepherd. Structural response to deflagration-to-detonation transition events in a tube. Technical Report FM2005-005, Graduate Aeronautical Laboratories California Institute of Technology, August 2005. 13

F. Pintgen and J.E. Shepherd. Elastic and plastic structural response of thin tubes to deflagration-to-detonation transition events. Technical Report FM2005-008, Graduate Aeronautical Laboratories California Institute of Technology, January 2006. 13

Florian Pintgen. *Detonation diffraction in mixtures with various degrees of instability*. PhD thesis, California Institute of Technology, Pasadena, California, December 2004. Electronic version available at http://etd.caltech.edu/etd/available/etd-02072005-173741/. 59

K. R. Rao, editor. *Companion Guide to the ASME Boiler and Pressure Vessel Code*, volume 2. ASME Press, 2002. 15

W.C. Reynolds. The element potential method for chemical equilibrium analysis: implementation in the interactive program STANJAN. Technical report, Mechanical Engineering Department, Stanford University, 1986. 24

E.A. Rodriguez and T.A. Duffey. Fracture-safe and fatigue design criteria for detonation-induced pressure loading in containment vessels. Bulletin 494, Welding Research Council, P.O. Box 1942, New York, NY, 2004. 15

Eric Schultz. *Detonation Diffraction Through an Abrupt Area Expansion*. PhD thesis, California Institute of Technology, Pasadena, California, April 2000. 59

J. E. Shepherd. Structural response of piping to internal gas detonation. In *ASME Pressure Vessels and Piping Conference*. ASME, 2006. PVP2006-ICPVT11-93670, to be presented July 23-27 2006 Vancouver BC Canada. 13, 16, 19

J. E. Shepherd. Chemical kinetics of hydrogen–air–diluent detonations. *Prog. Astronaut. Aeronaut.*, 106:263–293, 1986. 25

J. E. Shepherd, A. Teodorcyzk, R. Knystautas, and J. H. Lee. Shock waves produced by reflected detonations. In *Progress in Astronautics and Aeronautics*, volume 134, pages 244–264. 1991. 16

J. E. Shepherd, J. Karnesky, F. Pintgen, and J. C. Krok. Experimental measurements of strains and blast waves resulting from detonations in tubes. Technical Report FM2006.010, Graduate Aeronautical Laboratories, California Institute of Technology, 2008. 24, 26, 29, 31, 32, 38

J.E. Shepherd, E. Schultz, and R. Akbar. Detonation diffraction. In G. Ball, R. Hillier, and G. Roberts, editors, *Proceedings of the 22nd International Symposium on Shock Waves*, volume 1, pages 41–48, 2000. 59

G.P. Smith, D.M. Golden, M. Frenklach, N.W. Moriarty, B. Eiteneer, M. Goldenberg, C.T. Bowman, R.K. Hanson, S. Song, V.V. Lissianski W.C. Gardiner, and Z. Qin. GRI-Mech 3.0. http://www.me.berkeley.edu/gri_mech, 2004. 25

P.D. Smith and J.G. Hetherington. *Blast and Ballistic Loading of Structures*. Butterworth/Heinemann, 1994. 24

A. Sperber, HP Schildberg, and S. Schlehlein. Dynamic load on a pipe caused by acetylene detonations - experiments and theoretical approaches. *Shock And Vibration*, 6(1):29–43, 1999. 13

P. Thibault, L.G. Britton, and F. Zhang. Deflagration and detonation of ethylene oxide vapor in pipelines. *Process Safety Progress*, 19(3):125–139, 2000. 13

G.O. Thomas. The response of pipes and supports generated by gaseous detonations. *Journal of Pressure Vessel Technology*, 124:66–73, 2002. 13, 14

C. J. Wang, S. L. Xu, and C. M. Guo. Gaseous detonation propagation in a bifrucated channel. *J. Fluid Mech.*, 599:81–110, 2008. 59

R. L. Williams and G. O. Thomas. Detonation interaction with wedges and bends. *Shock Waves*, 11:481–492, 2002. 49, 56

W. C. Young and R. G. Budynas. *Roark's Formulas doe Stress and Strain*. McGraw-Hill, 7th edition, 1989. 75

A Check list

################ Bends and Ts VALIDATION ############################
SHOTNUMBER 7 DATE/TIME: 2006-07-14 16:55:39 WHO: tcurran

Po = 1 bar = 100 kPa Equivalence Ratio = 1
CHAPMAN JOUGUET VALUES:
Ucj = 2375.6 m/s Activation Energy =
Pcj = 33.262 bar = 3.326 MPa Prefl = 83.418 bar = 8.342 MPa
ZSigma = 0.022 mm MaxTempGrad = 0.022 mm
CONSTANT PRESSURE, CONSTANT VOLUME COMBUSTION:
Pcv = 16.794 bar = 1.679 MPa c_cv = 1236.6 m/s
c_isobar = 1126.7 m/s Sigma = 14.2

####### A) Prep & Vac ##
__ 1 Close vacuum hand valve, turn on vacuum pump
__ open hand valve, turn on gas key, evacuate line, turn off gas key
__ open bottlefarm valves.
__ 2 open V1, V2 , V3 , V5, VACUUM, Pressure < 50 mtorr
__ 3 Close VACUUM, check leak rate
__ 4 Zero AMPS
__ 5 Close door to room and DONT ENTER ROOM ANYMORE
__ 6 Turn on WARNING LIGHT

####### B) Filling ##
__ 7 Turn on Gas Key switch
__ 8 Evacuate fill line: Close V5, Press and hold VACCUUM and FEED
__ 9 Pressurize line to experiment: Gas-flow button and FEED
__ 10 Open V5 and fill till desired pressure (last column)

Spec	MolFr	MolFrN	PartP(KPa)	acc(kPa)	P_got(kPA)	MolF_got
C2H4	1.000	0.250	25.00	25.000	25.2	0.250
O2	3.000	0.750	75.00	100.000	100.9	0.750

__ 11 Close V5
__ LOOP through steps 8-11 for all gases
__ 12 Evacuate fill line: Press and hold VACCUUM and FEED
__ 13 Turn off Gas key switch

####### C) Circulate ##
__ 14 Close V1
__ 15 Run circulation pump for 5 min. start time: ____:____
__ final pressure: 100.8 kPa (open and close V1)
__ final temperture: 23.5 C
__ 16 Close V2 , V3
__ 17 CHECK ALL VALVES ARE CLOSED

####### D) Arm & fire ##
__ 18 Check sensor and trigger settings and shotnumber on DAS
__ 19 ARM DAS
__ 20 ! CHECK ALL VALVES CLOSED !
__ 21 ARM spark plug
__ 22 FIRE
__ 23 Switch of spark plug immediately after das triggered

####### E) Data ##
__ 24 check if data and setup file in shot dir
__ 25 Open V1 if temperature below 30C
__ post shot pressure: 63.8 kPa post shot temperature: 28.7 C
__ 26 Open V2 , V3 , V5, VACUUM
__ 27 End of shot series: Close hand valves, Shut of gas key,
__ shut off gas bottle farm, turn off evacuation pump

####### COMMENTS ##

B Data summary for straight aluminium specimen

Table 17: Peak pressure and peak strain for the straight aluminium specimen for the setup of Fig. 10.

shot	t_1	P1	t_2	P2	t_3	P3	S1	S2	S3	S4	S5
	(ms)	(MPa)	(ms)	(MPa)	(ms)	(MPa)	μstrain				
1	0.041	5.08	0.209	6.49	0.62	8.52	2690	3557	4085	2277	3787
2	0.041	4.73	0.212	4.72	0.621	9.87	2578	3438	3873	2474	2954
3	0.035	4.96	0.204	6.34	0.612	9.51	2586	3363	3873	2545	2809
4	0.036	4.82	0.206	6.27	0.616	9.21	2679	3504	3958	2336	2883
5	0.042	4.26	0.213	6.22	0.621	8.76	2615	3486	3832	2403	2775

C Data summary for straight steel specimen

Table 18: Peak pressure and peak strain of the straight steel specimen for the setup of Fig. 15.

shot	P_0	t_1	P1	t_2	P2	t_3	P3	S1	S2	S3	S4	S5
	(bar)	(ms)	(MPa)	(ms)	(MPa)	(ms)	(MPa)	μstrain				
6	1	0.039	4.91	0.203	5.77	0.563	9.48	536	510	450	484	640
7	1	0.038	5.72	0.203	5.57	0.566	9.76	510	538	473	480	583
8	1	0.042	4.63	0.205	4.77	0.571	8.80	497	516	468	492	549
9	1	0.043	4.06	0.206	5.15	0.573	8.87	467	516	541	400	481
10	1	0.003	4.72	0.176	5.39	0.536	10.30	506	535	451	468	555
11	1	0.036	4.26	0.224	4.97	0.578	8.05	520	514	450	425	518
13	0.8	0.031	4.38	0.203	4.93	0.563	13.92	417	448	355	368	461
25	0.8	0.025	4.66	0.196	4.78	0.552	12.28	408	440	386	355	433
14	0.7	0.031	4.09	0.198	4.76	0.567	8.53	353	376	291	324	367
15	0.6	0.031	3.43	0.204	3.72	0.583	6.89	287	306	249	240	300
16	0.5	0.019	2.87	0.191	3.22	0.564	9.89	222	250	237	197	222
26	0.5	0.019	3.02	0.201	2.60	0.576	10.4	242	259	219	226	291
17	0.4	0.028	2.62	0.193	3.82	0.559	6.89	180	197	193	163	169
18	0.3	0.016	1.99	0.195	1.52	0.596	6.69	136	148	151	133	156
19	0.2	0.015	1.44	0.207	1.36	0.612	5.25	89.9	91.8	105	78.7	91.1
20	0.1	0.016	0.52	0.22	0.627	0.59	3.89	57.0	57.7	59.5	62.0	59.5
22	0.07	0.03	0.254	0.663	0.411	0.804	3.342	60.1	57.0	57.0	58.3	56.4
23	0.05	–										

Table 19: Wall thickness measurements (inch) for the straight steel specimens. Measurements taken in the vicinity of the strain gages.

Sample 1				
0.0614	0.0607	0.0607	0.0611	0.0612
0.0607	0.0607	0.0611	0.0611	0.0612
0.0609	0.0606			
average				0.0609
standard deviation				0.0003

Sample 2				
0.0603	0.0608	0.0610	0.0605	0.0602
0.0601	0.0609	0.0607	0.0602	0.0604
average				0.0605
standard deviation				0.0003

D Data summary for bend specimens

Table 20: Wall thickness (inch) measurements for bend specimens.

Sample 1				
Gage No.				average
1	0.0620	0.0612	0.0603	0.0612
2	0.0599	0.0596	0.0604	0.0600
3	0.0603	0.0595	0.0595	0.0598
4	0.0603	0.0596	0.0614	0.0604
5	0.0604	0.0602	0.0614	0.0607
6	0.0622	0.0613	0.0620	0.0618
7	0.0620	0.0624	0.0600	0.0615
8	0.0628	0.0608		0.0618
9	0.0672	0.0659	0.0663	0.0665
10	0.0649	0.0670	0.0667	0.0662
average				0.0620
standard deviation				0.0025

Sample 2				
Gage No.				Average
1	0.0592	0.0596	0.0594	0.0594
2	0.0602	0.0598	0.0602	0.0601
3	0.0597	0.0596	0.0597	0.0597
4	0.0593	0.0597	0.0601	0.0597
5	0.0594	0.0595	0.0598	0.0596
6	0.0598	0.0594	0.0594	0.0595
7	0.0635	0.0642	0.0638	0.0638
8	0.0640	0.0635	0.0654	0.0643
9	0.0664	0.0670	0.0662	0.0665
10	0.0670	0.0668	0.0680	0.0673
11	0.0686	0.0688	0.0688	0.0687
12	0.0687	0.0662	0.0675	0.0675
13	0.0631	0.0630	0.0635	0.0632
14	0.0628	0.0631	0.0628	0.0629
15	0.0629	0.0638	0.0634	0.0634
average				0.0630
standard deviation				0.0033

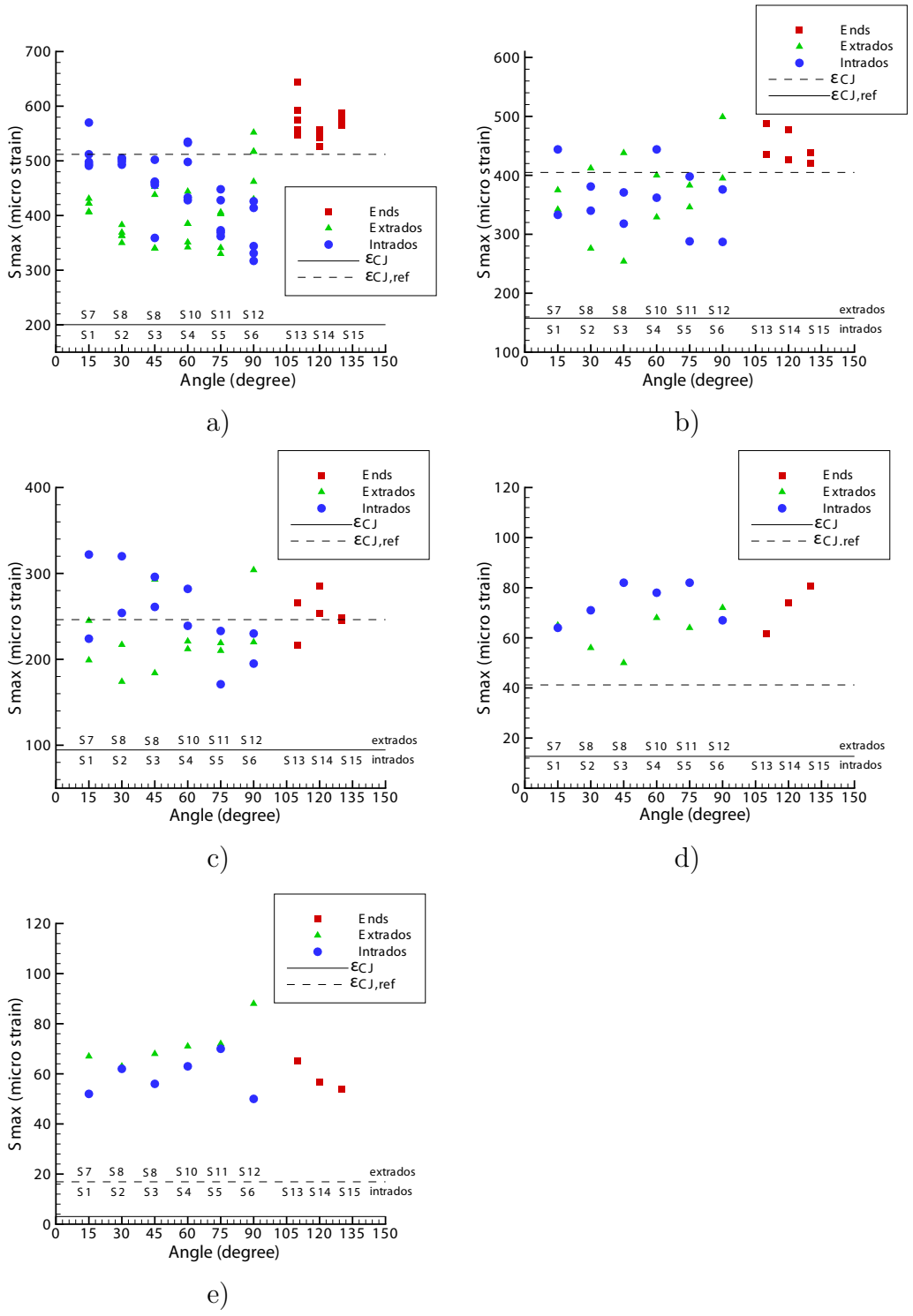

Figure 58: Peak strain vs. location. (a) $P_0 = 1$ bar, (b) $P_0 = 0.8$ bar, (c) $P_0 = 0.5$ bar, (d) $P_0 = 0.1$ bar and (e) $P_0 = 0.05$ bar.

Table 21: Peak pressure and peak strain of the bend specimen for the setup of Fig. 22. Test series B-1.

shot	P_0	t_1	P1	t_2	P2	t_3	P3	S13	S14	S15		
	(bar)	(ms)	(MPa)	(ms)	(MPa)	(ms)	(MPa)	μstrain				
29	1	0.598	5.966	0.763	5.818	1.359	17.60	548	527	576		
30	1	0.639	5.273	0.803	5.164	1.409	14.40	593	542	565		
31	1	0.569	5.328	0.744	4.753	1.33	20.06	644	557	573		
32	1	0.605	5.431	0.771	4.490	1.36	18.08	557	546	567		
33	1	0.637	5.184	0.816	4.314	1.396	19.17	574	547	588		
34	0.8	0.639	3.845	0.808	3.762	1.419	15.96	436	477	439		
35	0.8	0.633	4.648	0.805	4.031	1.409	13.03	488	426	421		
36	0.5	0.815	2.801	0.996	3.586	1.572	11.67	266	285	245		
37	0.5	0.85	2.787	1.01	4.247	1.629	10.37	216	253	248		
38	0.1	4.593	0.144	2.989	0.202	3.258	3.684	61.5	73.8	80.5		
39	0.05	5.177	0.062	4.939	0.108	4.076	3.070	65.1	56.7	53.94		
Peak strain												
shot	S1	S2	S3	S4	S5	S6	S7	S8	S9	S10	S11	S12
	μstrain											
29	407	350	340	342	341	430	498	–	359	433	369	331
30	406	383	340	351	330	552	570	493	462	428	373	426
31	422	363	453	385	403	517	512	499	456	535	448	414
32	449	366	378	386	550	434	491	505	460	498	362	317
33	431	369	438	444	406	462	494	504	502	533	428	344
34	342	276	254	329	346	395	333	340	318	362	288	287
35	375	412	438	400	383	499	444	381	371	444	398	376
36	245	217	184	212	219	304	224	320	296	282	233	230
37	199	174	293	221	210	220	322	254	261	239	171	195
38	65	56	50	68	64	72	64	71	82	78	82	67
39	67	63	68	71	72	88	52	62	56	63	70	50

Table 22: Peak pressure of the bend specimen at 10 intrados locations (see Fig. 26). Test series B-2.

shot	P_0	P1	P2	P4	P5	P6	P7	P8	P9	P10	P3
	(bar)	(MPa)									
81	0.1	5.470	4.188	3.981	3.715	3.425	5.163	–	4.437	4.451	17.53
82	0.1	5.091	4.153	3.948	3.285	3.420	4.592	4.257	4.663	4.233	15.95
83	0.1	4.971	4.011	3.698	3.261	3.482	4.116	4.968	4.382	4.033	17.93
84	0.1	4.691	4.257	3.631	3.083	3.383	3.708	4.423	4.120	3.984	17.52
85	0.08	3.864	4.094	2.699	2.367	2.516	3.007	4.256	3.327	3.318	14.16
86	0.08	3.482	3.843	3.115	2.588	2.745	3.504	4.594	2.943	3.162	13.10
87	0.05	6.745	2.884	2.315	1.971	2.066	2.379	2.612	2.360	2.625	9.16
88	0.05	1.845	2.016	1.949	1.883	2.047	2.327	3.388	2.787	2.165	10.54
89	0.03	0.359	0.485	2.765	2.451	1.480	2.343	2.169	1.072	1.341	21.73
90	0.02	0.093	0.059	0.067	0.033	0.038	0.038	0.033	0.045	0.051	0.136
91	0.015	0.868	0.930	0.716	0.380	0.796	2.108	0.544	0.640	0.697	4.332
Arrival time of the peak pressure.											
shot	P_0	t_1	t_2	t_4	t_5	t_6	t_7	t_8	t_9	t_{10}	t_3
	(bar)	(ms)									
81	0.1	0.587	0.773	1.092	1.102	1.134	1.15	–	1.182	1.2	1.291
82	0.1	0.604	0.771	1.103	1.117	1.132	1.147	1.166	1.179	1.195	1.305
83	0.1	0.592	0.761	1.098	1.112	1.127	1.142	1.161	1.189	1.206	1.3
84	0.1	0.602	0.766	1.108	1.122	1.137	1.153	1.171	1.185	1.2	1.314
85	0.08	0.599	0.762	1.114	1.129	1.147	1.163	1.183	1.196	1.213	1.33
86	0.08	0.701	0.862	1.194	1.209	1.225	1.241	1.261	1.274	1.291	1.41
87	0.05	2.62	2.762	3.062	3.076	3.092	3.107	3.13	3.144	3.158	3.286
88	0.05	0.751	0.941	1.303	1.315	1.332	1.346	1.365	1.381	1.394	1.495
89	0.03	5.447	5.12	4.088	4.102	4.139	4.157	4.175	4.219	4.59	4.377
90	0.02	2.068	2.795	4.288	6.792	6.752	7	6.465	6.348	6.292	5.312
91	0.015	0.894	1.053	1.484	1.516	1.536	1.56	1.6	1.609	1.634	1.767

Table 23: Peak pressure of the bend specimen at 10 extrados locations (see Fig. 26). Test series B-3.

shot	P_0	P1	P2	P4	P5	P6	P7	P8	P9	P10	P3
	(bar)	(MPa)									
94	1	5.405	4.220	4.731	5.818	8.011	11.333	9.718	7.320	6.616	17.107
95	1	5.472	4.525	4.198	5.449	7.562	7.930	8.741	6.439	6.410	16.988
96	0.8	4.142	3.263	3.448	4.249	6.405	6.623	7.950	5.235	5.797	14.839
97	0.8	4.106	3.266	3.648	4.626	7.077	6.598	8.249	5.704	6.983	14.395
98	0.5	1.576	1.995	2.865	3.851	5.292	5.367	7.511	5.125	4.232	10.916
99	0.5	2.549	2.343	1.866	2.634	3.838	4.218	5.877	4.035	3.643	9.534
100	0.3	1.722	2.107	1.033	1.285	1.079	1.690	3.647	1.545	1.139	7.164
101	0.2	0.252	5.326	1.199	1.807	2.542	2.080	3.970	1.613	1.565	7.402
Arrival time of the peak pressure.											
shot	P_0	t_1	t_2	t_4	t_5	t_6	t_7	t_8	t_9	t_{10}	t_3
	(bar)	(ms)									
94	1	0.631	0.805	1.13	1.147	1.165	1.182	1.197	1.212	1.229	1.335
95	1	0.583	0.759	1.086	1.107	1.125	1.138	1.154	1.168	1.185	1.291
96	0.8	0.639	0.827	1.154	1.172	1.193	1.206	1.222	1.237	1.255	1.358
97	0.8	0.579	0.756	1.1	1.120	1.138	1.151	1.166	1.18	1.200	1.299
98	0.5	0.770	0.984	1.306	1.321	1.337	1.352	1.368	1.381	1.396	1.495
99	0.5	0.836	1.010	1.421	1.441	1.461	1.479	1.498	1.513	1.53	1.635
100	0.3	0.831	0.995	1.426	1.43	1.456	1.483	1.511	1.53	1.555	1.696
101	0.2	6.816	5.248	5.544	5.562	5.581	5.595	5.615	5.63	5.65	5.781

Table 24: Peak pressure of the bend specimen at 10 locations (see Fig. 31). Test series B-4.

shot	P_0	P1	P2	P4	P5	P6	P7	P8	P9	P10	P3
	(bar)	(MPa)									
107	1	5.218	4.372	4.364	3.032	8.104	4.724	7.917	4.618	5.715	15.811
106	0.8	4.406	3.558	3.415	2.458	6.650	4.111	7.021	3.273	4.607	12.434
105	0.5	2.223	2.085	2.016	1.510	4.846	2.710	5.913	2.125	3.015	10.489
103	0.3	1.335	1.765	1.083	0.770	2.666	1.220	3.697	1.293	1.821	6.618
104	0.2	0.982	1.803	0.933	0.551	1.305	1.100	2.130	0.865	0.804	7.692
108	0.1	0.175	0.204	0.816	0.376	1.630	0.419	1.639	0.492	0.970	3.496
Arrival time of the peak pressure.											
	P_0	t_1	t_2	t_4	t_5	t_6	t_7	t_8	t_9	t_{10}	t_3
	(bar)	(ms)									
107	1	0.576	0.752	1.083	1.130	1.123	1.162	1.152	1.192	1.186	1.288
106	0.8	0.66	0.846	1.166	1.213	1.205	1.243	1.235	1.276	1.269	1.374
105	0.5	0.781	0.957	1.327	1.369	1.362	1.403	1.395	1.435	1.447	1.526
103	0.3	0.956	1.111	1.456	1.492	1.498	1.531	1.537	1.571	1.575	1.706
104	0.2	1.594	1.746	2.101	2.156	2.150	2.195	2.197	2.244	2.247	2.392
108	0.1	4.378	2.865	2.938	2.969	2.957	2.997	2.999	3.466	3.036	3.166

E Data summary for tee specimens

Table 25: Wall thickness (inch) measurements for tee specimen No. 1.

Sample 1				
Gage No.				average
1	0.0630	0.0631	0.0635	0.0632
2	0.0636	0.0633	0.0634	0.0634
3	0.0631	0.0625	0.0627	0.0628
4	0.0624	0.0622	0.0619	0.0622
5	0.0621	0.0622	0.0619	0.0621
6	0.0609	0.0613	0.0611	0.0611
7	0.0611	0.0612	0.0615	0.0613
8	0.0619	0.0617	0.0615	0.0617
9	0.0616	0.0619	0.0618	0.0618
10	0.0614	0.0617	0.0609	0.0613
11	0.0626	0.0619	0.0617	0.0621
12	0.0613	0.0617	0.0613	0.0614
13	0.0619	0.0615	0.0619	0.0618
14	0.0622	0.0626	0.0621	0.0623
15	0.0617	0.0618	0.0620	0.0618
average				0.0620
standard deviation				0.0007

Table 26: Peak pressure and peak strain for the tee specimen for the setup of Fig. 36. Test series T-1.

shot	P_0	t_1	P1	t_2	P2	t_3	P3	t_4	P4	S1	S2	S3
	(bar)	(ms)	(MPa)	(ms)	(MPa)	(ms)	(MPa)	(ms)	(MPa)	(μstrain)		
40	1	0.614	4.14	0.784	5.20	1.132	12.28	1.142	13.51	921	540	470
41	1	0.575	5.41	0.746	5.04	1.091	12.21	1.107	11.13	954	484	506
42	1	0.593	5.37	0.761	4.64	1.111	11.94	1.121	13.37	870	516	480
43	1	0.59	4.14	0.766	4.41	1.109	13.03	1.119	11.13	530	496	499
44	1	0.597	4.50	0.761	4.83	1.109	13.03	1.121	12.56	537	523	506
45	1	0.563	4.59	0.73	4.04	1.078	12.96	1.088	13.24	532	519	483
46	1	0.606	4.99	0.77	4.69	1.121	12.14	1.131	12.35	530	524	491
47	0.8	0.659	4.19	0.829	3.96	1.179	8.60	1.192	9.64	446	436	337
48	0.8	0.667	4.10	0.836	4.26	1.186	10.7	1.2	8.89	423	424	372
49	0.5	0.72	2.42	0.891	2.51	1.246	8.05	1.255	6.38	253	229	242
50	0.5	0.691	2.36	0.872	2.37	1.226	7.85	1.237	6.04	235	201	205
51	0.1	1.531	0.81	1.667	0.91	2.04	2.87	2.041	2.38	55	43	54
52	0.05	1.686	0.096	2.109	0.162	2.545	1.978	2.534	1.358	54	36	42
Peak strain												
shot	S4	S5	S6	S7	S8	S9	S10	S11	S12	S13	S14	S15
	(μstrain)											
40	493	650	206	278	373	274	514	489	415	872	795	1135
41	483	700	277	283	374	287	493	473	444	858	918	1132
42	471	687	229	286	365	277	532	474	485	901	832	1117
43	512	706	262	286	363	319	490	474	480	960	791	1068
44	542	677	297	271	358	334	461	476	457	959	751	1112
45	556	663	308	291	362	294	479	461	464	944	728	1081
46	540	686	237	325	356	297	427	474	422	947	691	1037
47	431	552	225	350	282	295	413	380	353	670	557	654
48	439	577	181	283	283	268	474	429	355	597	511	684
49	271	373	148	237	166	205	335	308	234	284	378	472
50	251	358	138	187	154	182	266	278	243	286	341	442
51	58.4	65.6	48.1	72.0	43.6	43.0	63.0	60.0	62.8	58.2	66.8	57.9
52	39.9	45.4	30.4	28.1	32.9	28.7	31.9	38.3	40.0	46.0	48.1	51.7

Table 27: Peak pressure and peak strain for the tee specimen using the setup of Fig. 43. Test series T-2.

shot	P_0	t_1	P1	t_2	P2	t_3	P3	t_4	P4
	(bar)	(ms)	(MPa)	(ms)	(MPa)	(ms)	(MPa)	(ms)	(MPa)
53	1	0.598	4.30	0.768	4.21	1.114	11.05	1.127	12.76
54	1	0.579	4.54	0.757	4.56	1.098	13.17	1.11	10.05
55	0.8	0.649	3.48	0.818	3.84	1.178	8.53	1.187	8.15
56	0.5	0.814	2.15	0.975	2.50	1.339	5.39	1.345	6.65

Table 28: Peak pressure and peak strain for the tee specimen using the setup of Fig. 45. Test series T-3.

shot	P_0	t_1	P1	t_2	P2	t_3	P3	t_4	P4	S15	S8	S9
	(bar)	(ms)	(MPa)	(ms)	(MPa)	(ms)	(MPa)	(ms)	(MPa)	(μstrain)		
60	1	0.59	5.547	0.761	4.807	0.974	4.883	1.135	12.965	505	321	–
61	1	0.59	4.346	0.758	4.200	0.849	4.883	1.126	17.106	517	337	457
Peak strain												
shot	S1	S2	S3	S2*	S3*	S4	S5	S4*	S5*	S6	S7	
	(μstrain)											
60	447	335	313	423	451	430	461	436	408	148	202	
61	502	385	348	405	419	348	464	498	410	204	252	

Table 29: Peak pressure and peak strain for the tee specimen using the setup of Fig. 47. Test series T-4.

shot	P_0	t_1	P1	t_2	P2	t_3	P3	t_4	P4	S8	S9	S15
	(bar)	(ms)	(MPa)	(ms)	(MPa)	(ms)	(MPa)	(ms)	(MPa)	(μstrain)		
62	1	0.59	5.547	0.761	4.807	-0.974	4.883	1.135	12.965	321	–	505
63	1	0.59	4.346	0.758	4.200	-0.849	4.883	1.126	17.106	337	457	517
Peak strain												
shot	S1	S2	S3	S2*	S3*	S4	S5	S4*	S5*	S6	S7	
	(μstrain)											
62	447	335	313	423	451	430	461	436	408	148	202	
63	502	385	348	405	419	348	464	498	410	204	252	

Table 30: Peak pressure and peak strain for the tee specimen using the setup of Fig. 49. Test series T-5.

shot	P_0	t_1	P1	t_2	P2	t_3	P3	t_4	P4	End
	(bar)	(ms)	(MPa)	(ms)	(MPa)	(ms)	(MPa)	(ms)	(MPa)	
77	1	0.59	5.547	0.761	4.807	-0.974	4.883	1.135	12.965	open
78	1	0.59	4.346	0.758	4.200	-0.849	4.883	1.126	17.106	open
79	1	0.599	5.122	0.767		1.151	9.074	1.294	11.500	close
80	1	0.607	4.772	0.771		1.153	9.824	1.293	11.500	close
Peak strain at 6 locations.										
shot	P_0	S1	S2	S3	S2*	S3*	S15			
	(bar)	(μstrain)								
77	1	446.5	334.7	312.7	423.2	451.4	505.0			
78	1	501.5	385.0	348.3	404.6	419.4	516.8			
79	1	504.6	427.0	370.8	486.5	473.1	484.1			
80	1	443.1	370.1	350.2	410.3	454.4	500.9			
Peak strain at 8 locations.										
shot	P_0	S4	S5	S4*	S5*	S6	S7	S8	S9	
	(bar)	(μstrain)								
77	1	430.4	461.0	435.6	407.8	147.8	201.5	321.4	–	
78	1	347.7	464.1	498.1	410.4	203.7	251.7	337.0	457.3	
79	1	485.3	538.0	610.6	477.0	301.3	468.0	355.4	1252.0	
80	1	443.9	495.7	552.2	479.5	308.0	434.0	316.0	1252.0	

Table 31: Peak pressure and peak strain for the tee specimen using the setup of Fig. 45. Test series T-6. In shots 109 and 110, the vertical branch was vented. In shot 111, the horizontal branch was vented, and in shot 12, both branches were vented.

shot	P_0	t_1	P1	t_2	P2	t_3	P3	t_4	P4	S15	S8	S9
	(bar)	(ms)	(MPa)	(ms)	(MPa)	(ms)	(MPa)	(ms)	(MPa)	μstrain		
109	0.1	0.62	6.014	0.808	4.368	–	–	1.161	14.53	613	334	1106
110	0.1	0.627	5.472	0.801	4.031	–	–	1.171	22.04	651	400	1167
111	0.1	0.6	5.273	0.765	4.402	1.127	22.92	–	–	614	363	1252
112	0.1	0.643	5.925	0.829	3.829	–	–	–	–	525	338	391
peak strain												
shot	S1	S2	S3	S2*	S3*	S4	S5	S4*	S5*	S6	S7	
	(μstrain)											
109	–	296	374	360	371	403	569	394	394	185	244	
110	–	434	469	361	368	467	566	372	395	131	301	
111	–	317	357	339	368	411	552	371	396	163	225	
112	476	271	300	343	367	283	448	350	371	179	207	

Table 32: Peak pressure for the tee specimen using the setup of Fig. 52. Test series T-7.

shot	P_0	P1	P2	P12	P5	P6	P7	P8	P9	P10	P11	P3	P4
	(bar)	(MPa)											
65	0.1	4.24	5.91	5.04	4.86	5.64	4.62	5.40	5.53	6.22	7.80	17.76	16.46
66	0.1	4.40	5.36	5.22	4.76	4.30	4.31	5.42	4.60	5.78	7.77	18.35	17.14
67	0.1	4.45	5.07	5.08	4.86	4.86	4.87	5.04	5.42	6.03	7.56	18.85	15.95
68	0.08	3.74	4.07	4.21	3.86	4.32	3.78	4.87	4.87	3.87	6.08	14.33	13.70
69	0.08	3.88	3.48	4.70	3.43	4.09	3.89	4.76	4.31	3.68	6.28	15.23	14.02
70	0.05	1.72	2.52	3.00	2.05	4.39	3.02	4.20	3.88	2.13	3.92	10.01	8.81
76	0.05	2.33	2.42	3.55	2.20	2.29	3.05	2.99	3.87	1.98	4.34	10.23	9.16
71	0.02	0.58	0.72	1.51	1.02	1.33	1.50	1.48	2.64	1.24	2.13	6.26	4.92
72	0.01	0.13	0.20	1.94	0.87	0.49	0.91	1.19	1.63	0.64	0.94	3.41	3.75
75	0.01	0.27	0.42	0.73	0.48	0.42	4.23	1.43	0.73	0.67	1.30	4.62	3.53
73	0.005	0.17	0.45	0.29	0.23	0.28	1.25	0.83	0.43	0.33	0.45	2.03	2.02
74	0.005	0.13	0.79	0.48	0.33	0.25	3.07	1.04	0.43	0.33	0.54	2.47	2.21
Arrival time of the peak pressure.													
	P_0	t_1	t_2	t_{12}	t_5	t_6	t_7	t_8	t_9	t_{10}	t_{11}	t_3	t_4
	(bar)	(ms)											
65	0.1	0.58	0.75	0.99	1.37	1.00	1.01	1.01	1.01	1.10	1.12	1.11	1.12
66	0.1	0.62	0.78	1.02	1.36	1.41	1.05	1.33	1.05	1.17	1.15	1.14	1.15
67	0.1	0.61	0.78	1.02	1.40	1.03	1.43	1.04	1.05	1.17	1.15	1.14	1.15
68	0.08	0.66	0.83	1.07	1.45	1.46	1.48	1.09	1.10	1.22	1.20	1.19	1.20
69	0.08	0.65	0.82	1.06	1.44	1.08	1.47	1.08	1.09	1.21	1.19	1.18	1.19
70	0.05	0.77	0.93	1.17	1.51	1.18	1.20	1.19	1.20	1.32	1.30	1.29	1.30
76	0.05	0.71	0.88	1.12	1.52	1.14	1.15	1.14	1.15	1.28	1.26	1.25	1.26
71	0.02	0.86	1.06	1.32	1.64	1.69	1.35	1.35	1.35	1.43	1.45	1.44	1.44
72	0.01	2.96	2.71	2.64	2.98	2.99	2.68	2.66	2.66	2.74	2.77	2.76	2.76
75	0.01	1.01	1.22	1.47	1.78	1.82	1.51	1.49	1.52	1.59	1.60	1.59	1.59
73	0.005	1.66	1.89	2.14	2.15	2.55	2.18	2.16	2.17	2.26	2.29	2.28	2.27
74	0.005	1.51	1.85	2.06	2.42	2.45	2.10	2.08	2.09	2.23	2.20	2.19	2.19

F Plots - straight aluminium specimen

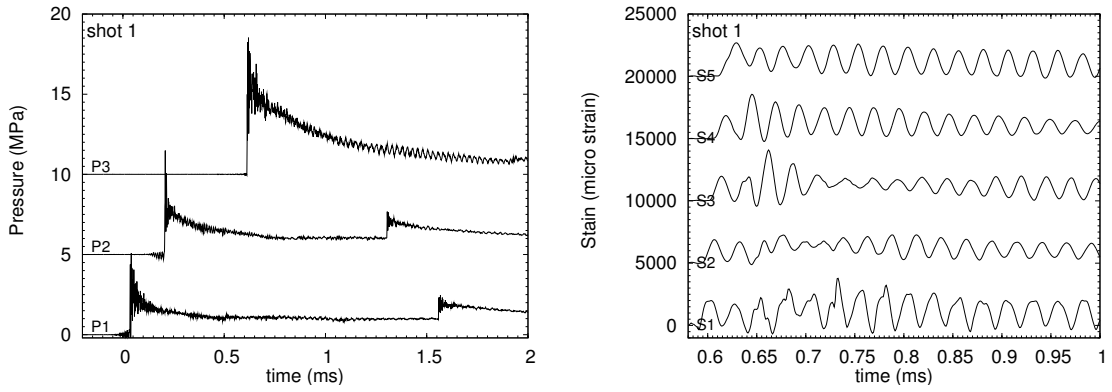

Figure 59: Pressure and strain traces, shot 1, aluminium straight specimen, $P_0 = 1$ bar

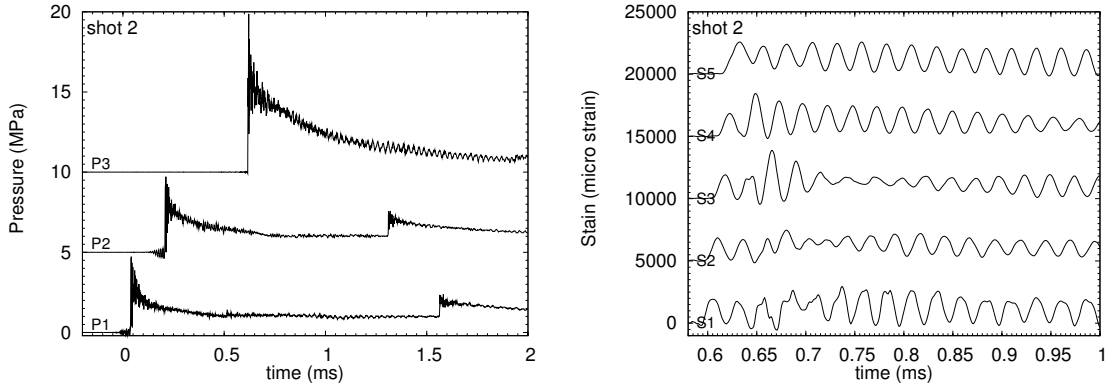

Figure 60: Pressure and strain traces, shot 2, aluminium straight specimen, $P_0 = 1$ bar

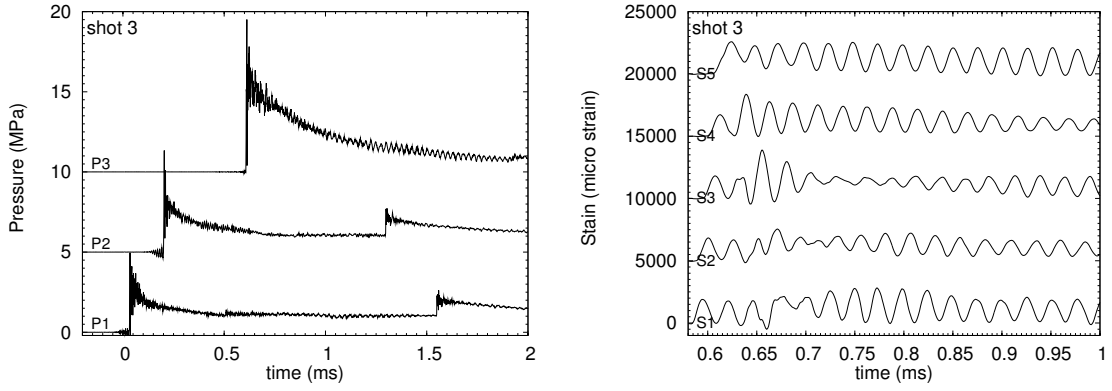

Figure 61: Pressure and strain traces, shot 3, aluminium straight specimen, $P_0 = 1$ bar

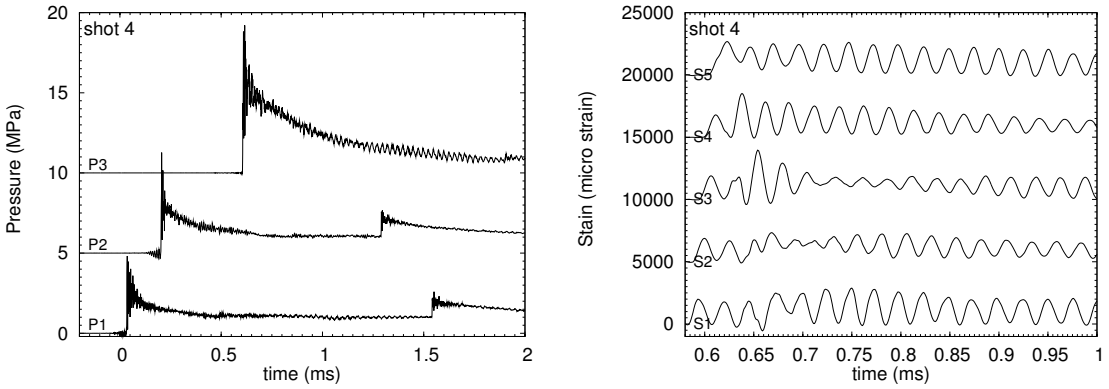

Figure 62: Pressure and strain traces, shot 4, aluminium straight specimen, $P_0 = 1$ bar

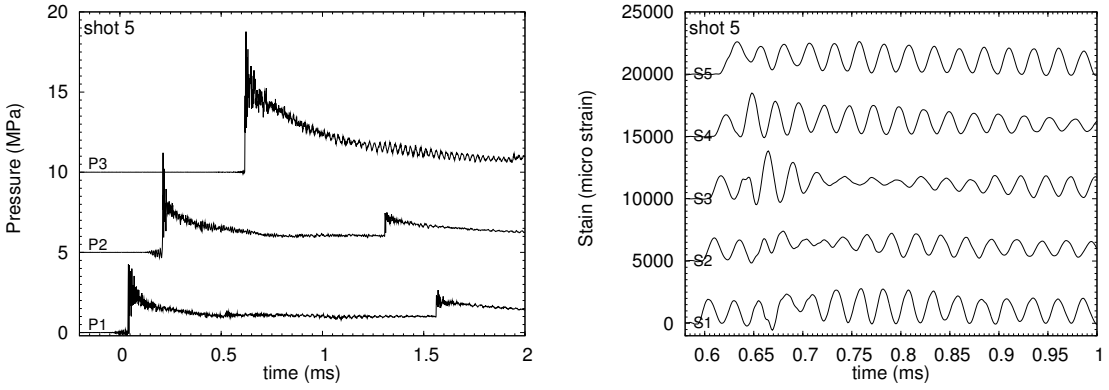

Figure 63: Pressure and strain traces, shot 5, aluminium straight specimen, $P_0 = 1$ bar

G Plots - straight steel specimen

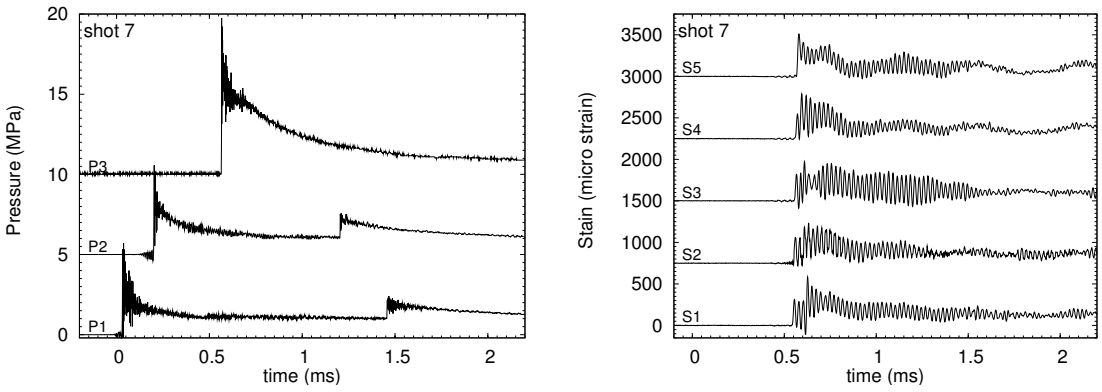

Figure 64: Pressure and strain traces, shot 7, steel straight specimen, $P_0 = 1$ bar

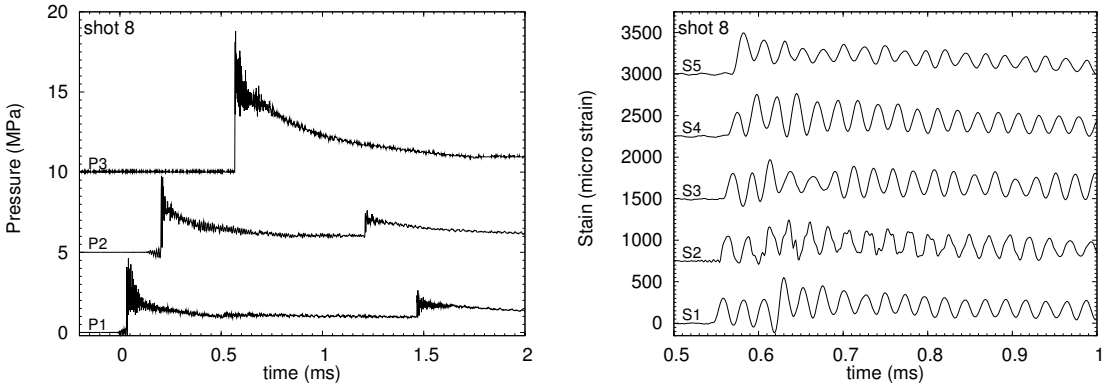

Figure 65: Pressure and strain traces, shot 8, steel straight specimen, $P_0 = 1$ bar

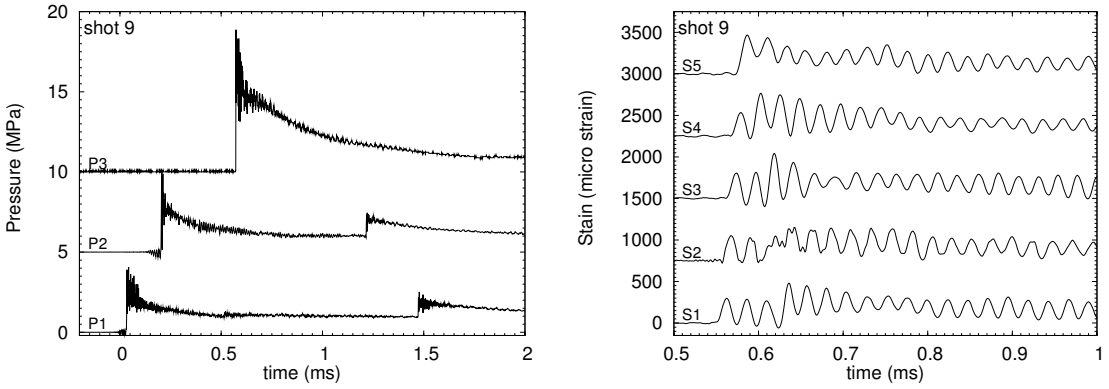

Figure 66: Pressure and strain traces, shot 9, steel straight specimen, $P_0 = 1$ bar

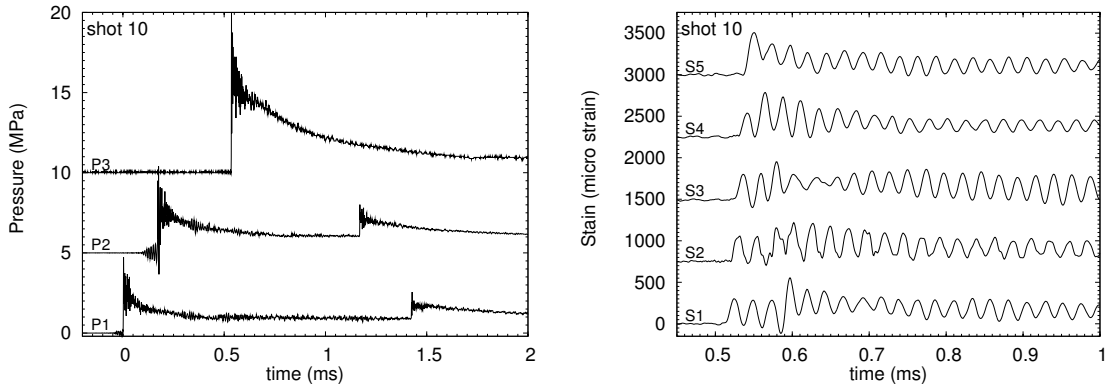

Figure 67: Pressure and strain traces, shot 10, steel straight specimen, $P_0 = 1$ bar

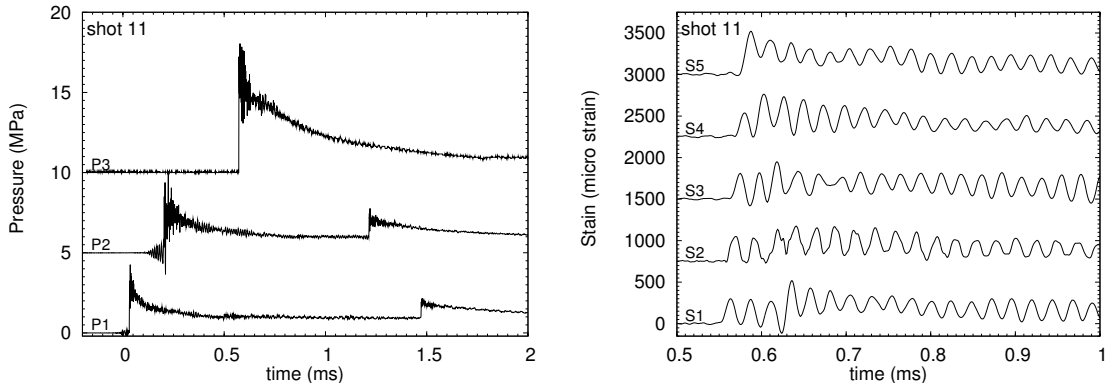

Figure 68: Pressure and strain traces, shot 11, steel straight specimen, $P_0 = 1$ bar

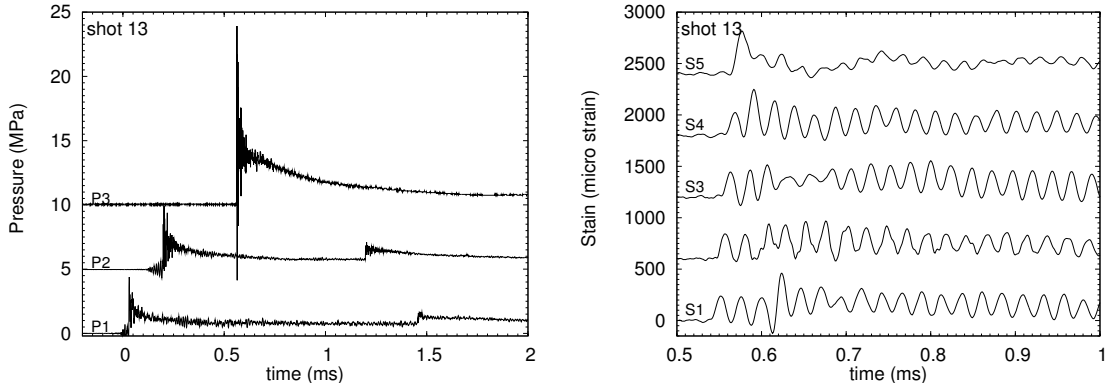

Figure 69: Pressure and strain traces, shot 13, steel straight specimen, $P_0 = 0.8$ bar

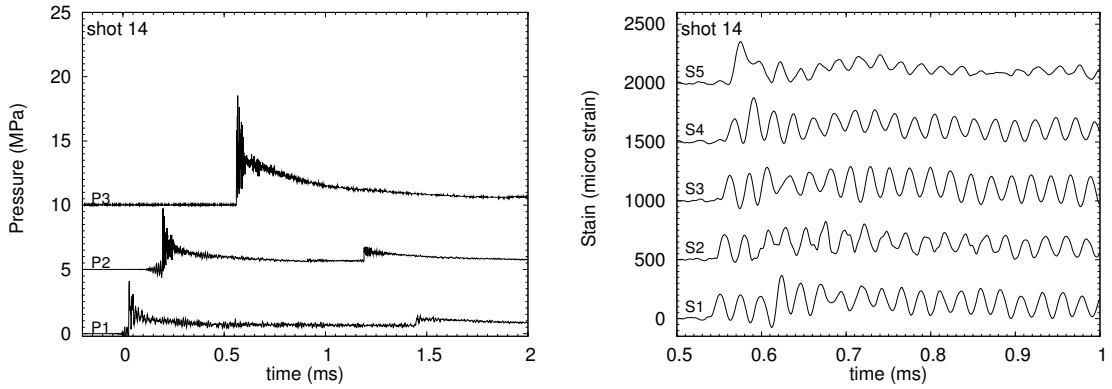

Figure 70: Pressure and strain traces, shot 14, steel straight specimen, $P_0 = 0.7$ bar

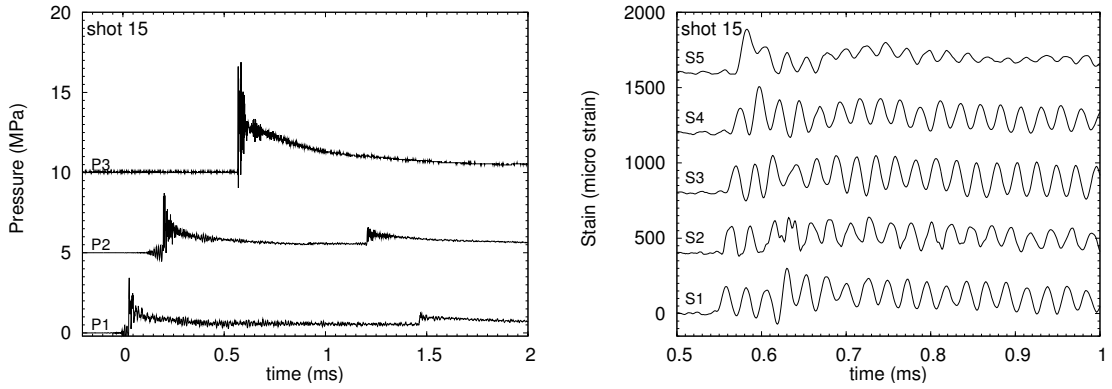

Figure 71: Pressure and strain traces, shot 15, steel straight specimen, $P_0 = 0.6$ bar

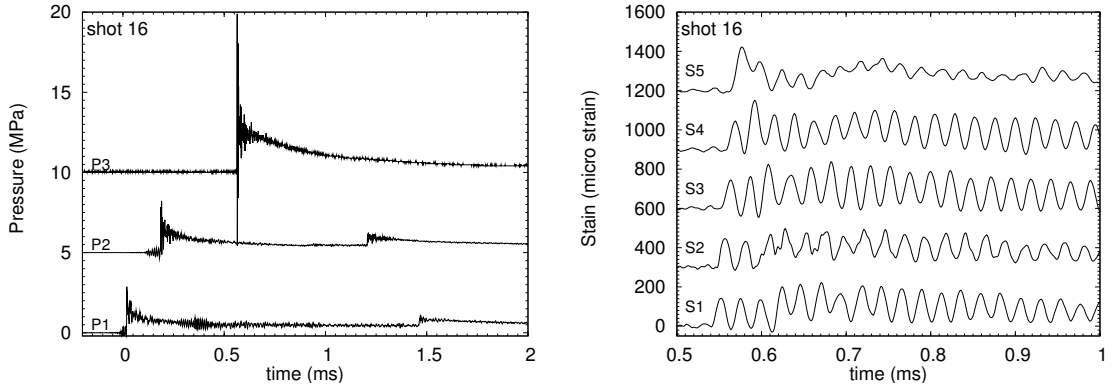

Figure 72: Pressure and strain traces, shot 16, steel straight specimen, $P_0 = 0.5$ bar

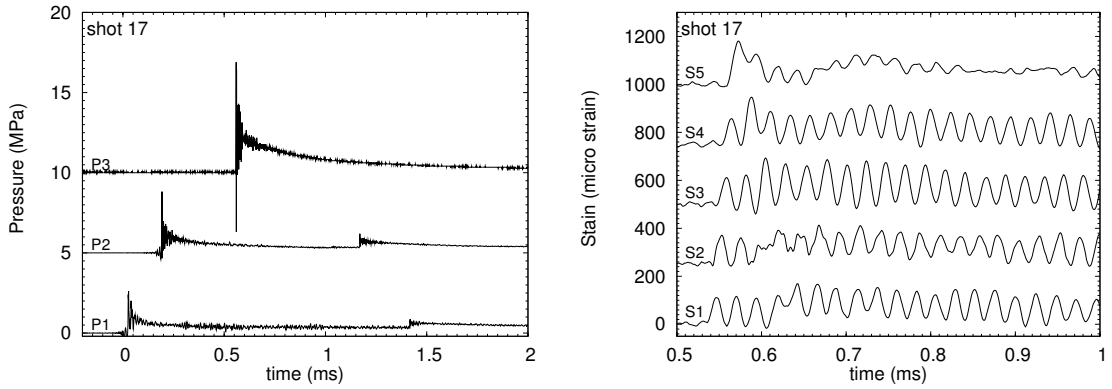

Figure 73: Pressure and strain traces, shot 17, steel straight specimen, $P_0 = 0.4$ bar

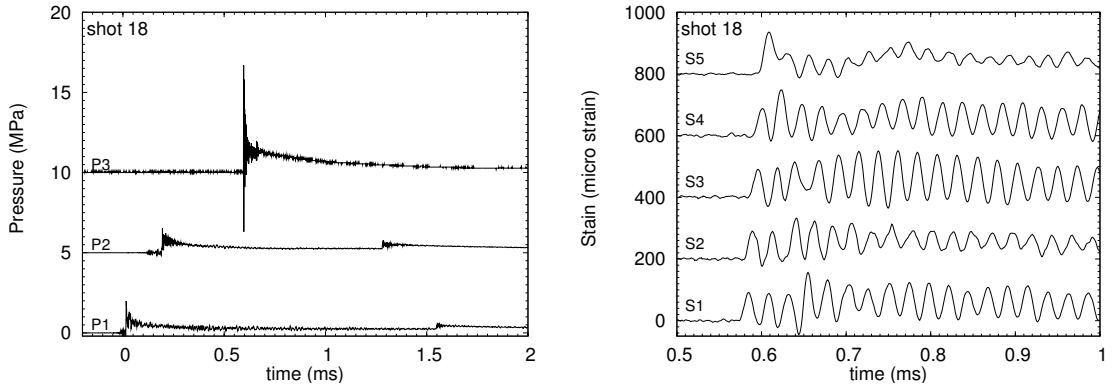

Figure 74: Pressure and strain traces, shot 18, steel straight specimen, $P_0 = 0.3$ bar

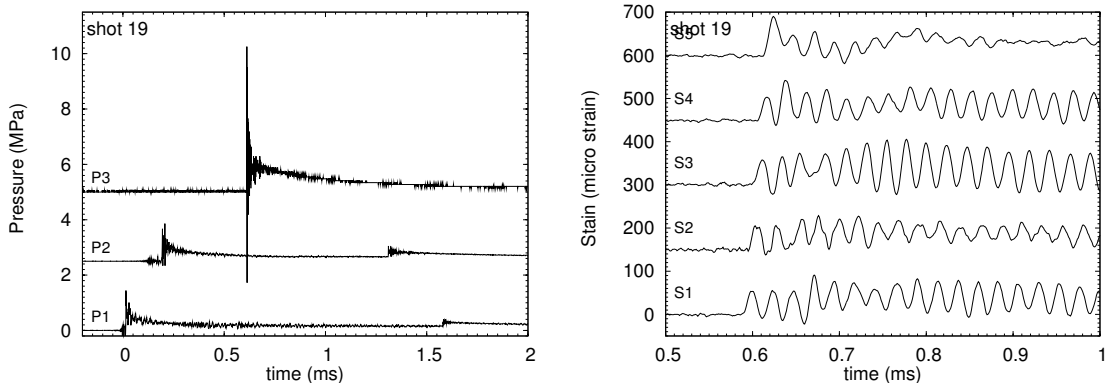

Figure 75: Pressure and strain traces, shot 19, steel straight specimen, $P_0 = 0.2$ bar

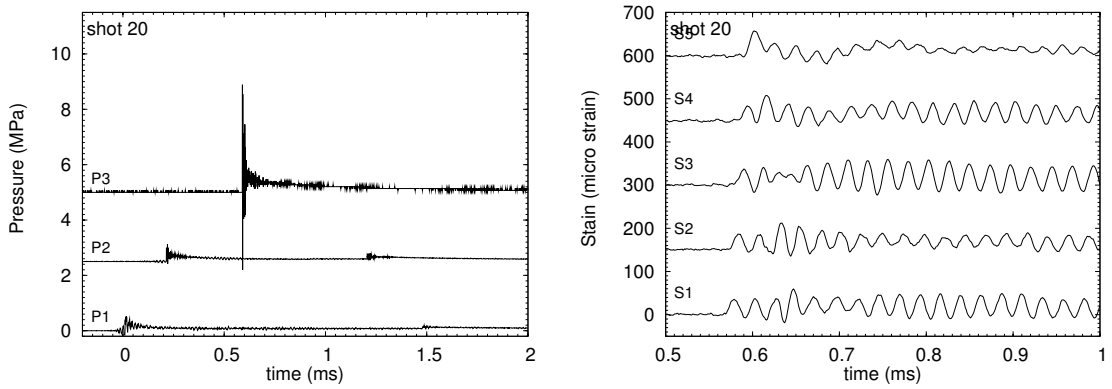

Figure 76: Pressure and strain traces, shot 20, steel straight specimen, $P_0 = 0.1$ bar

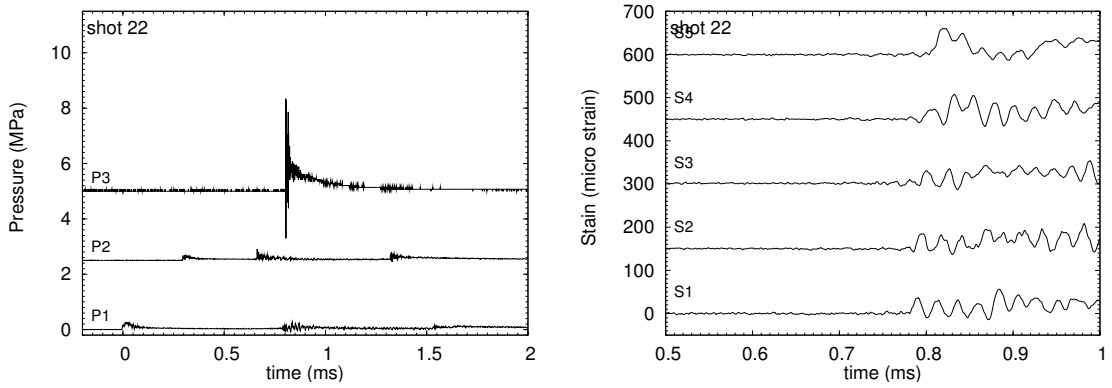

Figure 77: Pressure and strain traces, shot 22, steel straight specimen, $P_0 = 0.07$ bar

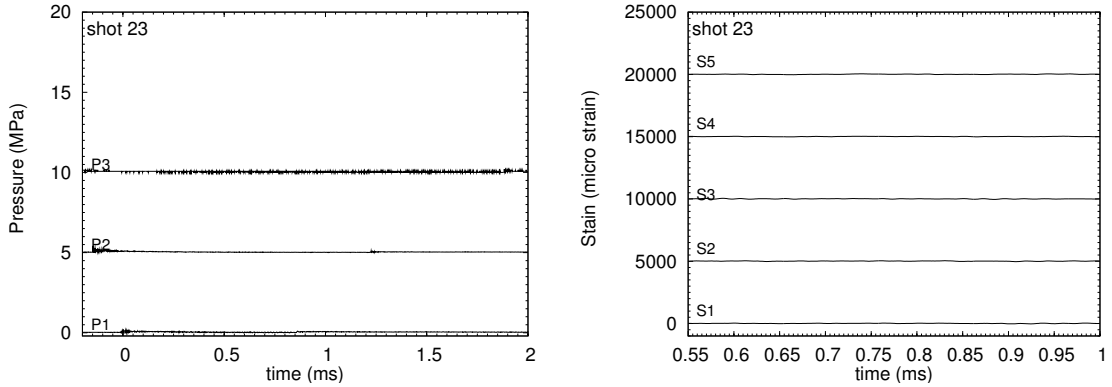

Figure 78: Pressure and strain traces, shot 23, steel straight specimen, $P_0 = 0.063$ bar

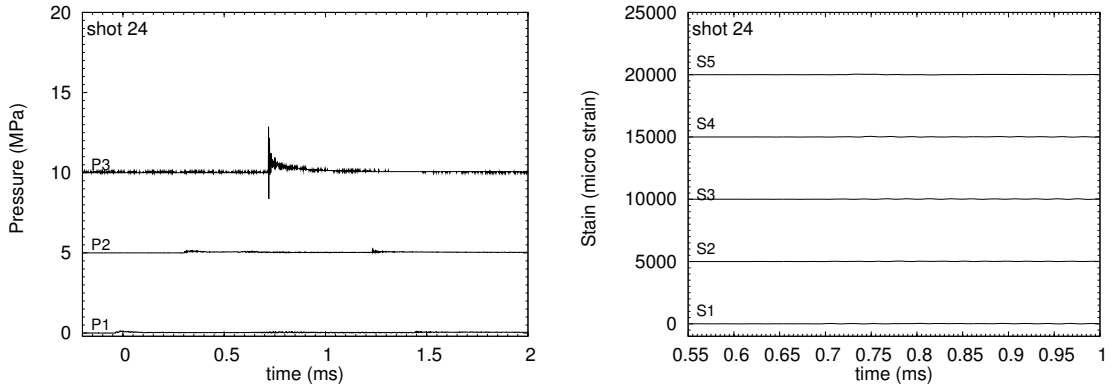

Figure 79: Pressure and strain traces, shot 24, steel straight specimen, $P_0 = 0.05$ bar

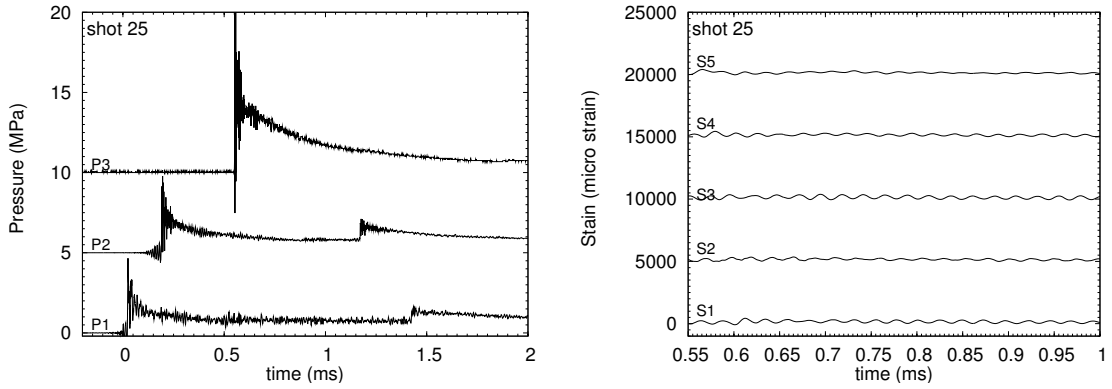

Figure 80: Pressure and strain traces, shot 25, steel straight specimen, $P_0 = 0.8$ bar

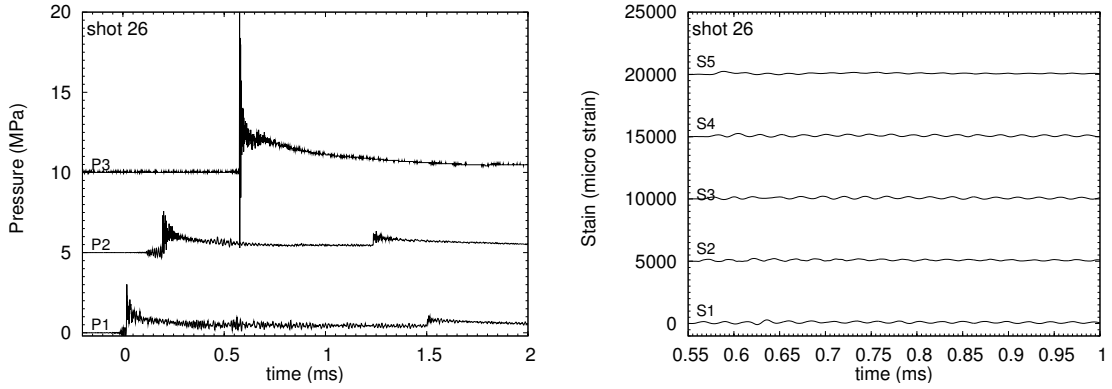

Figure 81: Pressure and strain traces, shot 26, steel straight specimen, $P_0 = 0.5$ bar

H Plots - bend specimens

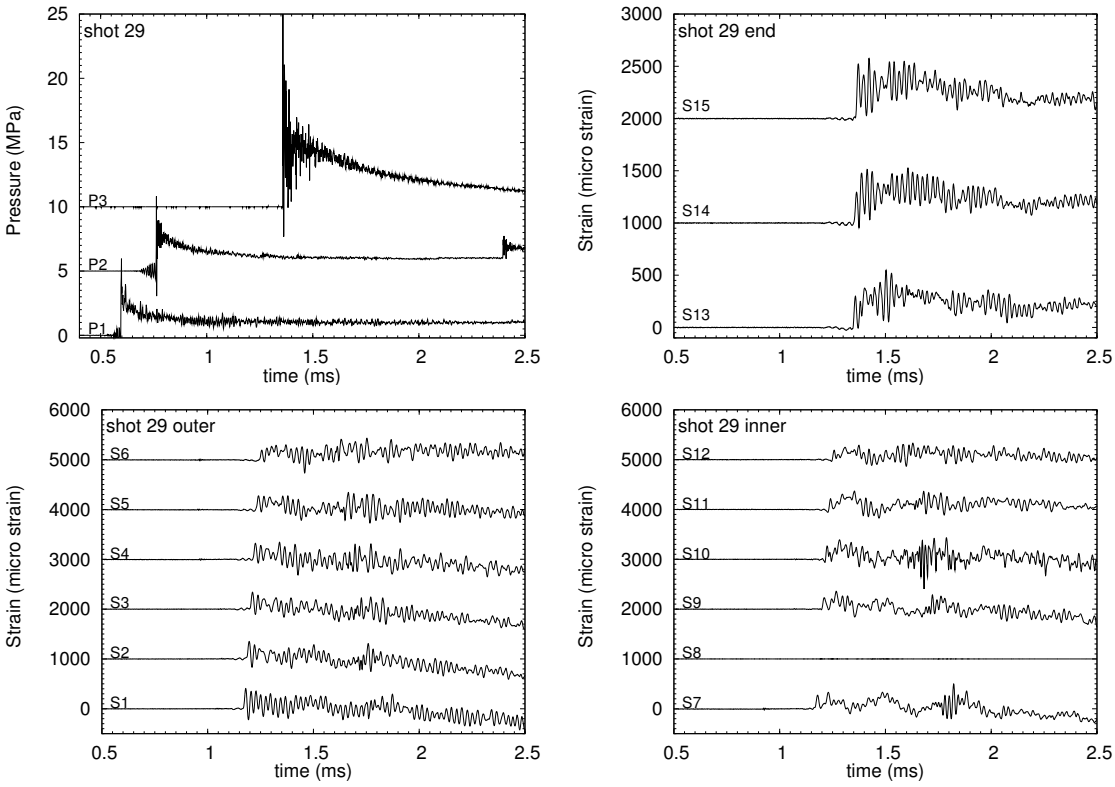

Figure 82: Pressure and strain traces, shot 29, bend specimen, $P_0 = 1$ bar

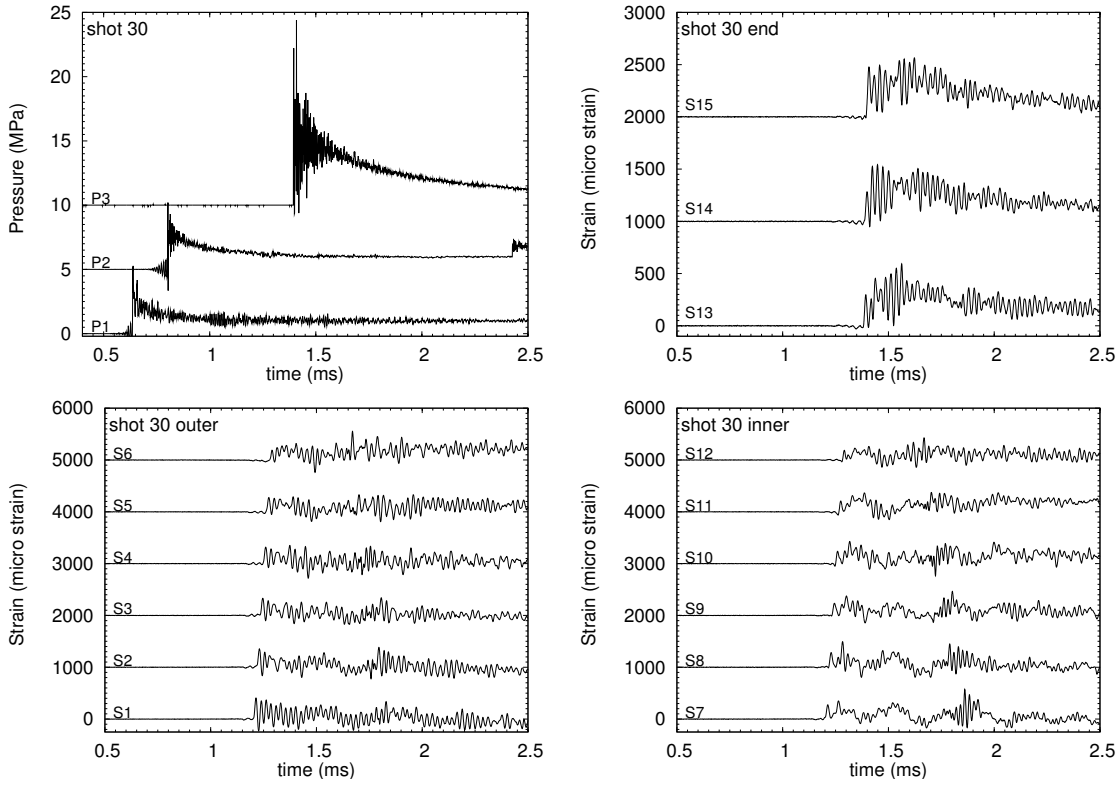

Figure 83: Pressure and strain traces, shot 30, bend specimen, $P_0 = 1$ bar

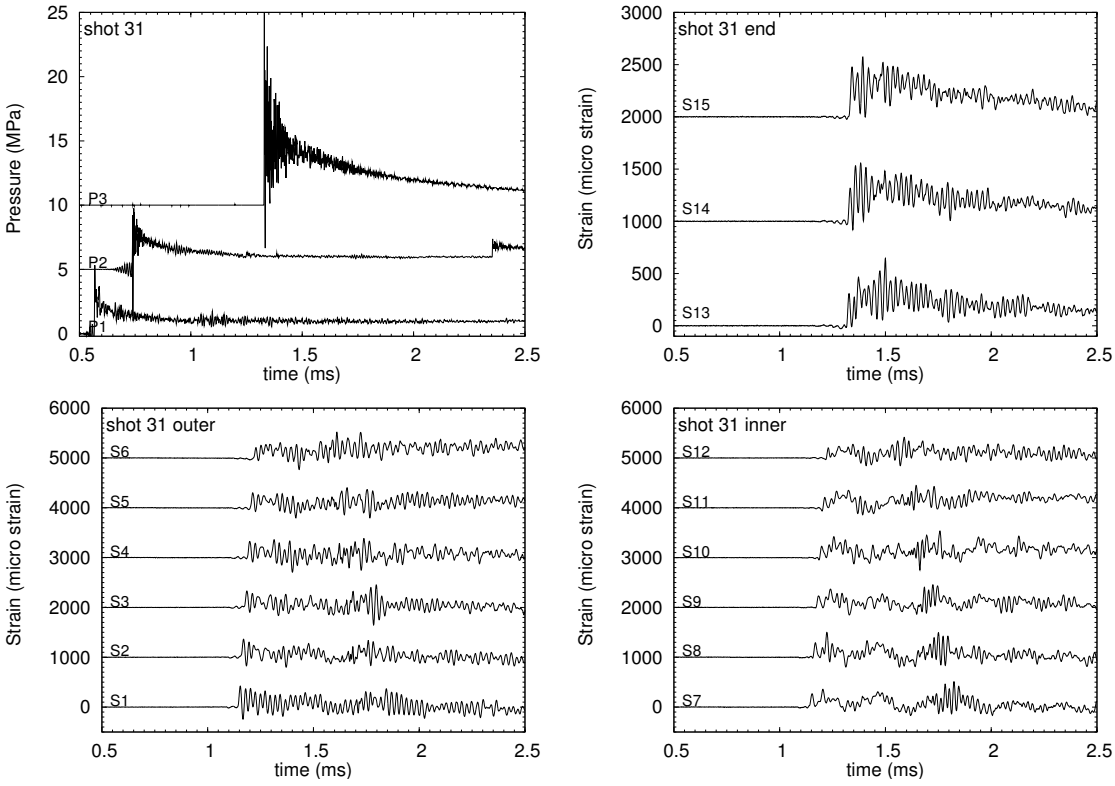

Figure 84: Pressure and strain traces, shot 31, bend specimen, $P_0 = 1$ bar

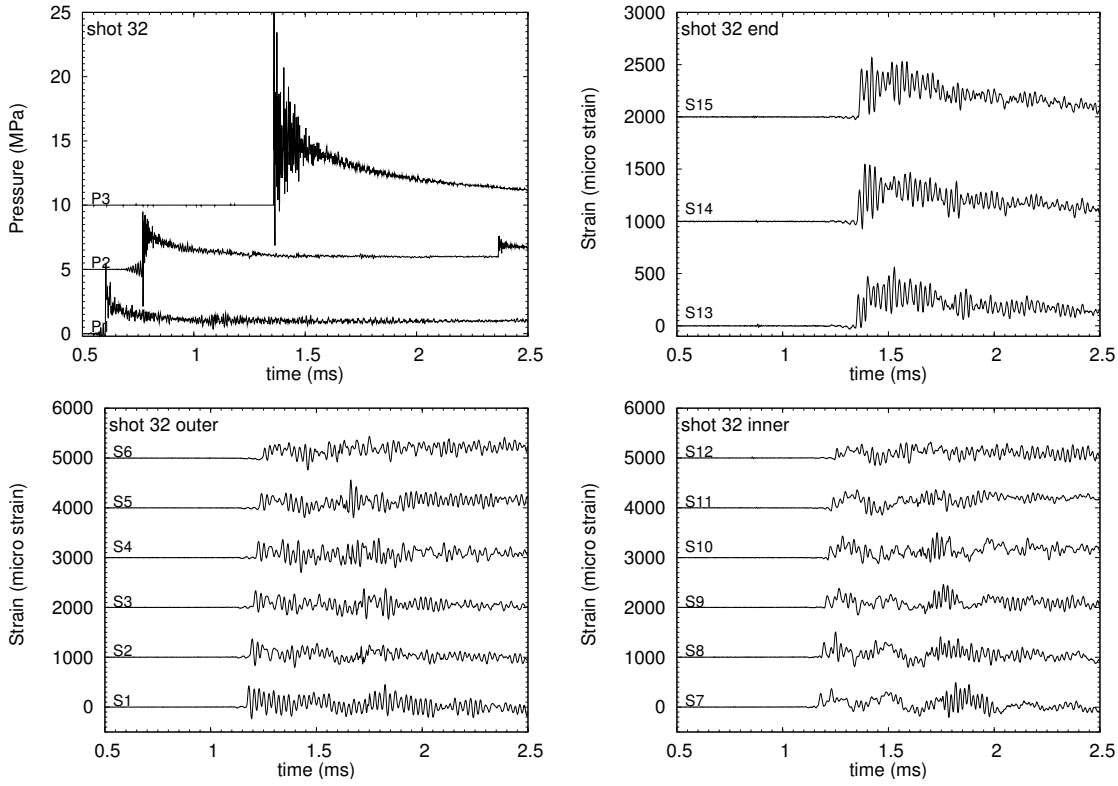

Figure 85: Pressure and strain traces, shot 32, bend specimen, $P_0 = 1$ bar

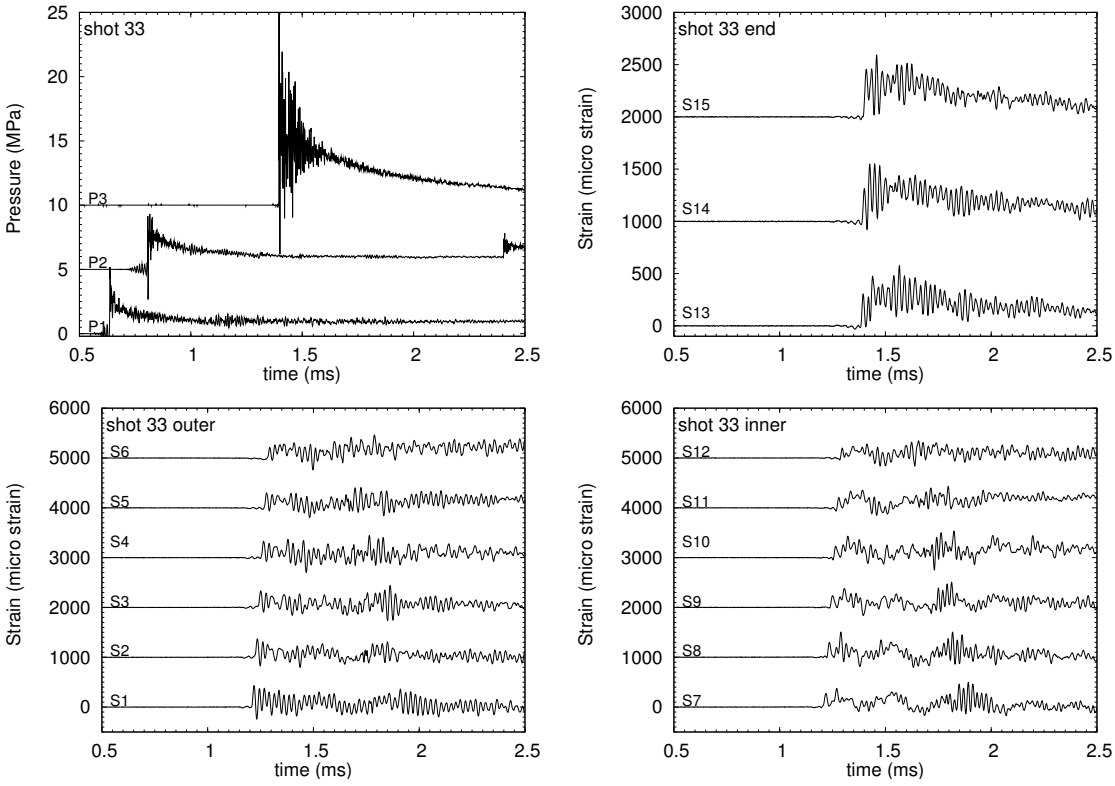

Figure 86: Pressure and strain traces, shot 33, bend specimen, $P_0 = 1$ bar

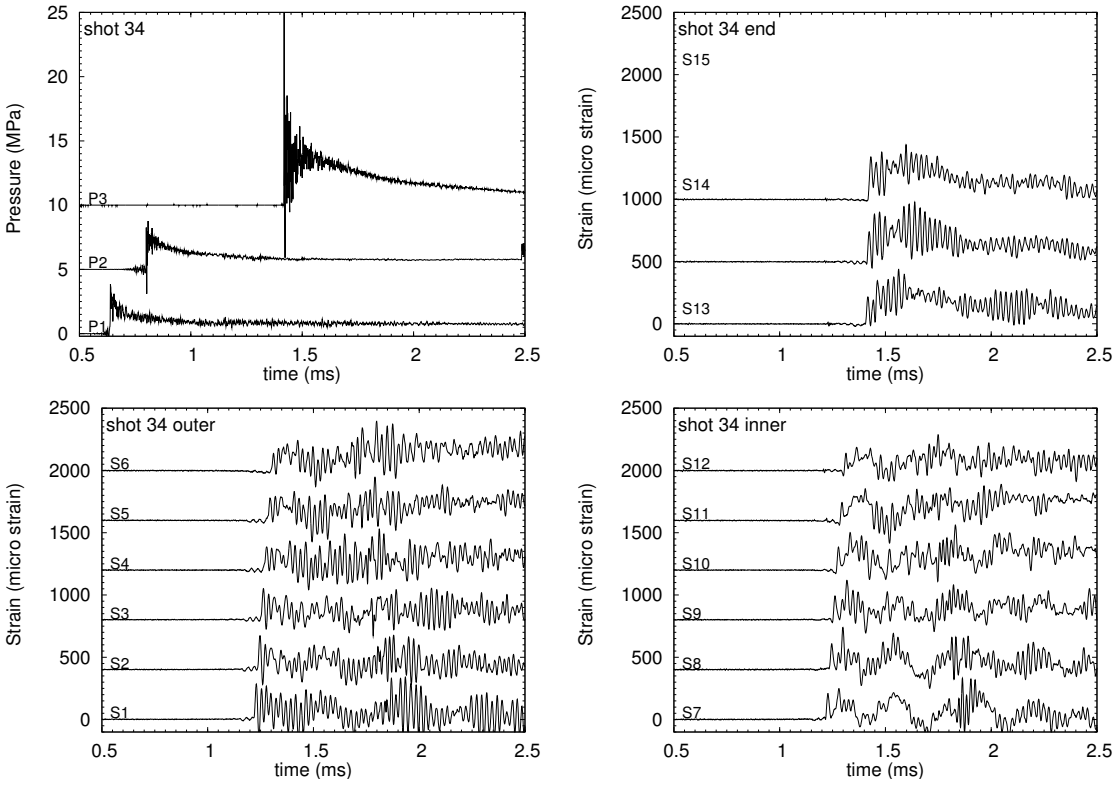

Figure 87: Pressure and strain traces, shot 34, bend specimen, $P_0 = 0.8$ bar

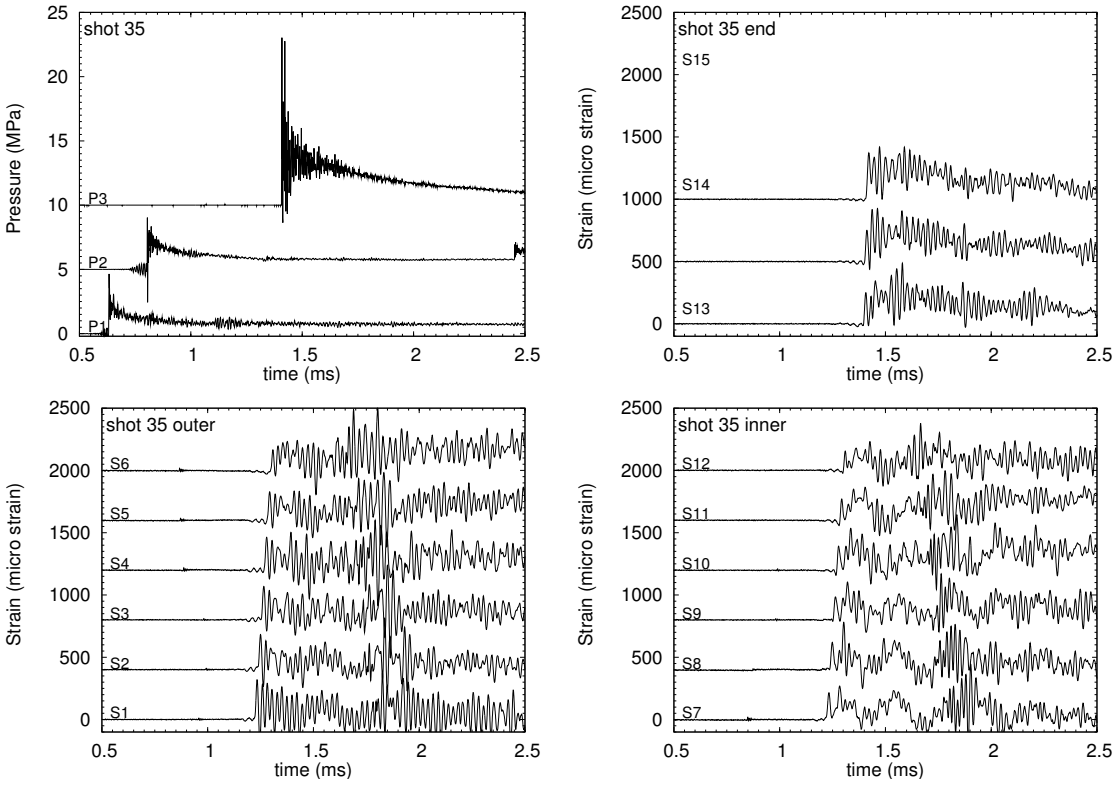

Figure 88: Pressure and strain traces, shot 35, bend specimen, $P_0 = 0.8$ bar

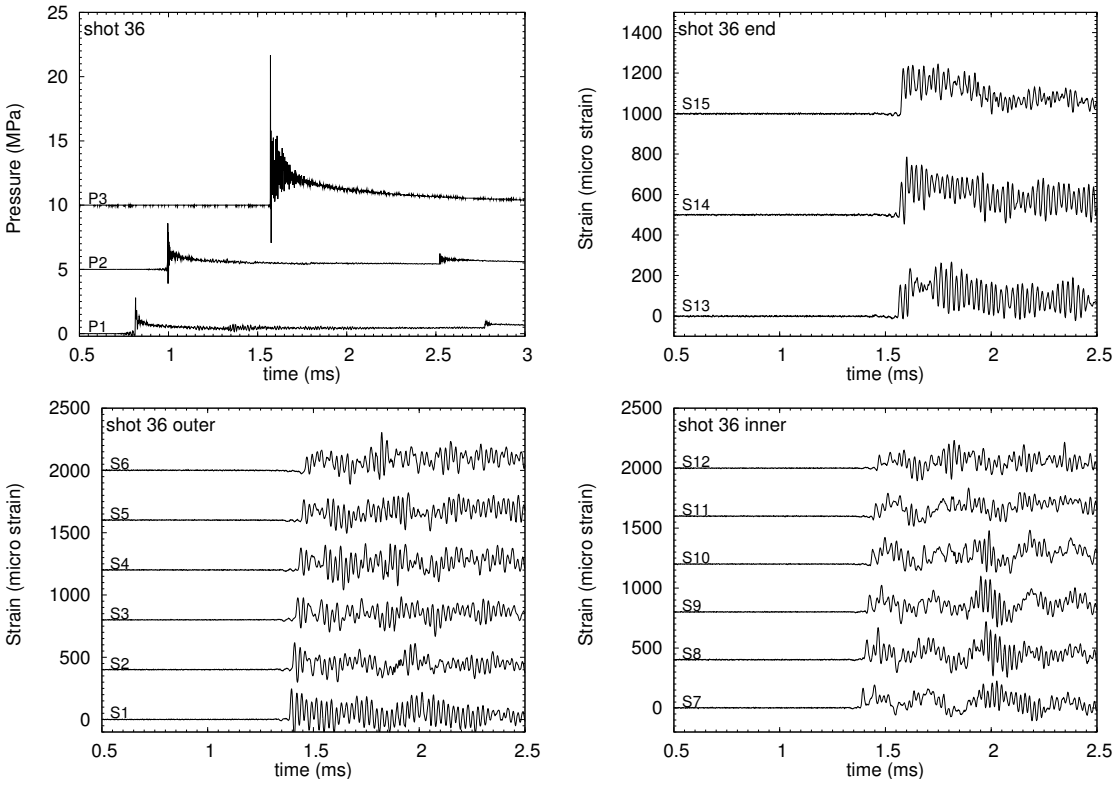

Figure 89: Pressure and strain traces, shot 36, bend specimen, $P_0 = 0.5$ bar

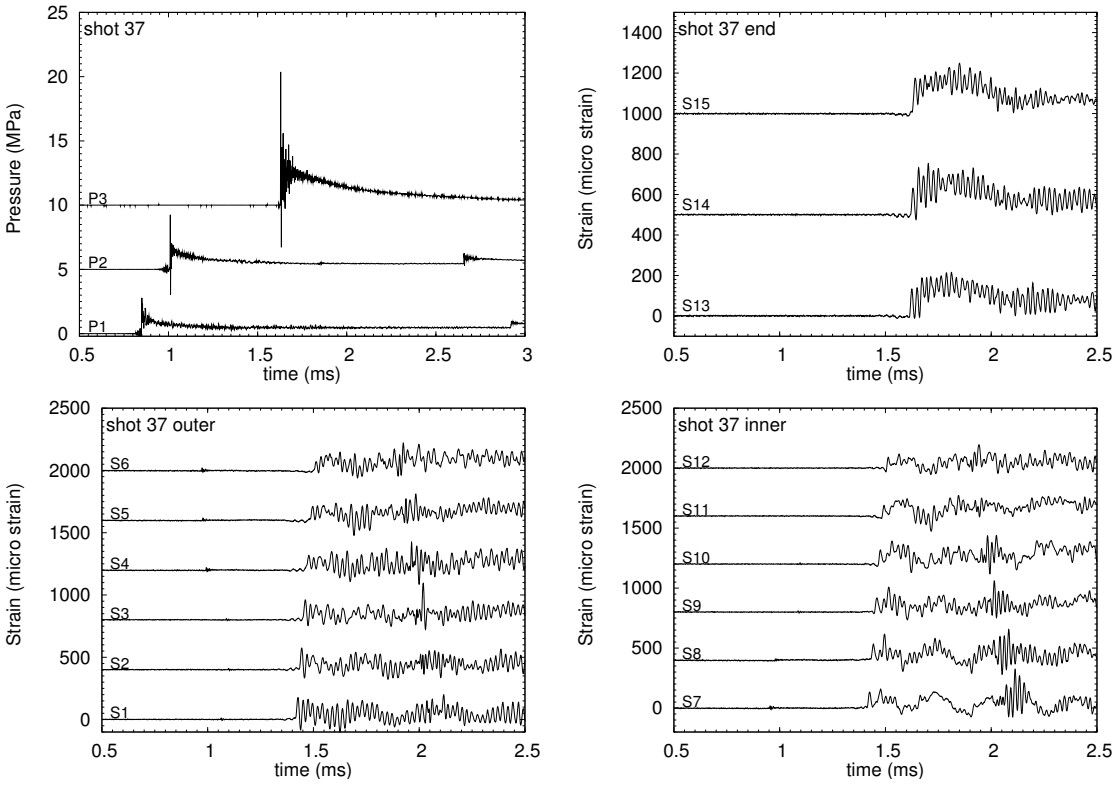

Figure 90: Pressure and strain traces, shot 37, bend specimen, $P_0 = 0.5$ bar

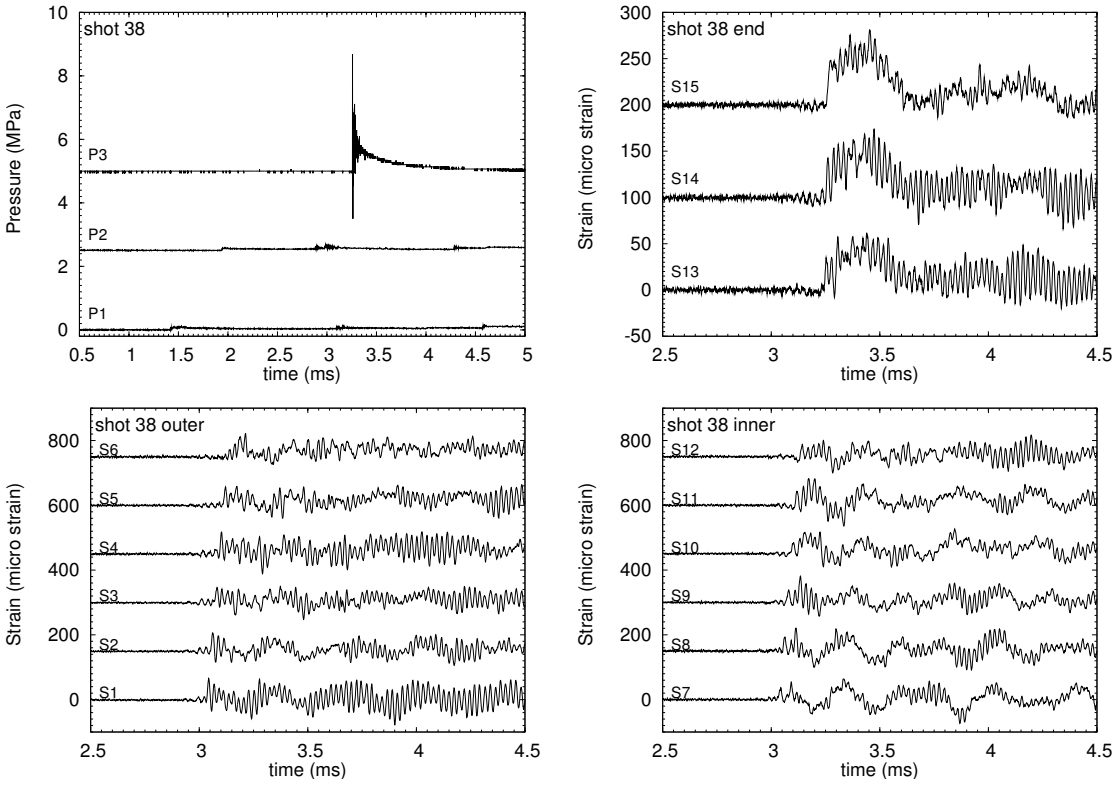

Figure 91: Pressure and strain traces, shot 38, bend specimen, $P_0 = 0.1$ bar

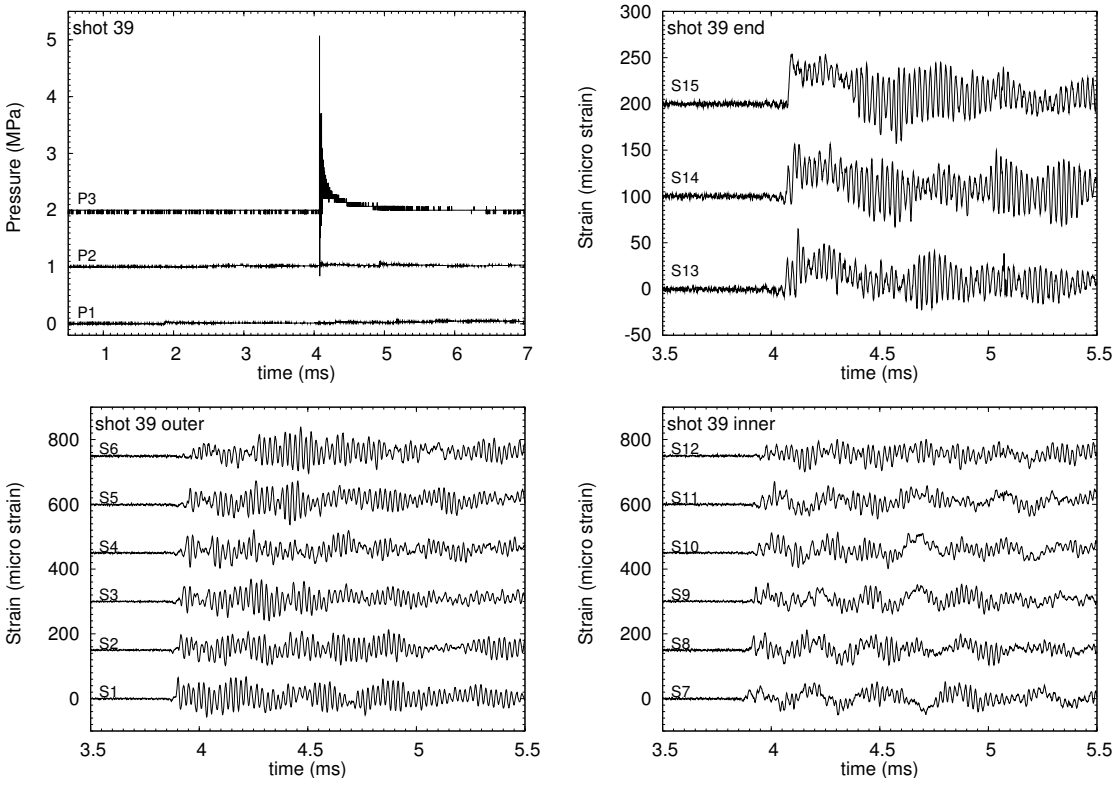

Figure 92: Pressure and strain traces, shot 39, bend specimen, $P_0 = 0.05$ bar

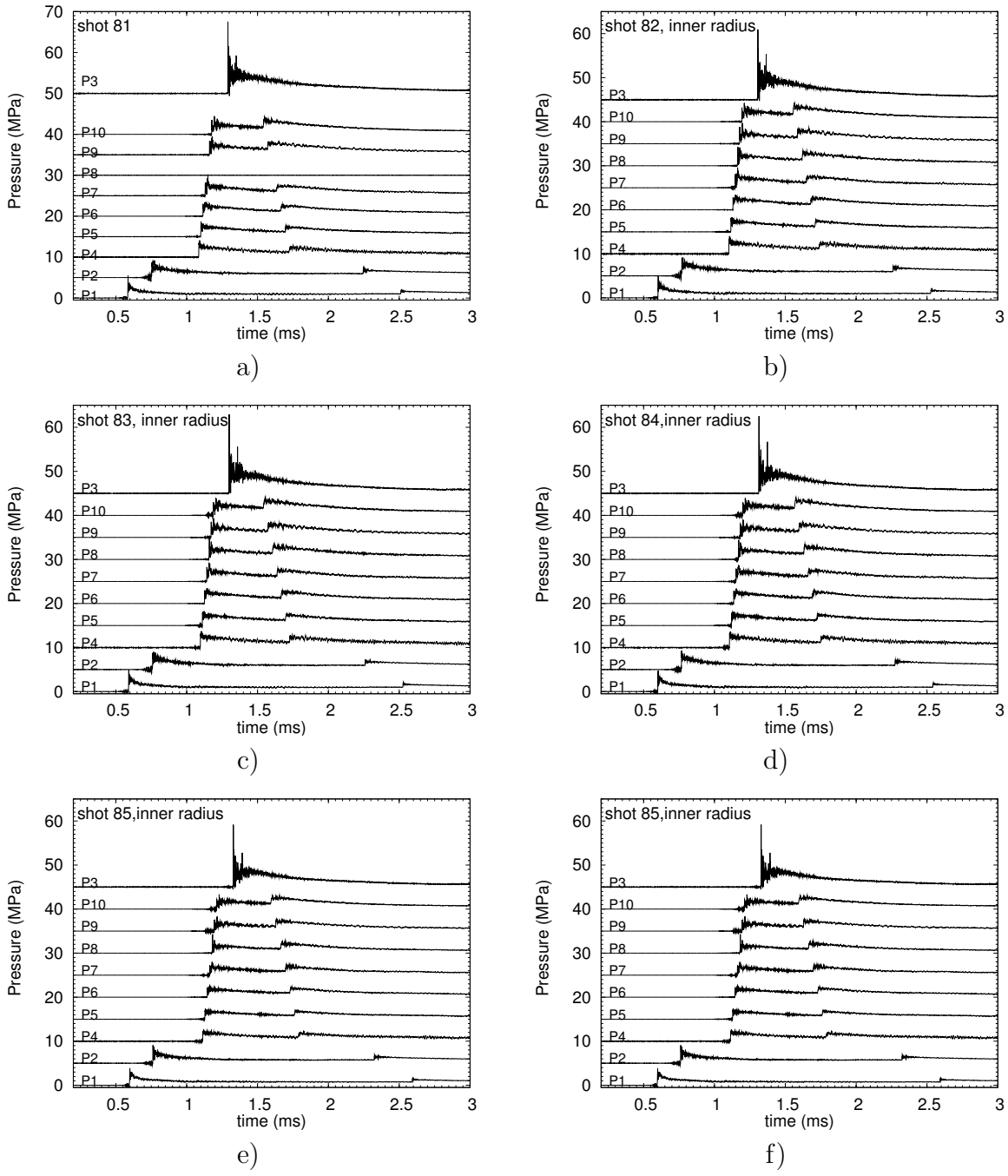

Figure 93: Pressure traces for the bend specimen: (a) shot 81, (b) shot 82, (c) shot 83 and (d) shot 84 for $P_0 = 1$ bar, (e) shot 85 and (f) shot 86 for $P_0 = 0.8$ bar. Test series B-2.

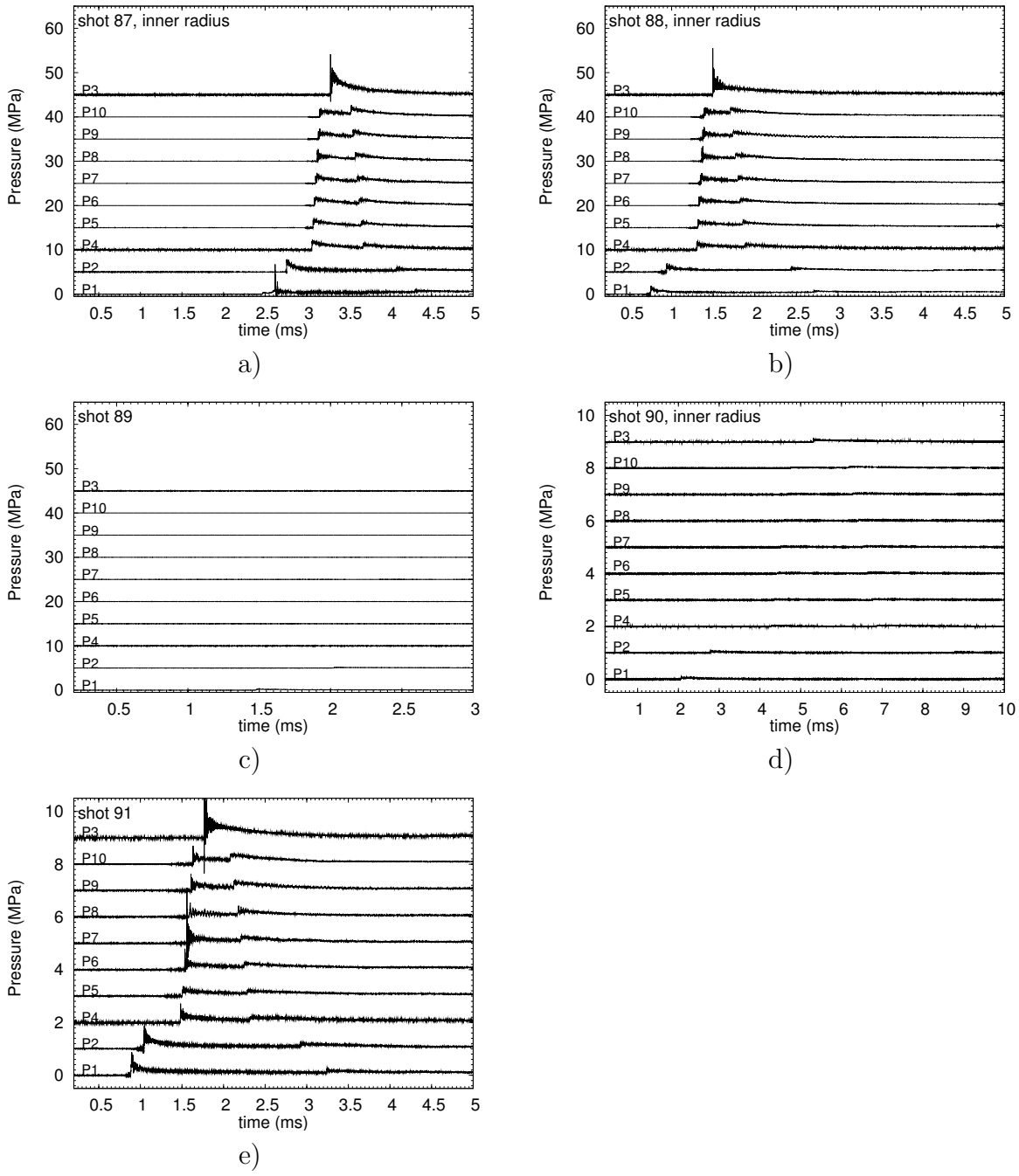

Figure 94: Pressure traces for the bend specimen: (a) shot 87 and (b) shot 88 for $P_0 = 0.5$ bar, (c) shot 89 for $P_0 = 0.3$ bar, (d) shot 90 for $P_0 = 0.2$ bar, (e) shot 91 for $P_0 = 0.15$ bar. Test series B-2.

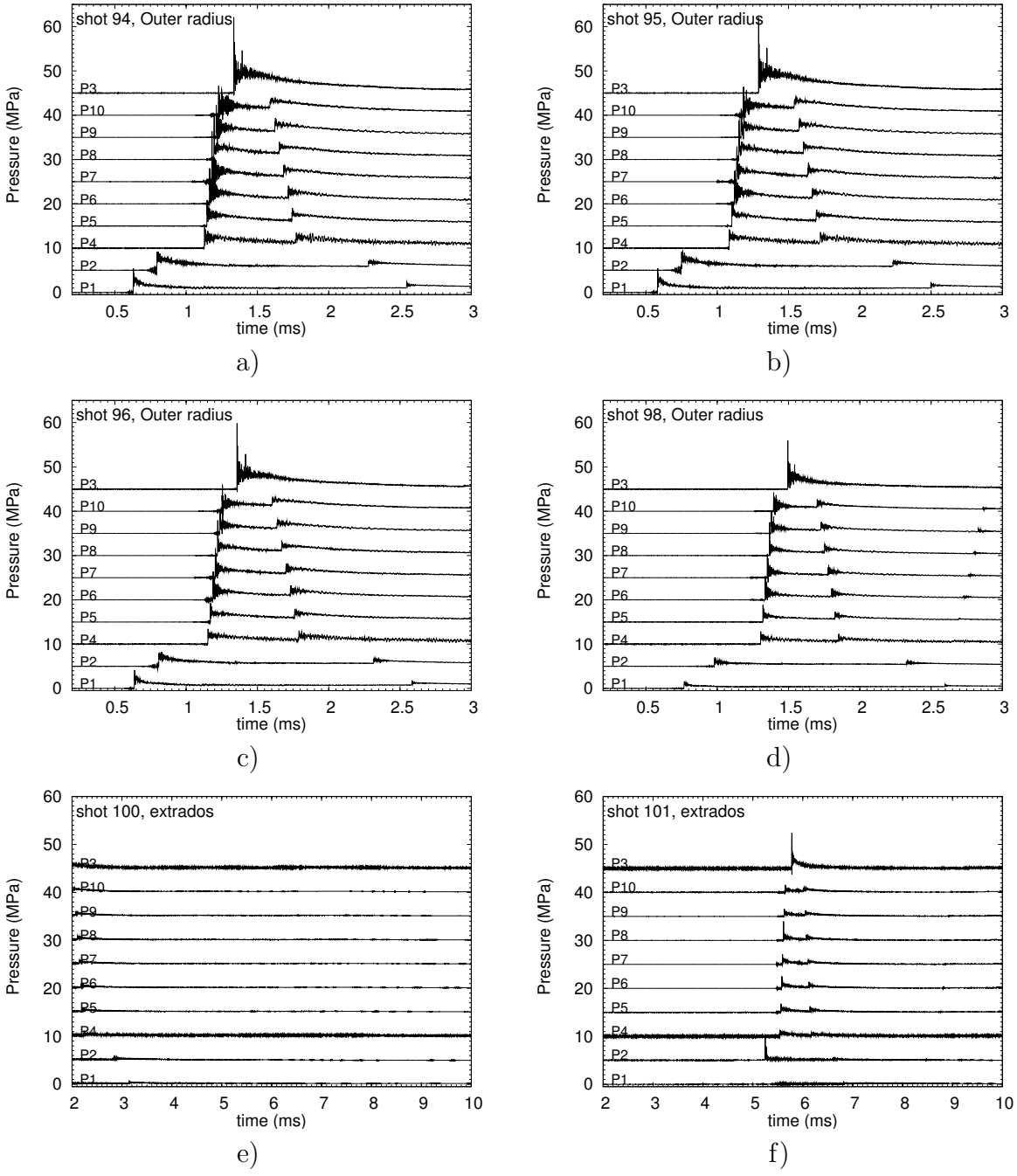

Figure 95: Pressure traces for the bend specimen: (a) shot 94 and (b) shot 95 for $P_0 = 1$ bar, (c) shot 96 for $P_0 = 0.8$ bar, (d) shot 98 for $P_0 = 0.5$ bar, (e) shot 100 for $P_0 = 0.3$ bar and (f) shot 101 for $P_0 = 0.2$ bar. Test series B-3.

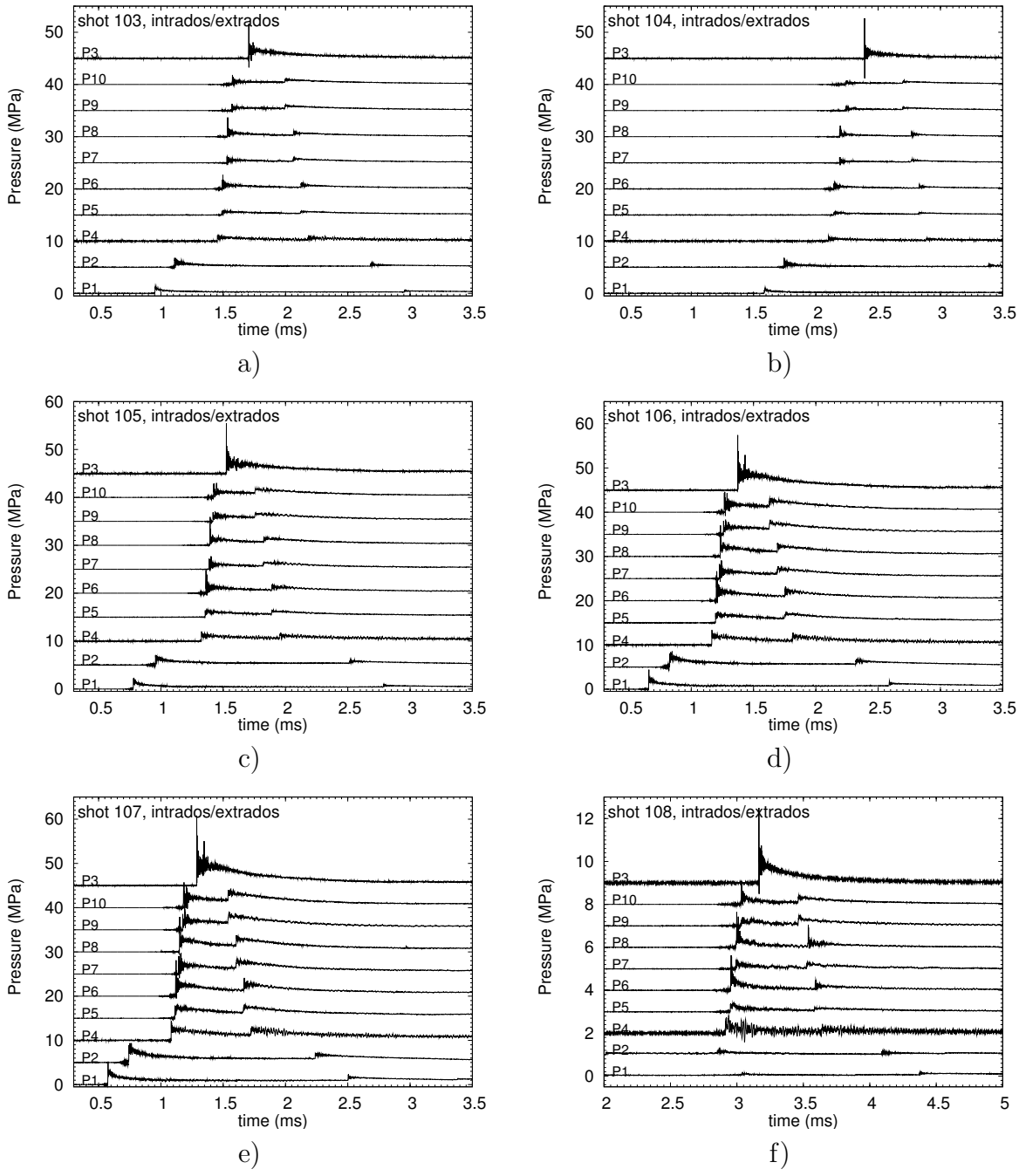

Figure 96: Pressure traces for the bend specimen: (a) shot 103 for $P_0 = 0.3$ bar, (b) shot 104 for $P_0 = 0.2$ bar, (c) shot 105 for $P_0 = 0.5$ bar, (d) shot 106 for $P_0 = 0.8$ bar, (e) shot 107 for $P_0 = 1$ bar and (f) shot 108 for $P_0 = 0.1$ bar. Test series B-4.

I Plots - Tee specimens

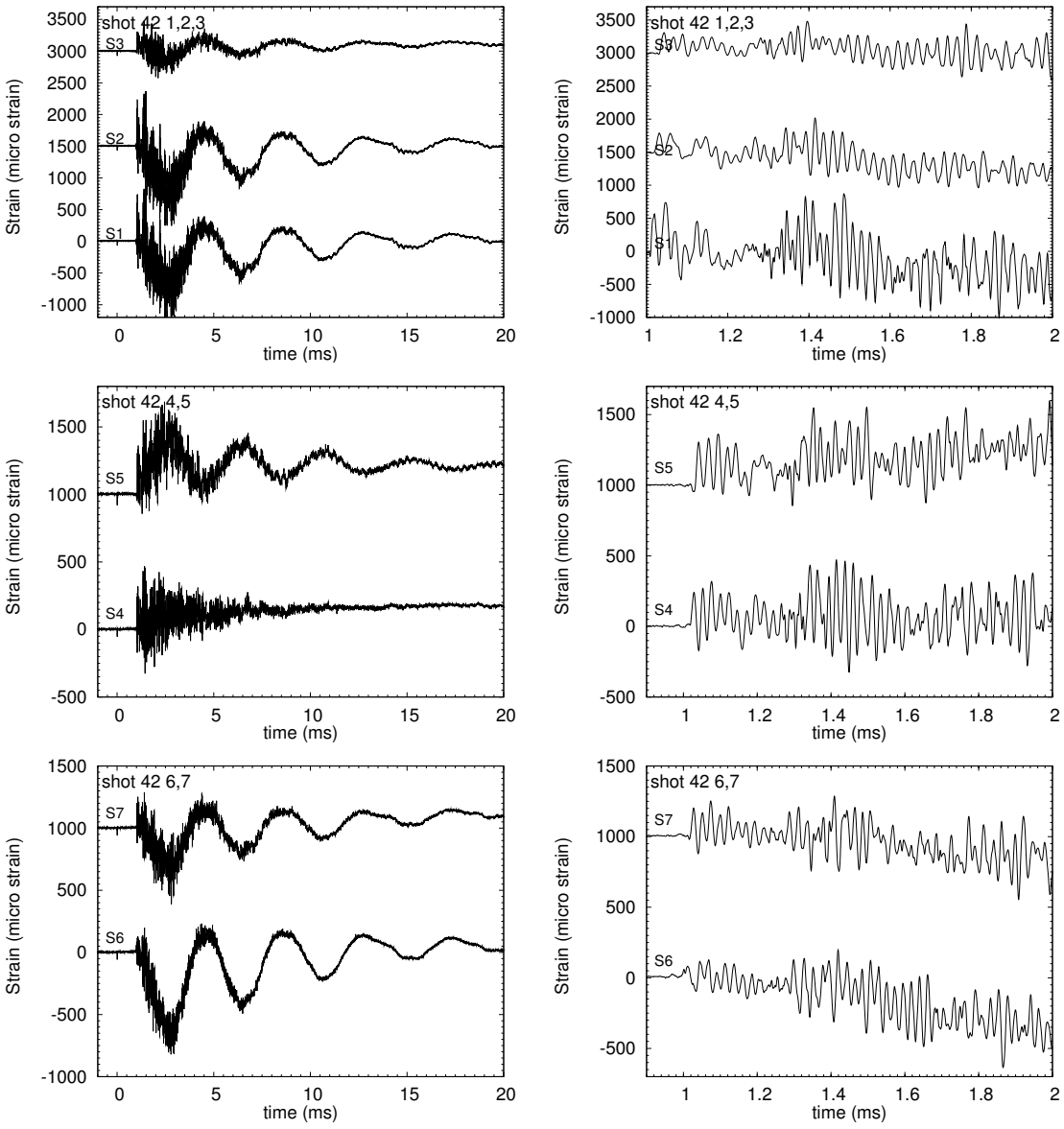

Figure 97: Strain traces, shot 42, tee specimen, $P_0 = 1$ bar

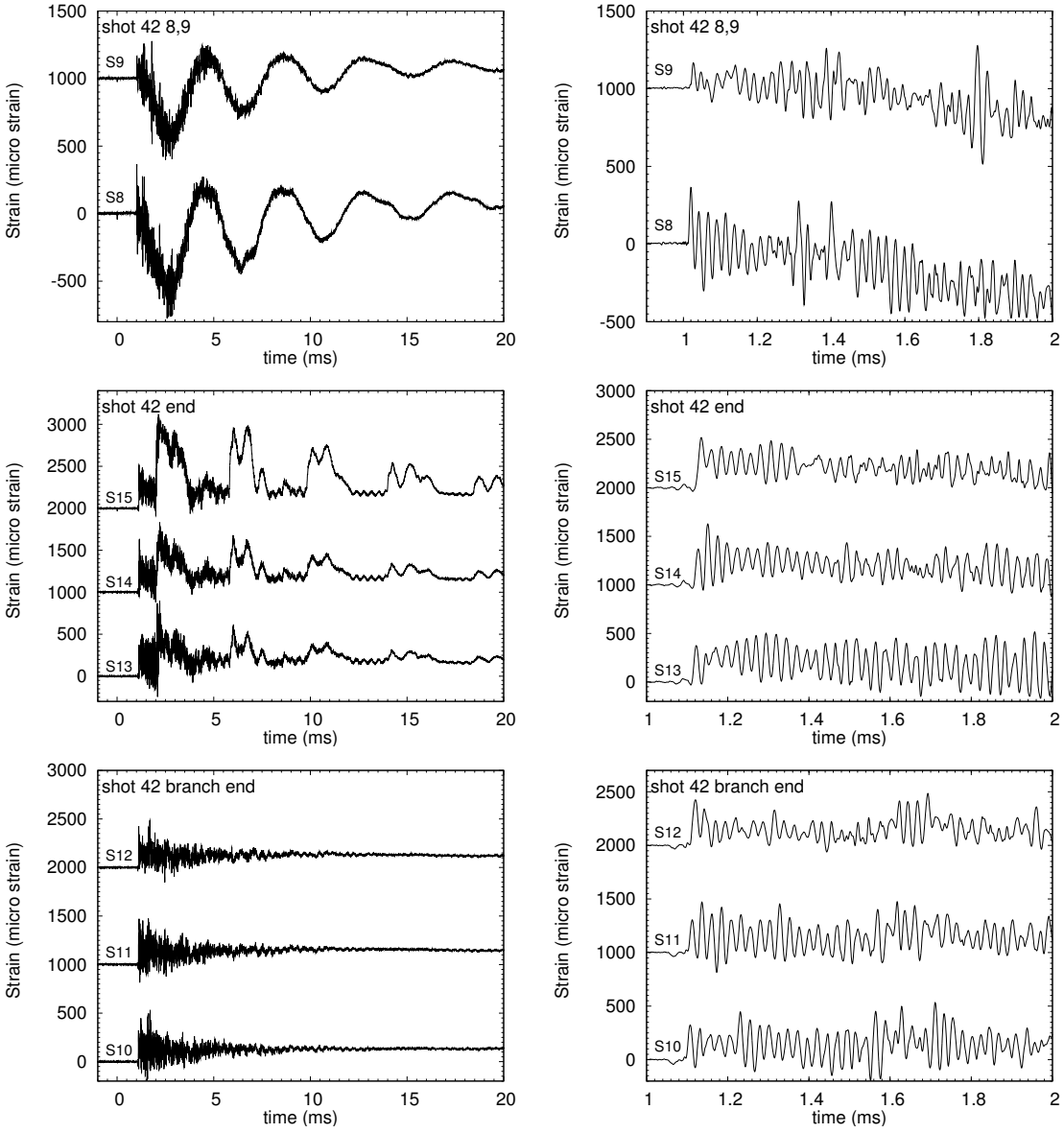

Figure 98: Strain traces, shot 42, tee specimen, $P_0 = 1$ bar

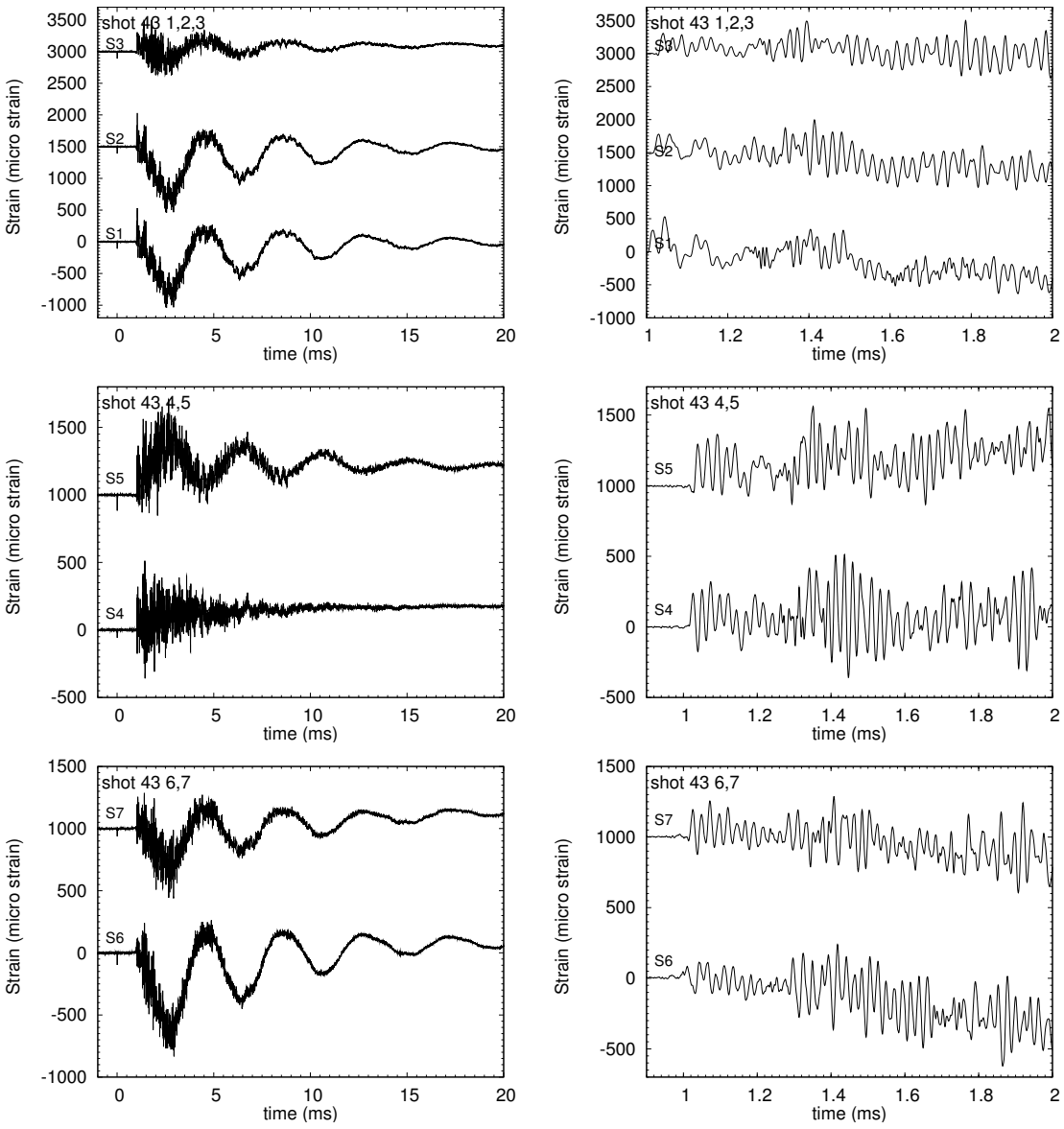

Figure 99: Strain traces, shot 43, tee specimen, $P_0 = 1$ bar

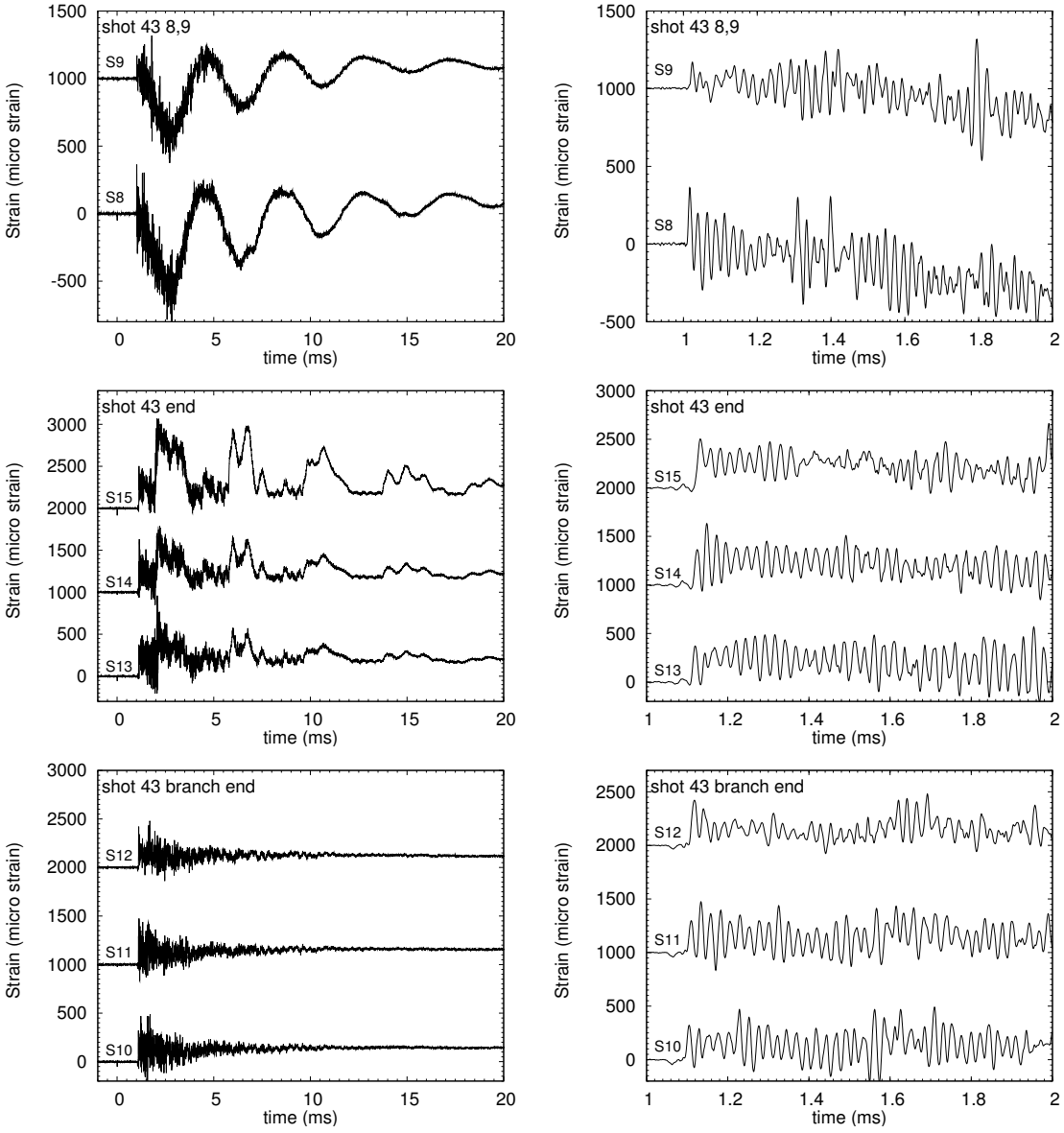

Figure 100: Strain traces, shot 43, tee specimen, $P_0 = 1$ bar

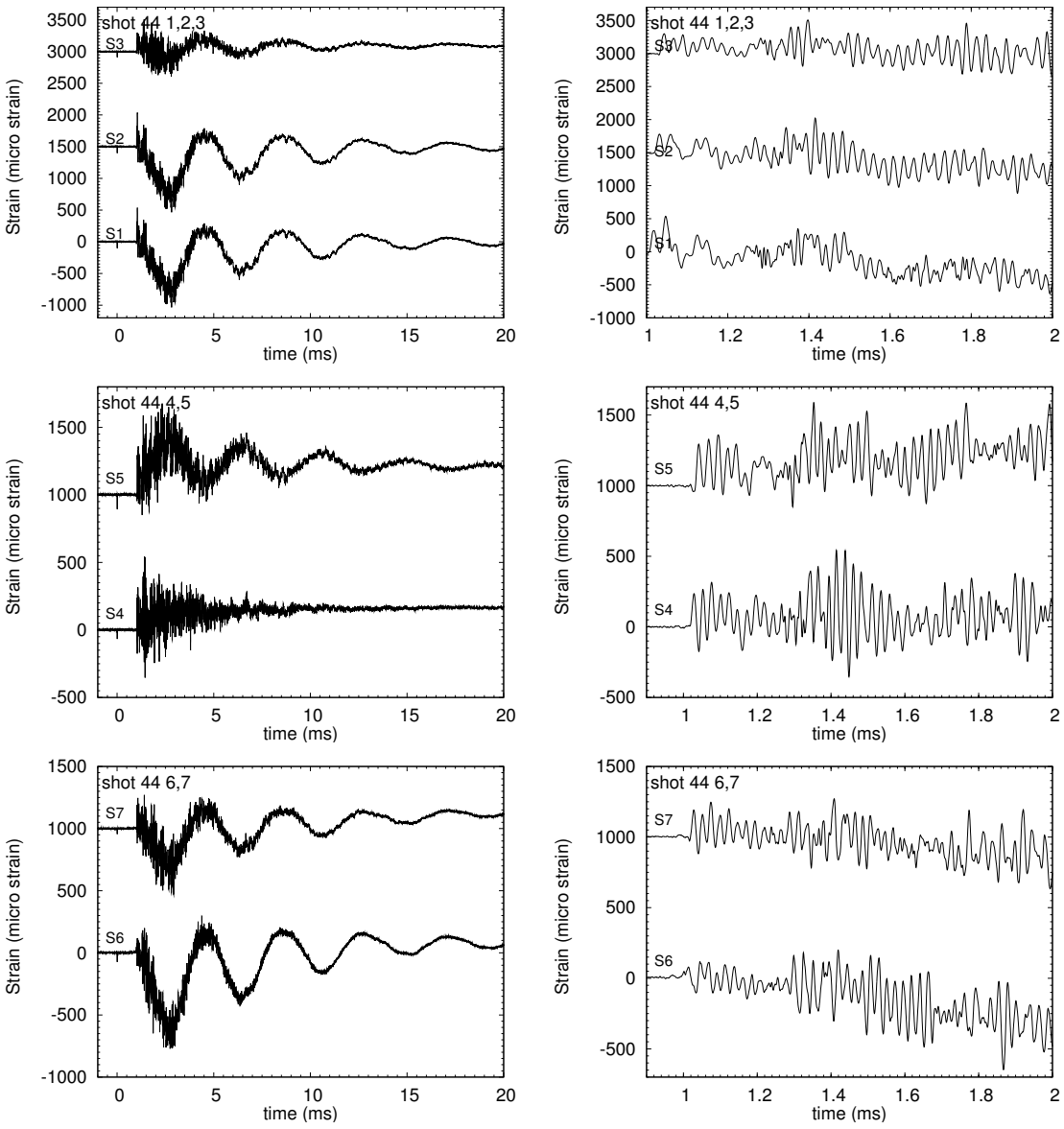

Figure 101: Strain traces, shot 44, tee specimen, $P_0 = 1$ bar

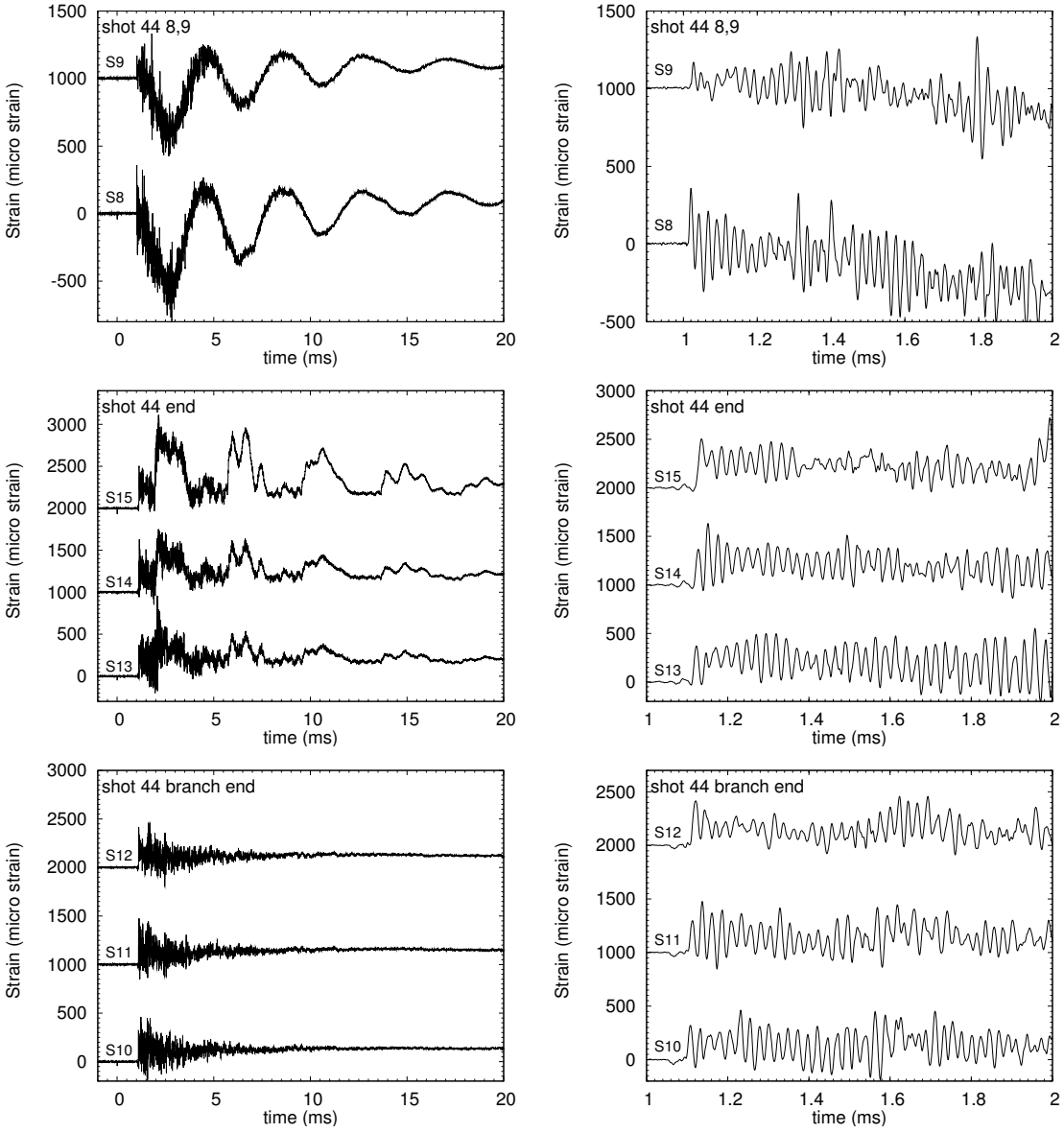

Figure 102: Strain traces, shot 44, tee specimen, $P_0 = 1$ bar

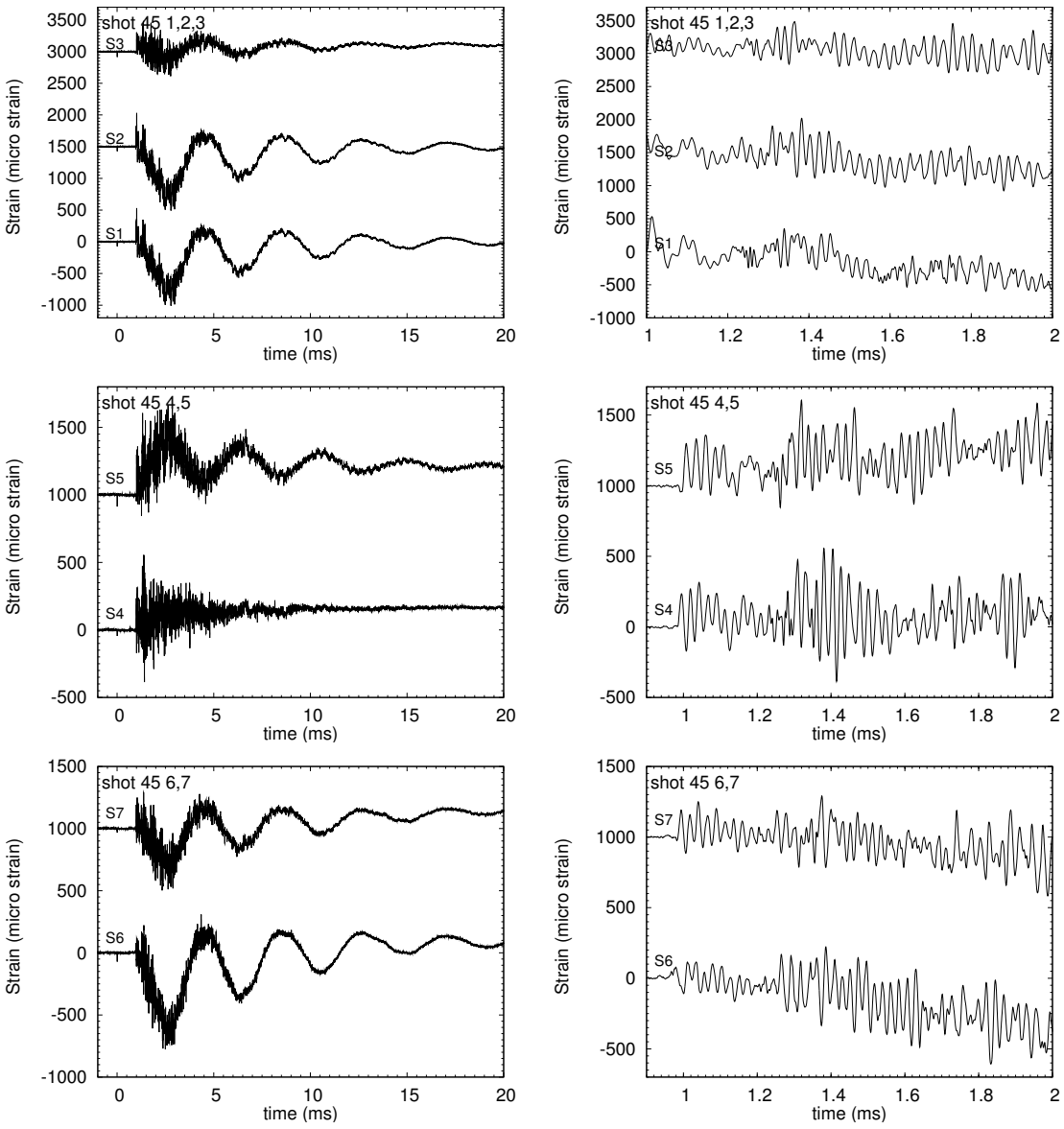

Figure 103: Strain traces, shot 45, tee specimen, $P_0 = 1$ bar

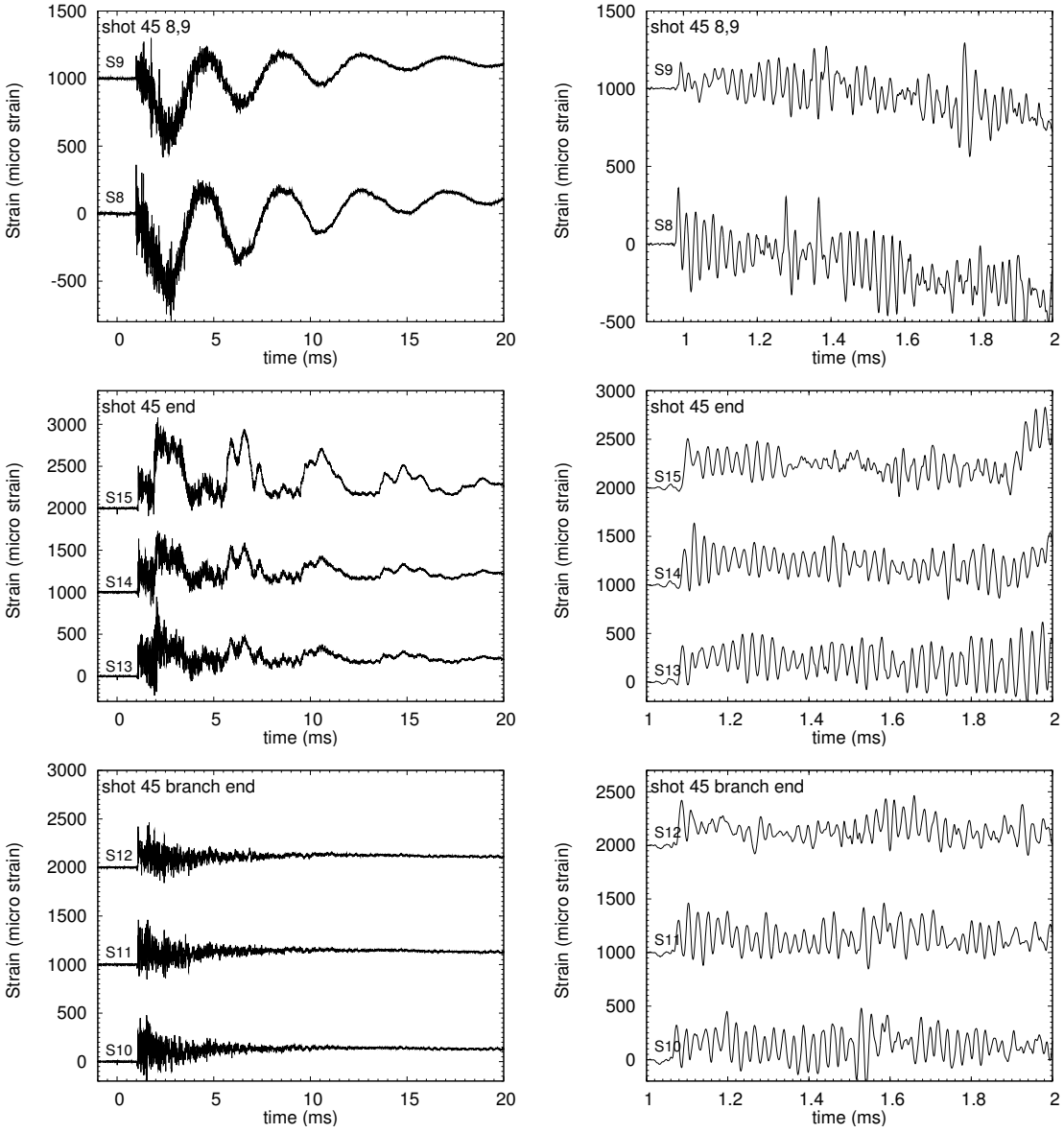

Figure 104: Strain traces, shot 45, tee specimen, $P_0 = 1$ bar

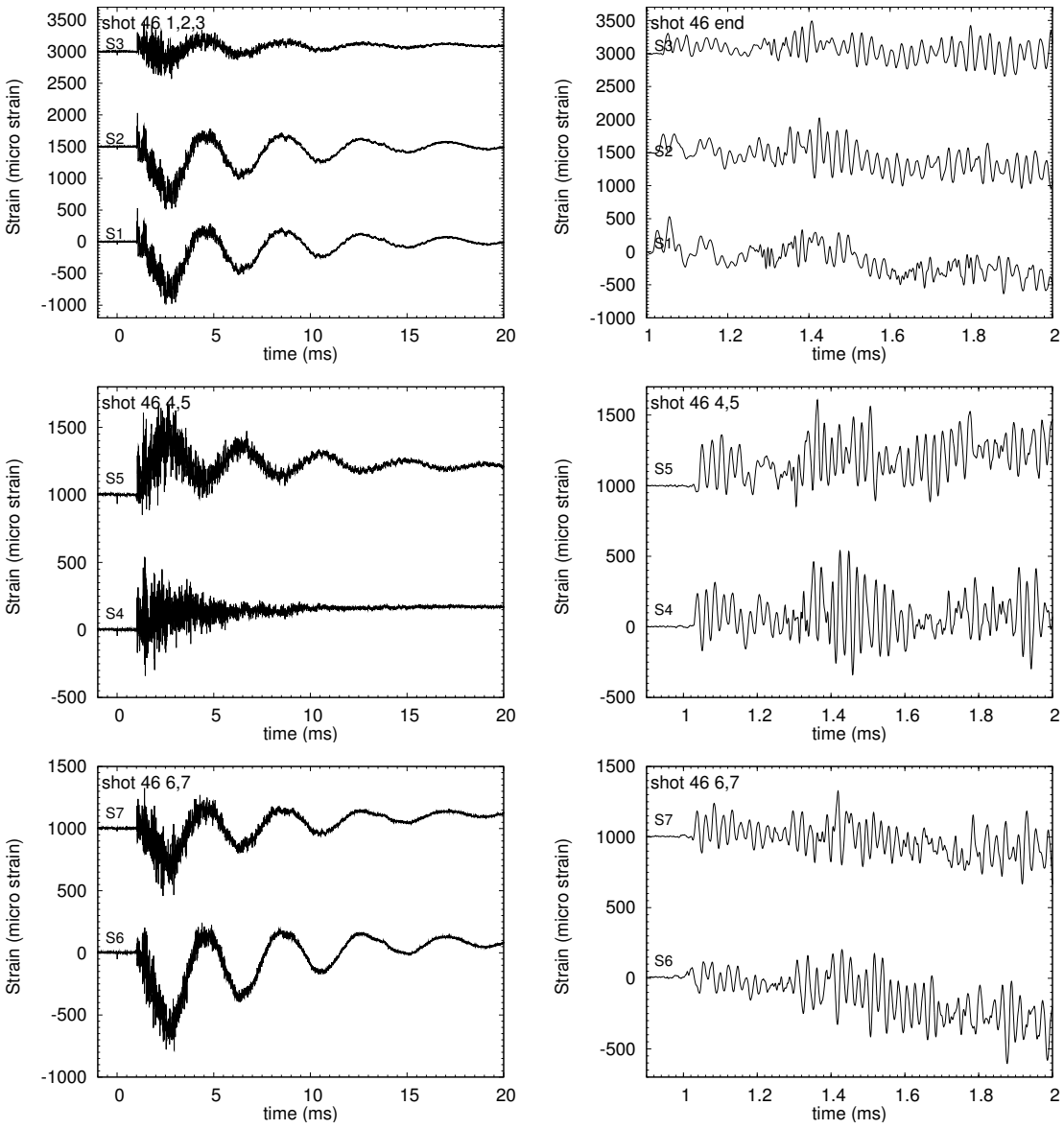

Figure 105: Strain traces, shot 46, tee specimen, $P_0 = 1$ bar

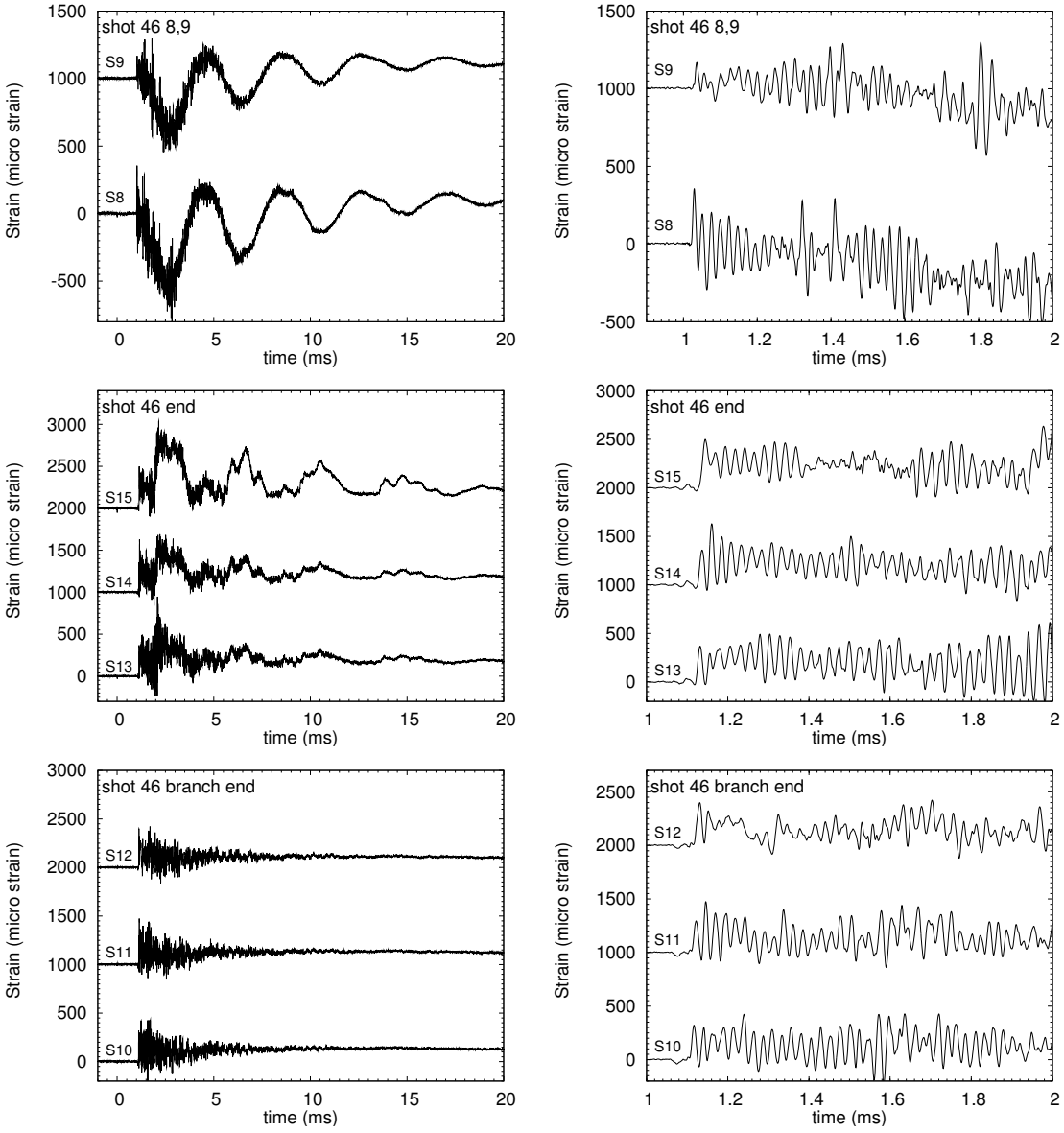

Figure 106: Strain traces, shot 46, tee specimen, $P_0 = 1$ bar

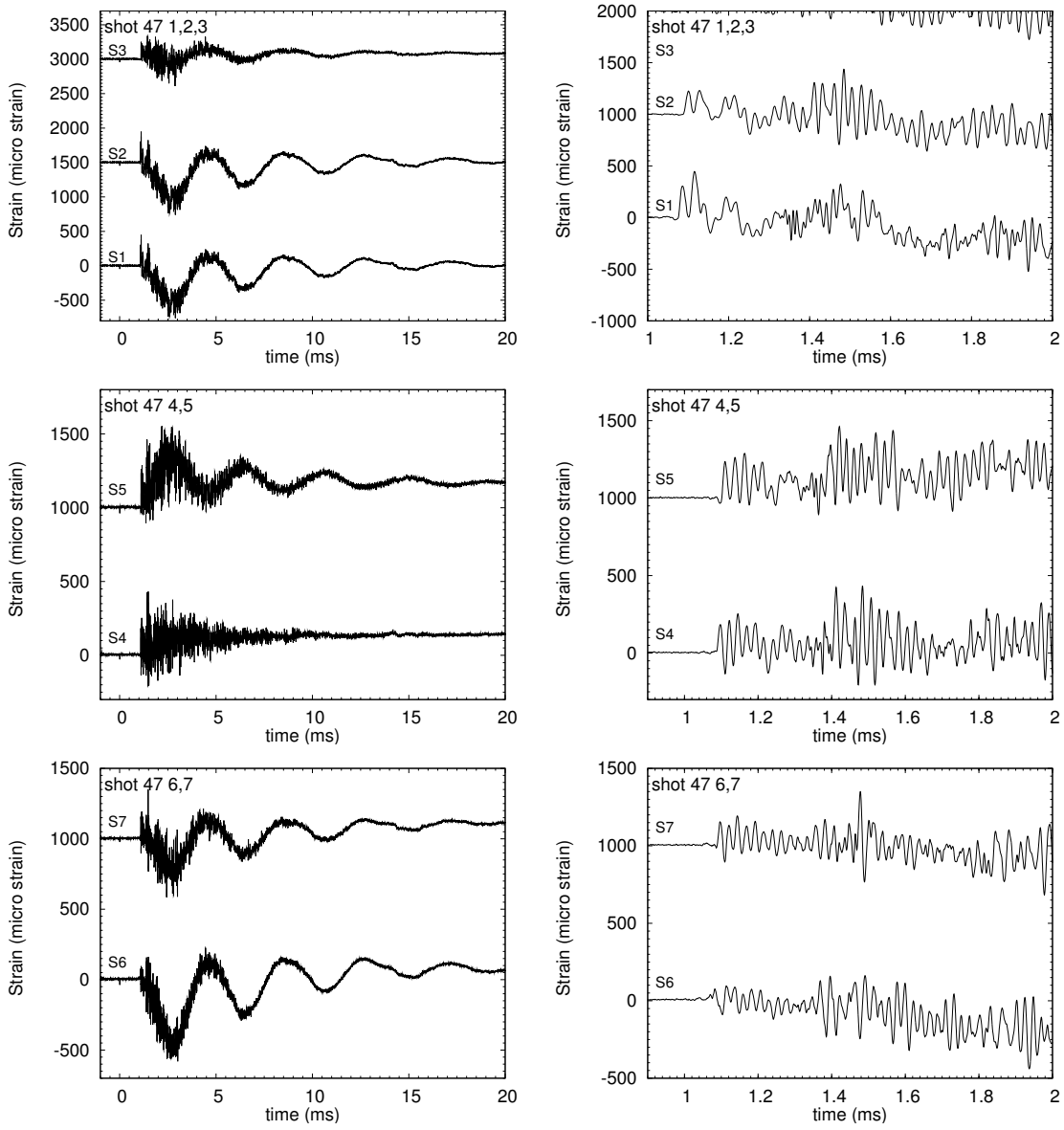

Figure 107: Strain traces, shot 47, tee specimen, $P_0 = 0.81$ bar

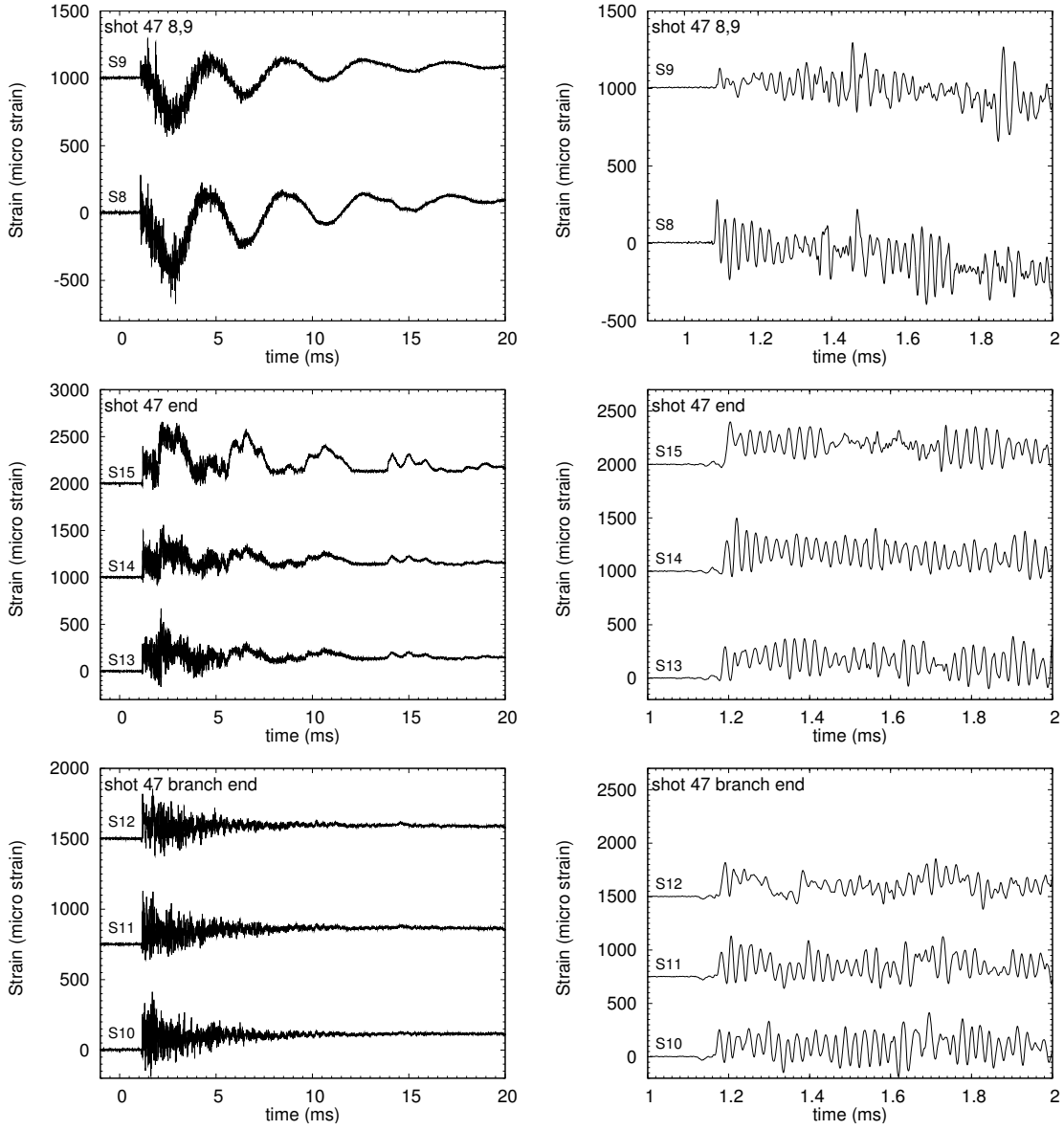

Figure 108: Strain traces, shot 47, tee specimen, $P_0 = 0.8$ bar

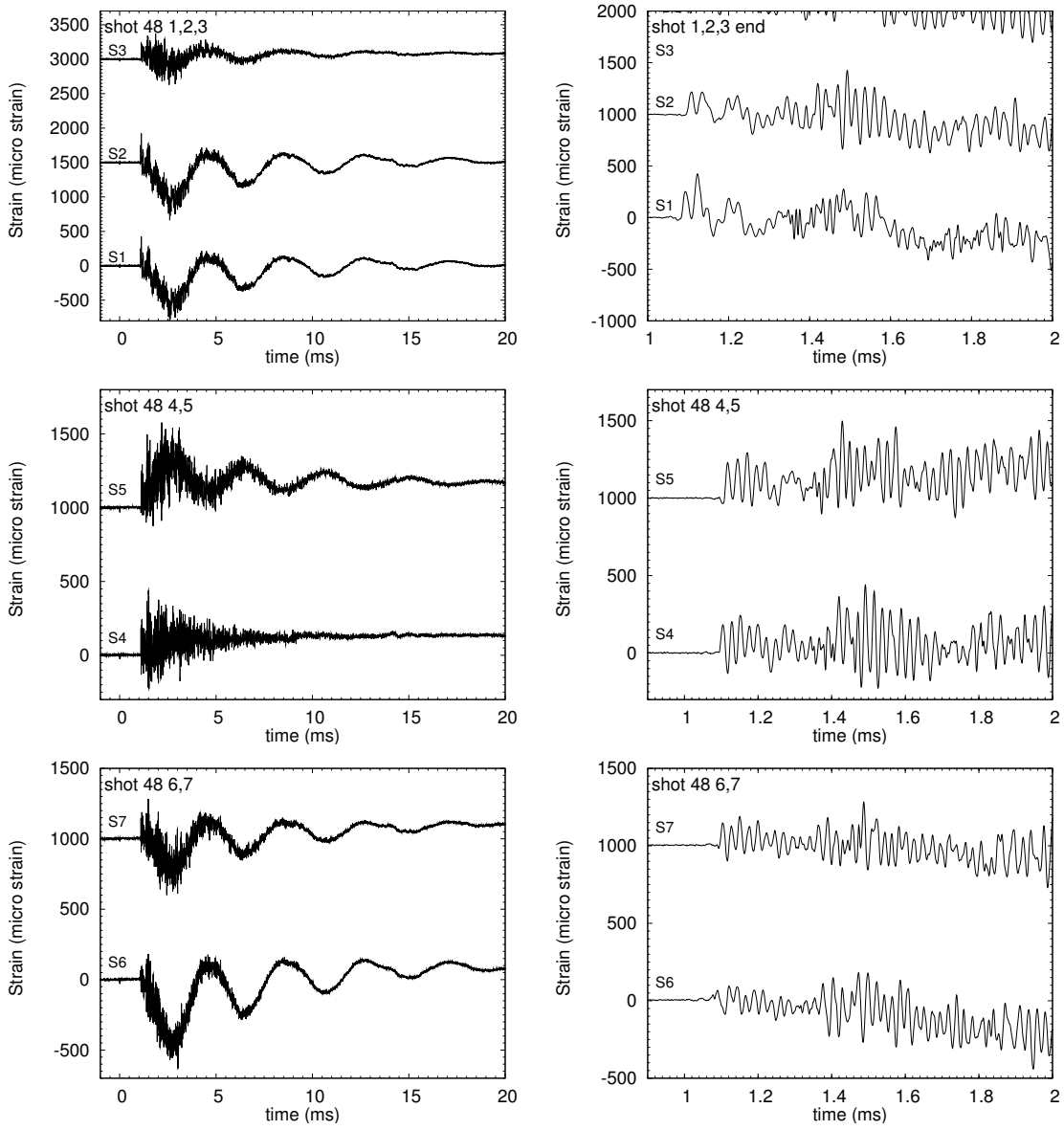

Figure 109: Strain traces, shot 48, tee specimen, $P_0 = 0.8$ bar

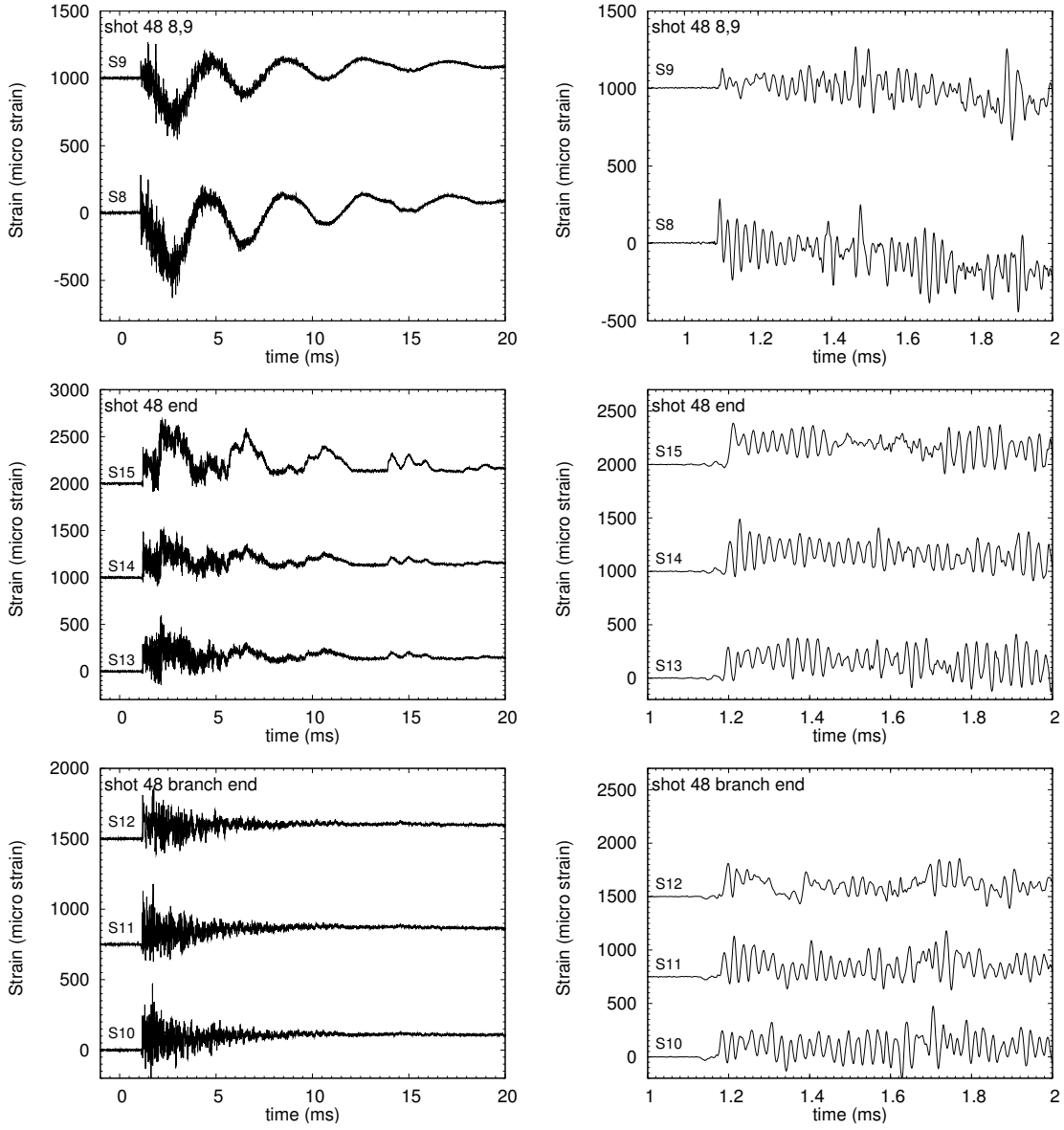

Figure 110: Strain traces, shot 48, tee specimen, $P_0 = 0.8$ bar

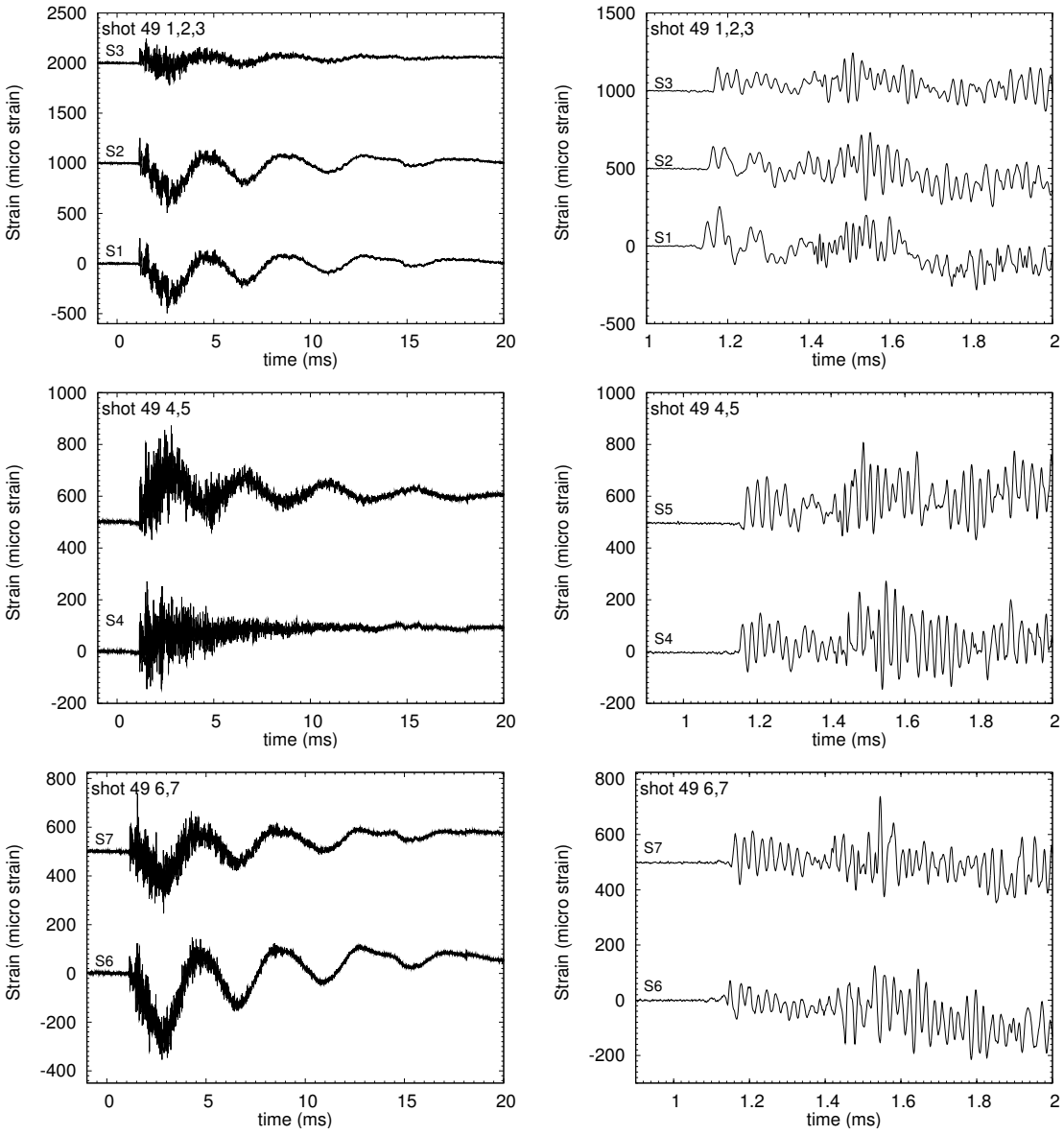

Figure 111: Strain traces, shot 49, tee specimen, $P_0 = 0.5$ bar

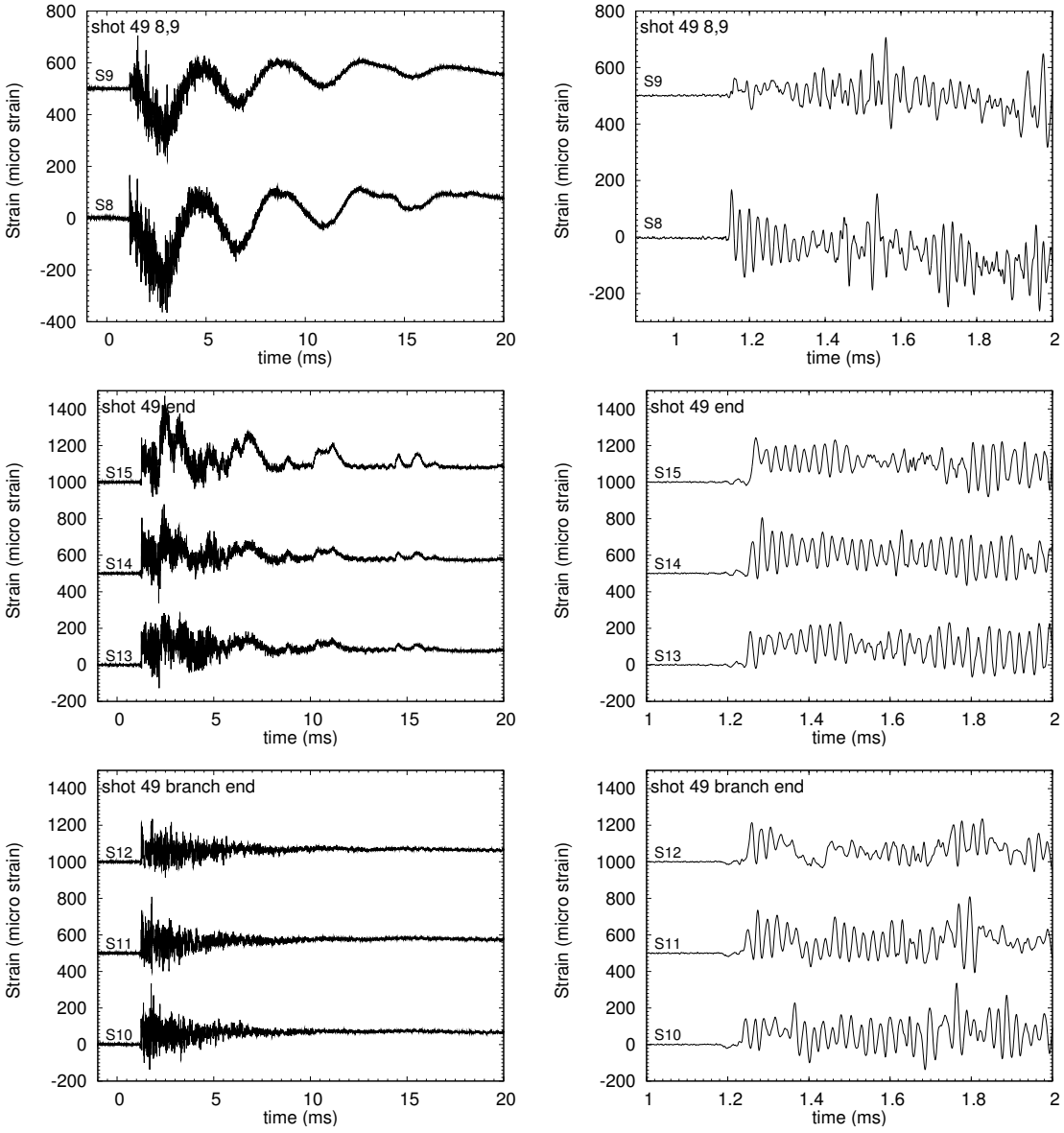

Figure 112: Strain traces, shot 49, tee specimen, $P_0 = 0.5$ bar

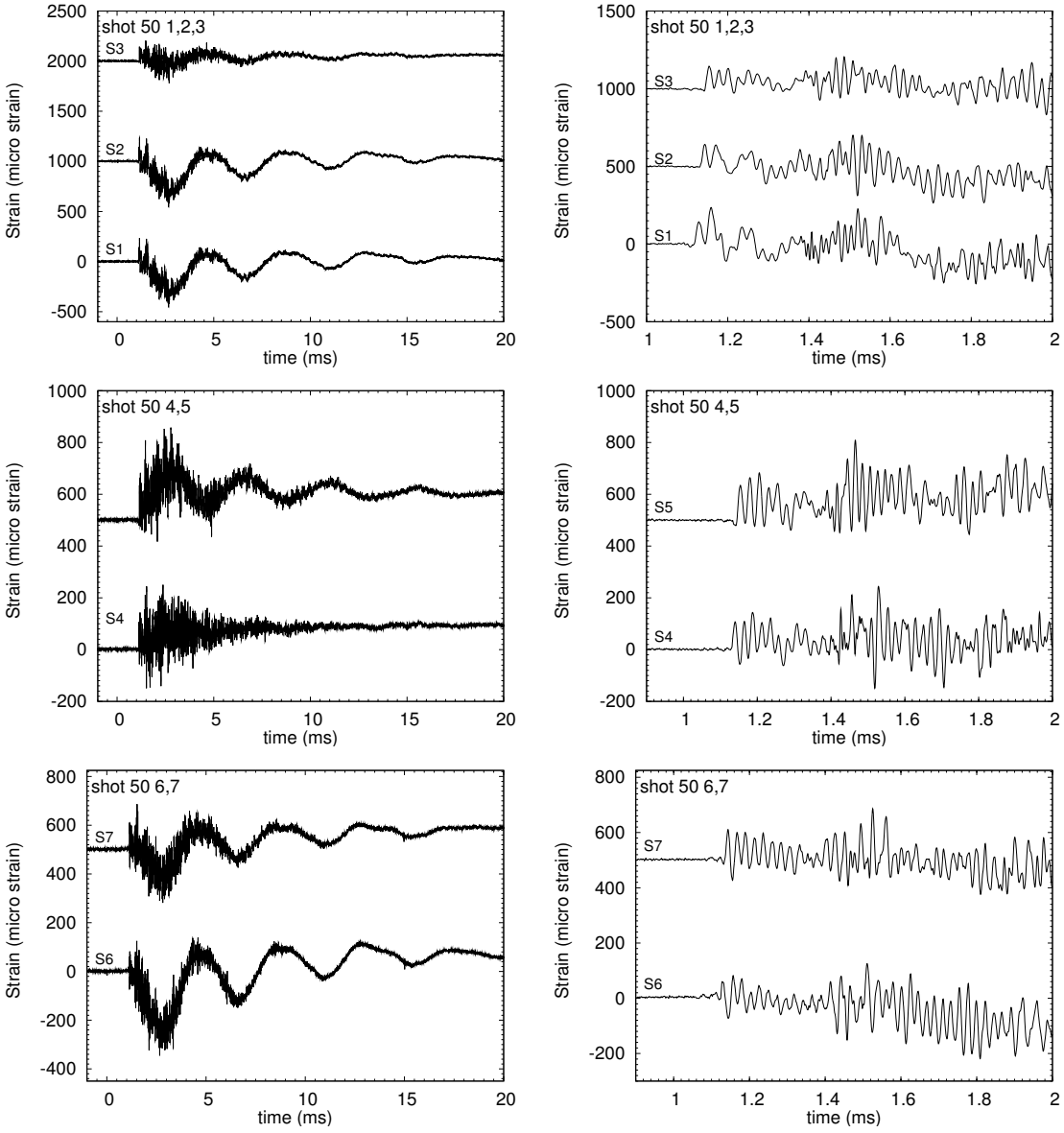

Figure 113: Strain traces, shot 50, tee specimen, $P_0 = 0.5$ bar

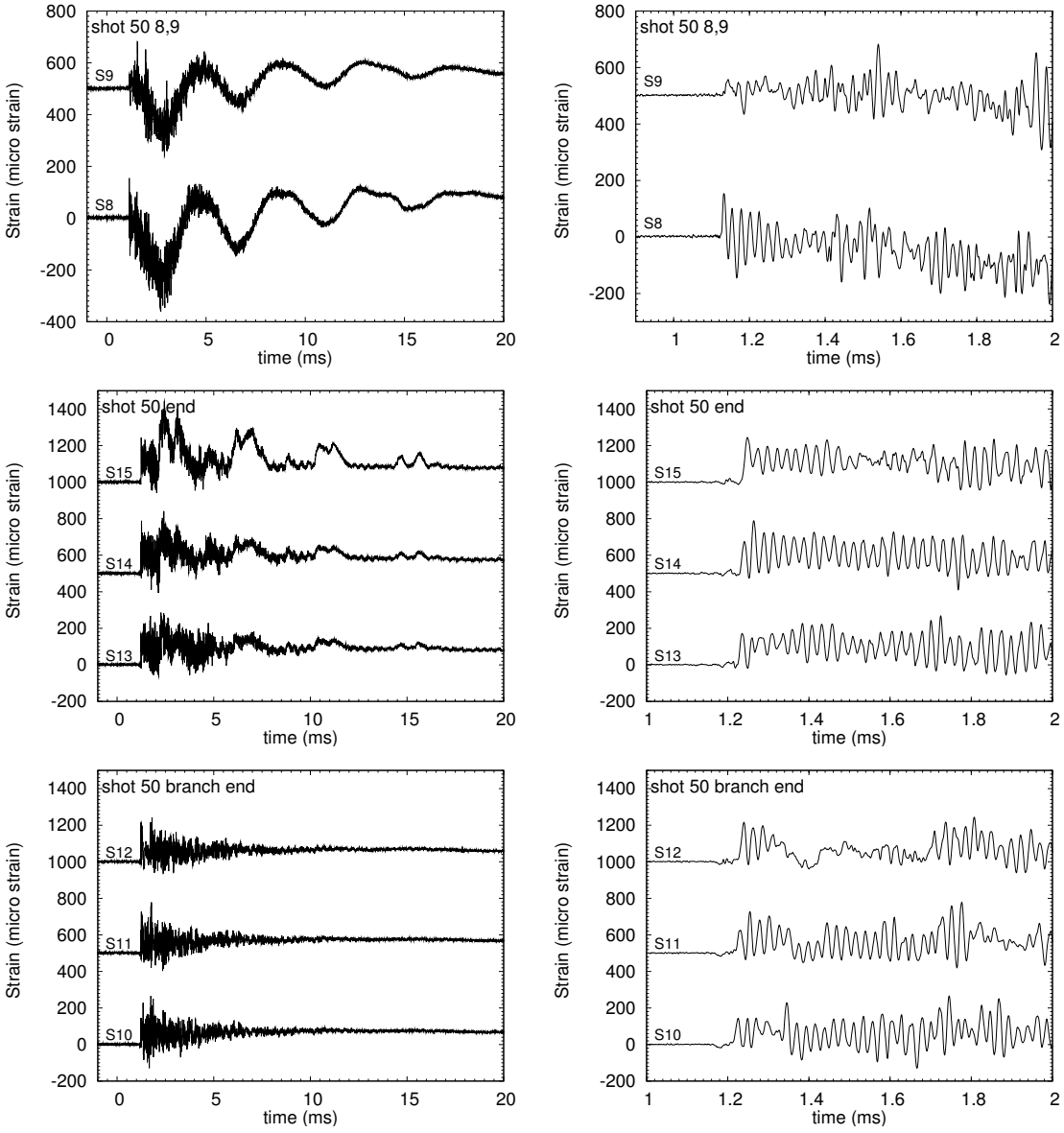

Figure 114: Strain traces, shot 50, tee specimen, $P_0 = 0.5$ bar

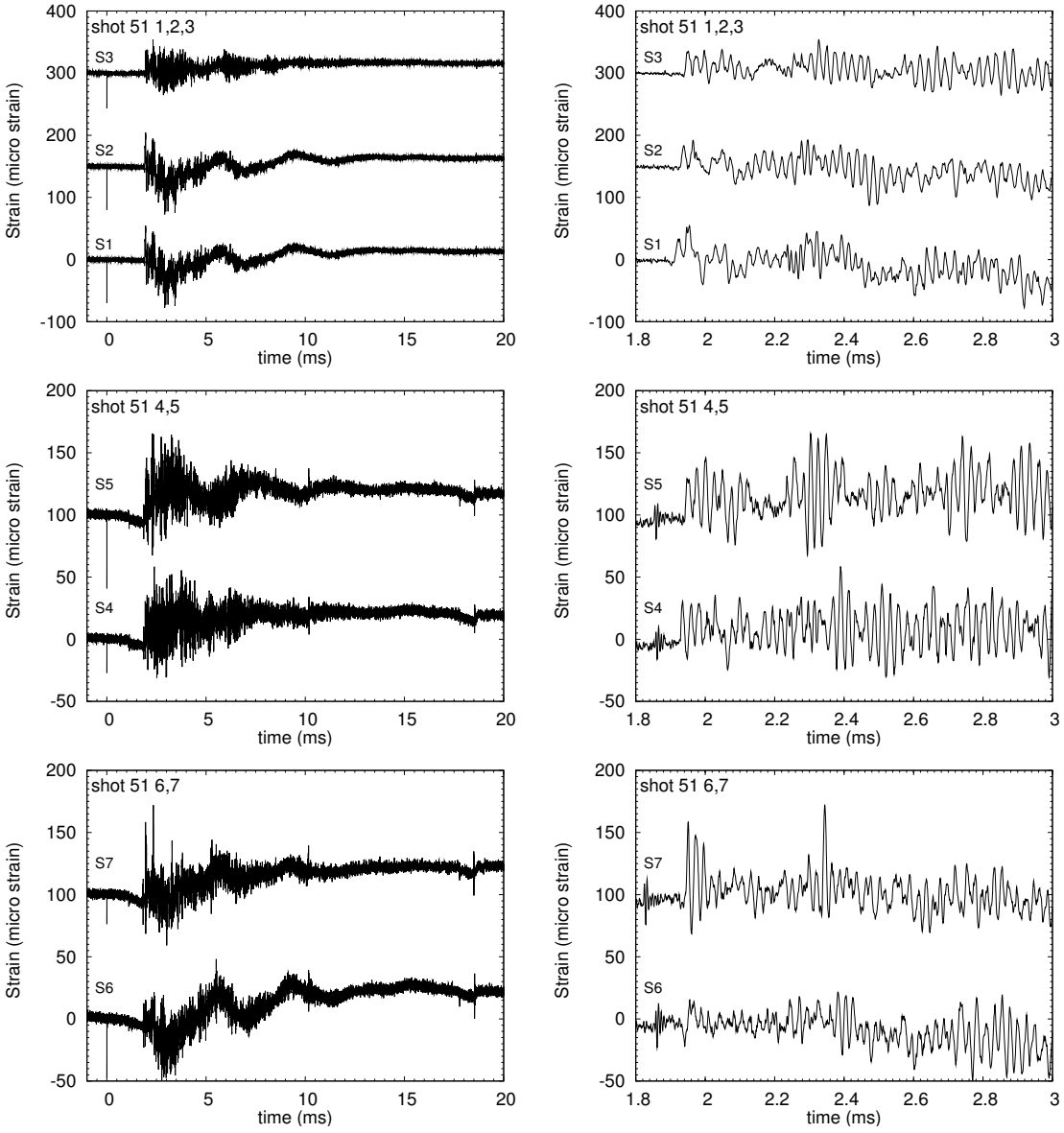

Figure 115: Strain traces, shot 51, tee specimen, $P_0 = 0.1$ bar

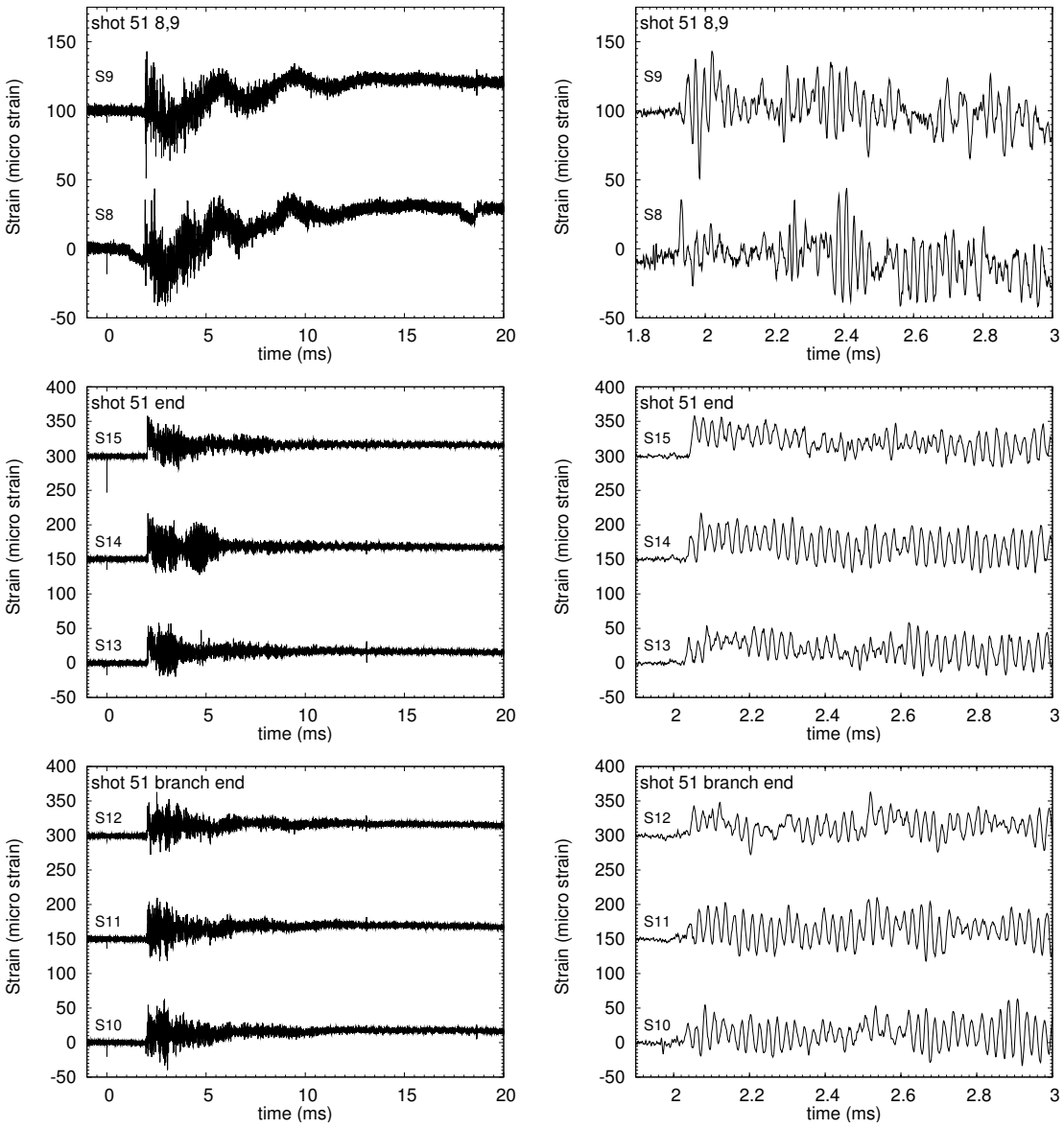

Figure 116: Strain traces, shot 51, tee specimen, $P_0 = 0.1$ bar

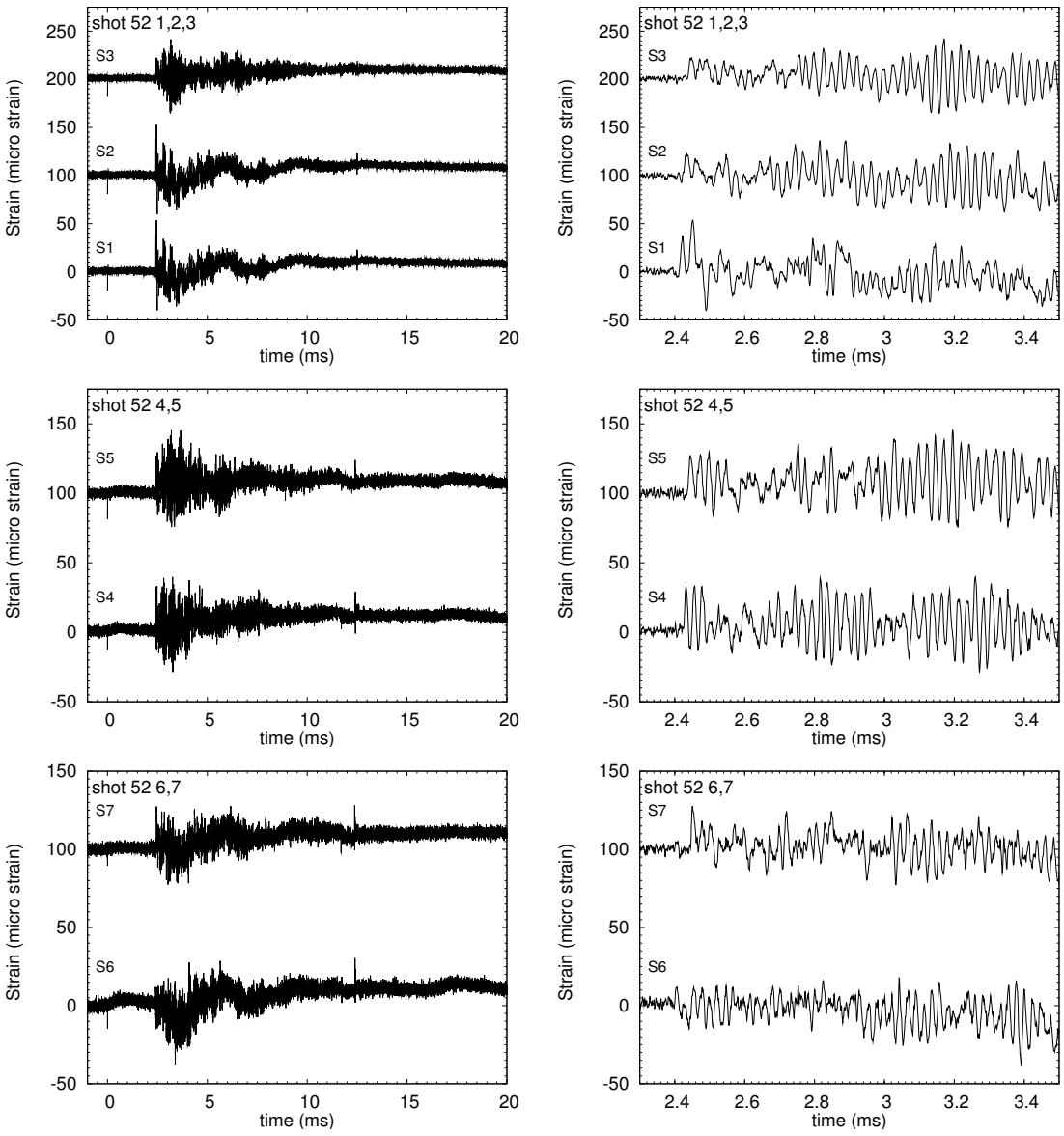

Figure 117: Strain traces, shot 52, tee specimen, $P_0 = 0.05$ bar

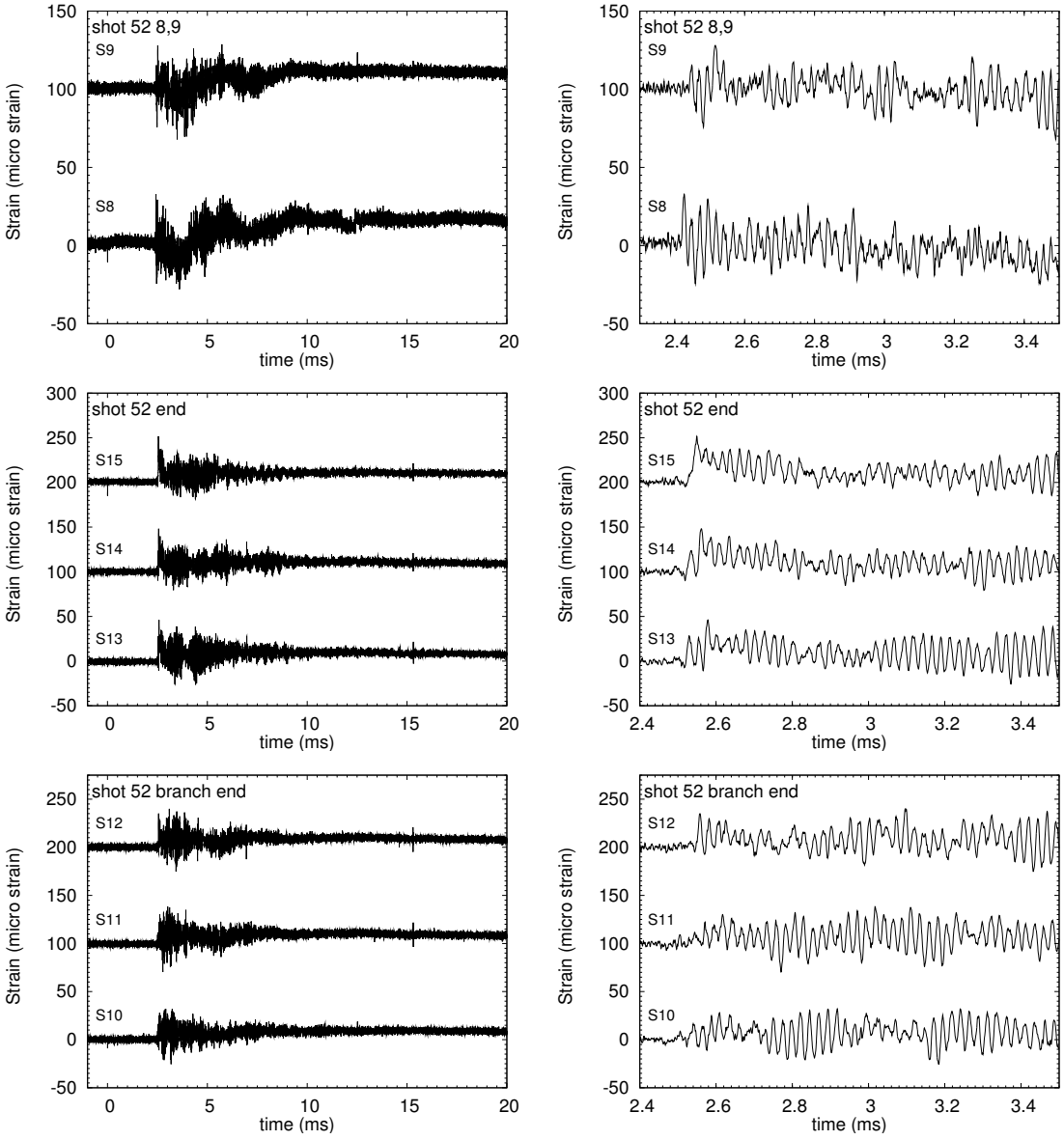

Figure 118: Strain traces, shot 52, tee specimen, $P_0 = 0.05$ bar

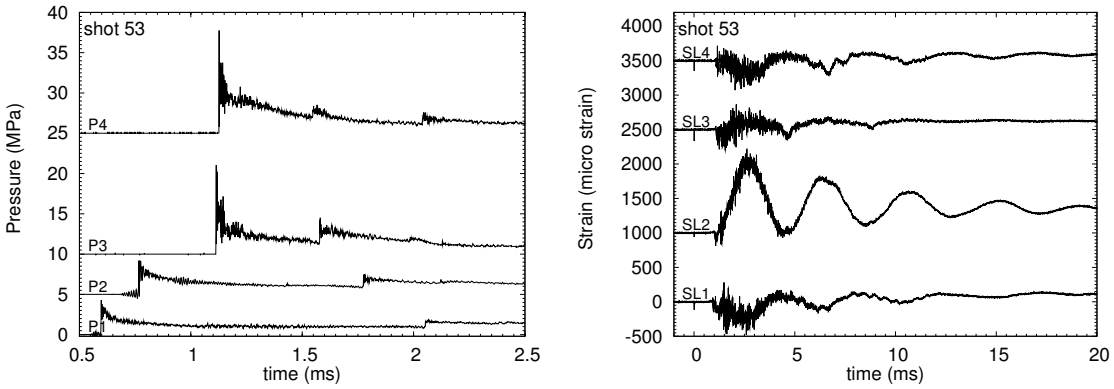

Figure 119: Pressure and strain traces, shot 53, tee specimen, $P_0 = 1$ bar

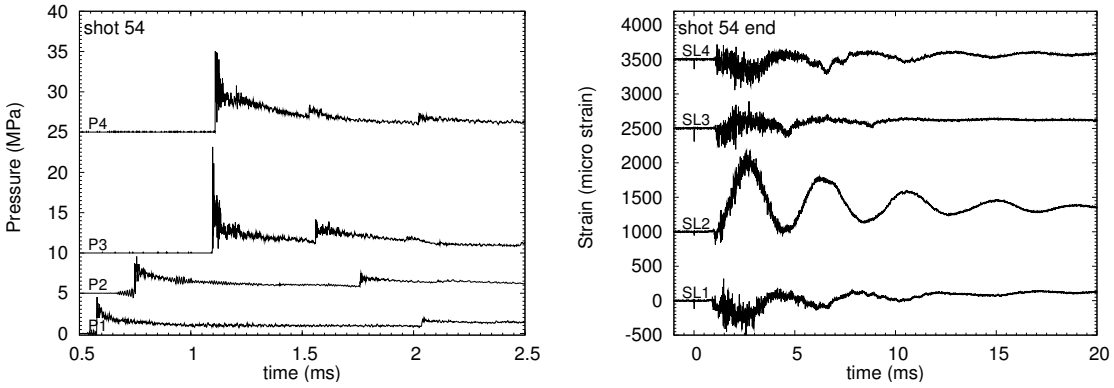

Figure 120: Pressure and strain traces, shot 54, tee specimen, $P_0 = 1$ bar

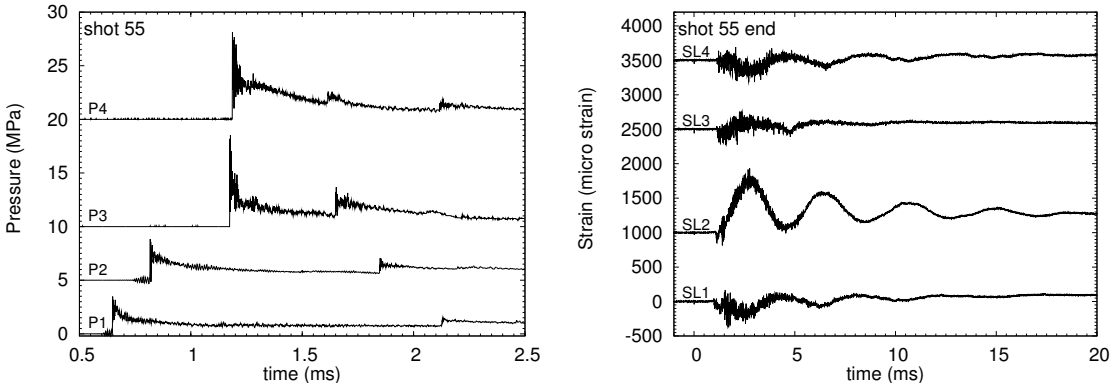

Figure 121: Pressure and strain traces, shot 53, tee specimen, $P_0 = 0.8$ bar

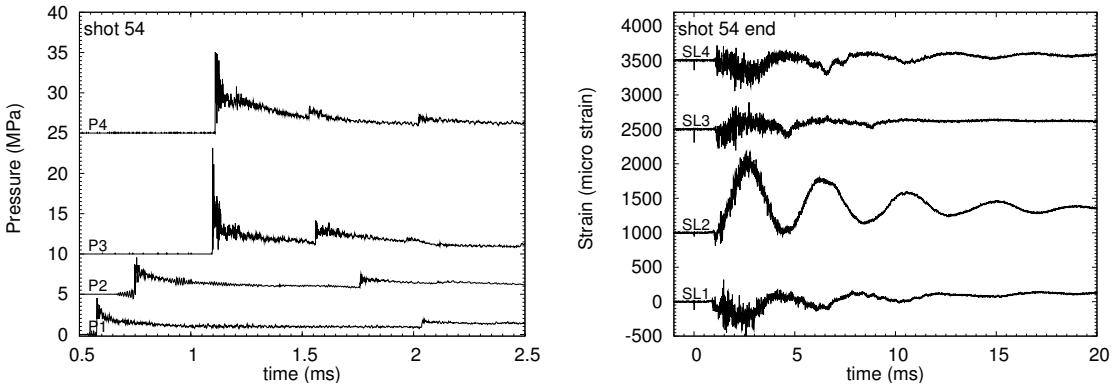

Figure 122: Pressure and strain traces, shot 54, tee specimen, $P_0 = 0.5$ bar